

**ON GRAIN BOUNDARY TRANSPORT OF HYDROGEN  
AND MECHANISM OF HYDROGEN-INDUCED  
INTERGRANULAR FRACTURE**

by

**Jing Yao**

A Thesis  
Submitted to the Faculty of Graduate Studies  
in Partial Fulfillment of the Requirements  
for the Degree of

**DOCTOR OF PHILOSOPHY**

Department of Mechanical Engineering  
University of Manitoba  
Winnipeg, Manitoba, Canada

(c) April, 1990



National Library  
of Canada

Bibliothèque nationale  
du Canada

Canadian Theses Service    Service des thèses canadiennes

Ottawa, Canada  
K1A 0N4

The author has granted an irrevocable non-exclusive licence allowing the National Library of Canada to reproduce, loan, distribute or sell copies of his/her thesis by any means and in any form or format, making this thesis available to interested persons.

The author retains ownership of the copyright in his/her thesis. Neither the thesis nor substantial extracts from it may be printed or otherwise reproduced without his/her permission.

L'auteur a accordé une licence irrévocable et non exclusive permettant à la Bibliothèque nationale du Canada de reproduire, prêter, distribuer ou vendre des copies de sa thèse de quelque manière et sous quelque forme que ce soit pour mettre des exemplaires de cette thèse à la disposition des personnes intéressées.

L'auteur conserve la propriété du droit d'auteur qui protège sa thèse. Ni la thèse ni des extraits substantiels de celle-ci ne doivent être imprimés ou autrement reproduits sans son autorisation.

ISBN 0-315-63273-9

Canada

**ON GRAIN BOUNDARY TRANSPORT OF HYDROGEN AND  
MECHANISM OF HYDROGEN-INDUCED INTERGRANULAR FRACTURE**

**BY**

**JING YAO**

A thesis submitted to the Faculty of Graduate Studies of  
the University of Manitoba in partial fulfillment of the requirements  
of the degree of

**DOCTOR OF PHILOSOPHY**

© 1990

Permission has been granted to the LIBRARY OF THE UNIVER-  
SITY OF MANITOBA to lend or sell copies of this thesis, to  
the NATIONAL LIBRARY OF CANADA to microfilm this  
thesis and to lend or sell copies of the film, and UNIVERSITY  
MICROFILMS to publish an abstract of this thesis.

The author reserves other publication rights, and neither the  
thesis nor extensive extracts from it may be printed or other-  
wise reproduced without the author's written permission.

# Abstract

The mechanism of hydrogen induced intergranular cracking in Ni has been investigated in this study. Two fundamental aspects are addressed: 1) the role of grain boundaries in the mass transport of hydrogen in materials contacted with hydrogen atmosphere, and 2) the effect of grain boundary pre-segregated hydrogen on the fracture mode and its mechanism. To accomplish these goals, three major investigations have been undertaken which can be summarized as follows.

(1) A new grain boundary diffusion model is presented. The model can be utilized to calculate the contribution of grain boundary diffusion to total mass transport in metals where lattice diffusion occurs interstitially. The grain boundary segregation factor, small grain sizes and a large range of the ratio of grain boundary to lattice diffusivity can be accommodated. Analytical solutions have been obtained for electrochemical permeation tests and penetration tests. Calculations predict that under most circumstances an average grain size of  $10\mu\text{m}$  can be used to determine conclusively if the transport of hydrogen in metals is enhanced by grain boundary diffusion.

(2) A dynamic technique to obtain qualitative information regarding hydrogen transport along grain boundaries in metallic materials has been proposed by re-interpreting and modifying the silver decoration technique proposed by Schöber and Dieker. The results of decoration tests in polycrystalline nickel and palladium with

and without hydrogen charging show that there is not a one-to-one correspondence between escaped hydrogen atoms and deposited silver atoms during the decoration process as reported previously. It is the oxidation film formed during electropolishing that prevents silver deposition. Any damage to the film and any process which reduces its stability may result in spontaneous silver deposition in the absence of hydrogen.

(3) Electrochemical permeation tests, silver decoration tests and penetration tests were performed in polycrystalline nickel with different grain sizes. Comparison of experimental results with theoretical predictions of the new grain boundary diffusion model indicated that grain boundaries are not high diffusivity paths for hydrogen. The dominant role played by grain boundaries during mass transport of hydrogen is retardation due to the trapping effect. The grain boundary diffusivity of hydrogen is concentration dependent; when the hydrogen concentration is extremely low, the grain boundary diffusion of hydrogen is virtually stopped. It is postulated that the low energy sites within grain boundaries are responsible for such retardation.

Grain boundary pre-segregated hydrogen changed the fracture mode from transgranular to intergranular at 77K when grain size was  $50\mu\text{m}$  or coarser, but had little effect in specimens with a grain size of  $10\mu\text{m}$ . By a comparison of the behavior of intergranular cracking due to hydrogen and that due to sulfur, a new mechanism of hydrogen induced intergranular cracking is proposed as follows.

Hydrogen enters the material and diffuses into the interior through the lattice. The hydrogen concentration in grain boundaries develops at almost the same rate as the lattice but is much higher because of the segregation factor. The segregated hydrogen at grain boundaries increases the driving force for intergranular cracking

by increasing the resistance to the leading dislocations in pileups in entering grain boundaries. If the local stress applied by dislocation pileups reaches the critical stress for grain boundary fracture before large scale cross slip takes place, intergranular cracking occurs.

# Acknowledgements

I would like to express my deepest gratitude to Dr. J. R. Cahoon for the supervision of this dissertation. He not only gave me his valuable suggestions and constant encouragement and support, but also granted me the freedom to complete the work in my own way. Without him, I could not have made this thesis possible.

I acknowledge gratefully the financial support provided by the Department of Mechanical Engineering and the Faculty of Graduate Studies, University of Manitoba, in the form of a Graduate Fellowship and an operating grant.

I also appreciate very much the technical assistance from Messrs. J. Van Dorp, D. Mardis and W. Hartle at the Metallurgical Sciences Laboratory, and R. Crampton at the Mechanical Engineering Department Machinshop.

Lastly, I would like to thank my family members for their sacrifice by staying with me in bitterly cold winters. I would also like to thank many friendly professors and fellow students who have helped and encouraged me throughout the course of this work.

# Nomenclature

$a$	half grain boundary width
$\beta$	constant
$C$	hydrogen concentration
$C_1$	hydrogen concentration through lattice
$C_2$	hydrogen concentration through grain boundaries
$C_{av}$	averaged hydrogen concentration
$C_g$	hydrogen concentration in grain boundaries
$C_g^s$	hydrogen concentration in grain boundary area on input surface
$C_g^*$	critical hydrogen concentration in grain boundaries for intergranular cracking to occur
$C_l$	hydrogen concentration in lattice
$C_0$	hydrogen concentration on input surface
$D_{eff}$	effective hydrogen diffusivity
$D_g$	hydrogen diffusivity along grain boundaries
$D_l$	hydrogen diffusivity in lattice
$E_b$	grain boundary binding energy with hydrogen
$f$	fugacity

$F$	Faraday constant
$h$	thickness of the membrane
$i$	permeation rate
$i_s$	steady state permeation rate
$i_s^*$	lattice diffusion steady state permeation rate
$i_{\text{total}}$	total permeation current
$K$	ratio of the grain boundary diffusivity to the lattice diffusivity
$L$	average grain size
$N$	number of dislocations in a pileup
$Q$	total diffusing substance which has passed through the membrane in time $t$
$R$	ratio of actual breakthrough time to that without grain boundary enhancement
$s$	segregation factor
$\sigma_a$	applied external stress
$\sigma_p$	stress applied by a pileup onto its barrier
$\sigma_g^r$	resistance to the controlling process for leading dislocations in a pileup to cross a boundary
$\sigma_g^*$	grain boundary strength
$T$	temperature
$t$	time
$t_a$	actual breakthrough time in polycrystal

- $t_b$  actual breakthrough time in monocrystal
- $t_{ag}$  actual breakthrough time in polycrystal with enhanced transport by grain boundaries
- $t_{lag}$  lag-time obtainable from a permeation curve

# Contents

<b>Abstract</b>	<b>i</b>
<b>Acknowledgement</b>	<b>iv</b>
<b>Nomenclature</b>	<b>v</b>
<b>1 Introduction</b>	<b>1</b>
<b>2 Literature Review</b>	<b>7</b>
2.1 Phenomenon of Hydrogen Induced Intergranular Cracking . . . . .	7
2.1.1 Observations in Metals and Alloys . . . . .	7
2.1.2 Impurity Effects . . . . .	8
2.2 Grain Boundary Diffusion . . . . .	10
2.2.1 Grain Boundary Structure . . . . .	10
2.2.2 Fast Grain Boundary Diffusion . . . . .	13
2.2.3 Models of Grain Boundary Diffusion . . . . .	15
2.2.4 Conflicts Regarding Grain Boundary Diffusion of Hydrogen . .	21
2.3 Mechanisms of Hydrogen Embrittlement . . . . .	22
2.3.1 General Mechanisms . . . . .	22
2.3.2 Mechanisms for Intergranular Cracking . . . . .	27

<b>3</b>	<b>Theoretical Modeling of Grain Boundary Diffusion</b>	<b>30</b>
3.1	Geometric Grain Boundary Model . . . . .	30
3.2	Case 1: Permeation Test . . . . .	34
3.2.1	Calculating the Permeation Current . . . . .	36
3.2.2	Calculating the Lag Time . . . . .	37
3.3	Case 2: Penetration Test . . . . .	38
<b>4</b>	<b>Theoretical Results and Discussion</b>	<b>40</b>
4.1	Permeation Curves . . . . .	40
4.1.1	Comparison with Literature Data . . . . .	40
4.1.2	Effect of $K$ Ratio . . . . .	42
4.1.3	Effect of Segregation Factor $s$ . . . . .	44
4.1.4	Effect of Grain Boundary Width . . . . .	47
4.1.5	The Break-through Time . . . . .	47
4.1.6	Time Lag Method for Measuring the Diffusion Coefficient . . . . .	49
4.1.7	Maximum Grain Size to Reveal Grain Boundary Transport . . . . .	53
4.1.8	Early Stages of the Transient . . . . .	55
4.2	Penetration Curves . . . . .	57
<b>5</b>	<b>Modification of the Silver Decoration Technique</b>	<b>60</b>
5.1	Introduction . . . . .	60
5.2	Experimental . . . . .	61
5.3	Results and Discussion . . . . .	63
5.3.1	In the Absence of Hydrogen . . . . .	63
5.3.2	In the Presence of Hydrogen . . . . .	69
5.4	Conclusions . . . . .	78

<b>6</b>	<b>Experimental Procedures</b>	<b>80</b>
6.1	Materials . . . . .	80
6.2	Specimen Preparation . . . . .	80
6.2.1	Specimens for Permeation and Decoration Tests . . . . .	80
6.2.2	Specimens for Penetration Tests . . . . .	81
6.3	Apparatus and Procedures for Electrochemical Permeation Tests . . .	82
6.4	Apparatus and Procedures for Silver Decoration Tests . . . . .	84
6.5	Apparatus and Procedures for Penetration Tests . . . . .	85
<b>7</b>	<b>Experimental Results</b>	<b>88</b>
7.1	Electrochemical Permeation Tests . . . . .	88
7.1.1	General Permeation Results . . . . .	88
7.1.2	Effective Diffusivity . . . . .	90
7.1.3	Trapping Effect . . . . .	91
7.1.4	Early Stage Plateaus . . . . .	91
7.1.5	The Steady State Permeation Rate . . . . .	94
7.2	Silver Decoration Tests . . . . .	95
7.2.1	Decoration Before Main Breakthrough . . . . .	95
7.2.2	Decoration Behavior of Grain Boundaries . . . . .	95
7.2.3	Effect of Segregated Sulfur . . . . .	99
7.3	Sulfur Induced Grain Boundary Cracking . . . . .	99
7.3.1	In the Absence of Hydrogen . . . . .	99
7.3.2	Combined with Hydrogen Effect . . . . .	107
7.4	Hydrogen Effect on the Fracture Mode . . . . .	107
7.4.1	Medium and Coarse Grained Specimens . . . . .	107
7.4.2	Fine Grained Specimens . . . . .	118

<b>8</b>	<b>Discussions</b>	<b>127</b>
8.1	Grain Boundary Transport of Hydrogen . . . . .	127
8.1.1	Dominant Process During Mass Transport of Hydrogen . . . . .	127
8.1.2	Explanation of Low $D_g$ at Low Concentrations . . . . .	128
8.1.3	$D_g$ at High Concentrations . . . . .	129
8.1.4	Comparison with the Literature . . . . .	130
8.1.5	Distinguishing Fast Paths from Short Circuit Paths of Diffusion	133
8.1.6	Dislocation Pipe Diffusion of Hydrogen . . . . .	134
8.2	Grain Size Effect on the Fracture Mode . . . . .	135
8.3	The Mechanism of Hydrogen Induced Intergranular Cracking . . . . .	137
8.3.1	Decohesion Theory . . . . .	138
8.3.2	Increase of the Driving Force . . . . .	139
8.3.3	New Mechanism for Intergranular Cracking . . . . .	140
<b>9</b>	<b>Conclusions and Recommendations</b>	<b>146</b>
9.1	Conclusions . . . . .	146
9.2	Recommendations . . . . .	148
	<b>Bibliography</b>	<b>149</b>
	<b>APPENDIX</b>	<b>157</b>
<b>A</b>	<b>FORTTRAN Program for Permeation Curves</b>	<b>157</b>
<b>B</b>	<b>FORTTRAN Program for Penetration Tests</b>	<b>162</b>

# List of Figures

2.1	Diffusivity spectrum for fcc metals [24,63]. . . . .	14
2.2	Schematic representation of three types of kinetics. Vertical lines indicate grain boundaries, curved lines are isoconcentration contours. The diffusion source coincides with the top horizontal lines. . . . .	16
2.3	Isolated grain boundary diffusion model in the B-kinetics regime. . .	18
2.4	Geometric model of grain boundary diffusion for parallel grain boundaries. . . . .	20
2.5	Localized-slip mechanism of hydrogen induced cracking: (a) ductile rupture, (b) when hydrogen is present. . . . .	26
2.6	Latanision's model for hydrogen induced intergranular fracture in Ni, (a) clean grain boundary and (b) with impurity precipitates. . . . .	29
3.1	Grain boundary aggregate. All grain boundaries are assumed perpendicular to the free surface of the membrane, i.e., into the paper. Those parallel to the surface are neglected. . . . .	31
3.2	The equivalent grain boundary tube. $z$ direction is into the paper. . .	32
4.1	Comparison of the present theory with that of Whipple [77] for $K = 10^6$ and $S = 1$ . The circles are calculated from eqn.(3.10) for $K \times S = 10^6$ . The solid curves are Whipple's results. . . . .	41
4.2	Normalized permeation rate vs reduced time for various $K$ values. . .	43

4.3	Permeation rate vs time for different $K$ values. $i_g^*$ is the steady state current corresponding to the bulk diffusion. . . . .	45
4.4	Normalized permeation rate vs reduced time with different binding energy. . . . .	46
4.5	Early stage of permeation curves shown in Figure 4.2. . . . .	51
4.6	Normalized permeation rate vs reduced time for various grain sizes. . . . .	54
4.7	Normalized permeation rates from grain boundary areas and the grain interiors for $K = 100$ where grain boundary transport becomes dominant. --: Percentage of grain boundary contribution. . . . .	56
4.8	Calculated penetration curves. Grain size $50\mu\text{m}$ . Curve 1 represents the lattice diffusion. The contribution from the grain boundaries is 50% for curve 2 and >99% for curve 3. . . . .	58
4.9	Calculated penetration curves. Grain size $10\mu\text{m}$ . Curve 1 represents the lattice diffusion. The contribution from the grain boundaries is 60% for curve 2 and >90% for curve 3. . . . .	59
5.1	Deposits on Ni270 (electropolished and uncharged) decorated in solution A for 12 hours. . . . .	64
5.2	Silver particles on an electropolished and uncharged Ni270 specimen decorated in solution C for 5 hours. . . . .	66
5.3	Deposits on uncharged Pd surface after decoration in solution A for 8 hours. . . . .	68
5.4	Decoration deposits on Ni270 surface after hydrogen charging and re-electropolishing in solution B for 9 hours. . . . .	71
5.5	Silver particles in charged area on Ni270 decorated in solution B for 30 min. Grain boundaries are decorated. . . . .	72

5.6	Silver particles in charged area on Ni270 degassed for 26 hours before re-electropolishing and decorated in solution B. Grain boundaries are not decorated. . . . .	74
6.1	Apparatus for permeation tests. . . . .	83
6.2	(a). Silver decoration cell: 1. Pt electrode, 2. front rubber seal; 3. test membrane; 4. downstream rubber seal and (b). membrane with various areas described in the text. . . . .	87
7.1	Measured permeation curves normalized by steady state value of permeation current of each individual test: 3) $h = 0.01\text{cm}$ , 4) $h = 0.007\text{cm}$ 5) $h = 0.01\text{cm}$ with coarse grains and 6) recharging of specimen from curve 3. . . . .	89
7.2	Early stages of permeation transients shown in Fig.7.1. . . . .	93
7.3	Non-decorated grain boundaries on area C of the downstream surface of Ni membrane. SEM 2000x. . . . .	97
7.4	Silver particle decorated grain boundaries on area A of the charging surface of Ni membrane. SEM 2000x. . . . .	98
7.5	Silver particle in the vicinity of a grain boundary on downstream surface of Ni membrane with segregated sulfur. SEM 1000x. . . . .	100
7.6	The ultimate strength and elastic limit vs temperature for grain size $50 \mu\text{m}$ . Curves $a_1$ , $a_2$ and $a_3$ represent grain boundary strengths affected by segregated sulfur. Curve e is the elastic limit. . . . .	101
7.7	SEM fractograph of a fracture surface in a specimen with segregated sulfur at grain boundaries which was fractured at 77K with large elongation. . . . .	103

7.8	SEM fractograph of microvoids on fracture surfaces of a specimen which was fractured intergranularly at 77K with segregated sulfur at grain boundaries. . . . .	104
7.9	Chemical analysis on a fracture surface by EDS. . . . .	105
7.10	SEM fractograph of matching fracture surfaces on a specimen which was fractured intergranularly at 77K with segregated sulfur at grain boundaries. . . . .	106
7.11	SEM fractograph of a coarse grained specimen fractured at 77K with segregated sulfur and pre-charged hydrogen. . . . .	108
7.12	SEM fractograph of a coarse grained rod specimen fractured at 77K with pre-charged hydrogen, close to charging surface. . . . .	109
7.13	SEM fractograph of a coarse grained rod specimen fractured at 77K with pre-charged hydrogen, close to the center. . . . .	110
7.14	SEM fractograph of a coarse grained rod specimen fractured at 77K with pre-charged hydrogen, transition band. . . . .	111
7.15	SEM fractograph of a coarse grained specimen fractured at 77K with pre-charged hydrogen. . . . .	112
7.16	Matching striations on fracture surfaces of a specimen fractured at 77K with pre-charged hydrogen. . . . .	113
7.17	SEM fractograph of a specimen fractured at 77K with pre-charged hydrogen. Average grain size was 50 $\mu$ m. . . . .	115
7.18	SEM fractograph of a medium grained specimen fractured at 77K with pre-charged hydrogen. The intergranular fracture depth is clearly seen. . . . .	116

7.19 Measured IG cracking depths (normalized by half thickness of the membrane) vs pre-charging periods in unaged specimens with a grain size of $50\mu\text{m}$ . All curves are calculated from eqn.(3.37). Curve 1 represents the lattice diffusion. The contribution from the grain boundary is 50% for curve 2 and >90% for curve 3. Thickness $h$ is $190\mu\text{m}$ (after polishing). . . . .	117
7.20 Stress strain curves in specimens saturated with hydrogen. Grain size $50\mu\text{m}$ . . . . .	119
7.21 The ultimate strength and elastic limit vs temperature for grain size $10\mu\text{m}$ . Curves a represents grain boundary strengths. Curve d is obtained from hydrogen pre-saturated specimens with a grain size of $50\mu\text{m}$ . Curve e is the elastic limit. . . . .	120
7.22 Stress strain curves in specimens saturated with hydrogen. Grain size $10\mu\text{m}$ . . . . .	122
7.23 SEM micrograph of a fine grained specimen which was pre-saturated with hydrogen but fractured with full ductility. The reduction of area was almost 100%. . . . .	123
7.24 Comparison of transgranular fracture surfaces: (a) fine grained specimen pre-saturated with hydrogen and fractured transgranularly; (b) well developed dimples in central area of a rod specimen shown in Fig.7.13. . . . .	124
7.25 SEM micrograph of side surface of a fine grained specimen which was pre-saturated with hydrogen but fractured with full ductility. The external stress is horizontal. . . . .	125

8.1	Re-produced Mütschele and Kirchheim's [128] measurement of hydrogen diffusion coefficient in single and polycrystalline palladium. The ratio of the latter to the former has a maximum value of 3.5 at high concentrations and a minimum of 0.05 extrapolated to low concentrations. . . . .	131
8.2	New mechanism for intergranular fracture due to hydrogen. . . . .	143
8.3	SEM micrograph showing an area around a grain boundary triple point on a specimen side surface which was fractured at room temperature in the absence of hydrogen but with segregated sulfur at grain boundaries. . . . .	144

# List of Tables

2.1	Fugacity -Pressure relationship for gaseous hydrogen at 298K (atm) .	23
4.1	Calculated $R$ ratios of actual breakthrough time to that without enhanced grain boundary transport. Detecting sensitivity is 0.1%. Binding energy is 11.6 kJ/mol. . . . .	50
4.2	Calculated $R$ ratios of actual breakthrough time to that without enhanced grain boundary transport. Detecting sensitivity is 0.1%. Binding energy is 20 kJ/mol. . . . .	50
4.3	Calculated $\beta$ values for various $K$ ratios and grain sizes. Binding energy is 11.6 kJ/mol ( $s = 114$ ). . . . .	50
4.4	Calculated $\beta$ values for $K=0$ with different grain size and binding energy. . . . .	51
4.5	Calculated permeation rates at lag-time. Binding energy is 11.6 kJ/mol.	54
5.1	Results of decoration tests without hydrogen charging . . . . .	65
5.2	Procedures of decoration tests in Ni charged with hydrogen . . . . .	70

# Chapter 1

## Introduction

Degradation of mechanical properties of many metals and alloys by hydrogen is a severe engineering problem upon which much work has been expended [1-9]. The fracture mode of hydrogen embrittled materials can be either transgranular or intergranular. It is well established that hydrogen induces or promotes intergranular cracking in many metals and alloys. For instance, the fracture mode of polycrystalline nickel is transgranular ductile rupture if no severe segregation of other impurities such as sulfur occurs. However, when solute hydrogen is introduced into the metal, the fracture mode changes to intergranular cracking [10-13].

Since the hydrogen decohesion theory was put forward in the early days of hydrogen embrittlement research, and also since it had been well documented that grain boundaries are fast diffusion paths in metals and alloys, the mechanism of hydrogen induced intergranular cracking seemed to be quite straight forward. Therefore, although quite a few mechanisms have been proposed to explain hydrogen embrittlement, the phenomenon of hydrogen induced intergranular cracking had been overlooked prior to the 1980's. However, as it becomes more evident that under certain circumstances, hydrogen does promote plasticity, more interest has been generated in this area during the past decade. The main objective of this study,

therefore, is to further our understanding of this particular phenomenon, i.e., to study the mechanism of hydrogen induced intergranular cracking.

Obviously, for intergranular cracking to occur, hydrogen has to arrive at interior grain boundaries by diffusion through the lattice, grain boundaries, dislocation networks or by moving dislocation transport as dislocation core atmospheres. A better understanding of hydrogen induced cracking requires a knowledge of the contribution of each of these processes to hydrogen transport. Considerable effort has been expended in the past decade towards this end.

Many researchers in this field consider grain boundaries as fast diffusion paths for hydrogen; i.e., the ratio of grain boundary diffusivity to lattice diffusivity is high,  $K = D_g/D_l \gg 1$ . Quite a few attempts have been made to provide direct experimental evidence for enhanced transport of hydrogen by grain boundaries. In 1982, Tsuru and Latanision[14] used the electrochemical permeation technique to investigate grain boundary diffusion of hydrogen in polycrystalline nickel and observed an almost instant increase in the anodic current which saturated in a few minutes well before the main transient started. They considered this early saturation as the first experimental evidence of rapid grain boundary diffusion. By simply comparing two saturations, they calculated a  $K$  ratio of 60. One year later, Schöber and Dieker [15] reported other experimental evidence using the silver decoration technique originally designed by themselves.

These results concerning the enhanced grain boundary transport of hydrogen were initially accepted. However, when Tsuru and Latanision's work was duplicated, the observation of an early breakthrough was found to be a result of experimental procedures and could be eliminated. Consequently, to clarify the situation regarding grain boundary transport of hydrogen has become a major objective of

this study, since all newly proposed mechanisms of hydrogen induced intergranular cracking suggest enhanced transport of hydrogen by grain boundaries. In order to do this, it would be ideal to have a technique which is capable of both dynamically and directly monitoring the emerging consequences of hydrogen permeation flux in terms of microstructural characteristics. The electrochemical permeation test is a dynamic technique, i.e. it provides time related information [16,17]. However, this information is averaged over the downstream surface of the membrane. The silver decoration technique is supposed to have the required capability [15,18]; however, it was found in the beginning of this research that the surface effects could obscure the results and reproducibility was so poor that the technique had to be modified before it could be used with any confidence. Since this technique is important to this study, a separate chapter is assigned for its re-interpretation and modification.

In the meantime, however, Lee et al [19] proposed a new thermal analysis technique, and provided an indication that also supported enhanced grain boundary transport of hydrogen in nickel. In 1988, Kimura and Birnbaum [20] performed hydrogen penetration tests in pure polycrystalline nickel. By measuring the intergranular depths in specimens which were precharged with hydrogen at different temperatures for various periods but fractured at 77K, they concluded that hydrogen transport was enhanced by grain boundaries. However, Birnbaum [21] admitted that an essential mistake was made in their derivations. A high  $K$  value,  $10^3 \sim 10^4$ , would be obtained if the mistake was corrected. Further, it turned out by analyzing their data with Whipple's model that the activation energy for diffusion along grain boundaries was higher than that through the lattice even when different concentrations for the lattice and grain boundary area on the charging surface were taken into account. Obviously, this is incorrect.

Further, during the most recent hydrogen conference, *The Fourth International Conference on the Effects of Hydrogen on Material Behavior*, September 12-16, 1989, Wyoming, USA, two groups reported experimental results both of which supported the fast diffusion concept [22,23]. One report followed Tsuru and Latanision's lead by detecting the early breakthrough current, and failed to notice any significant changes in the steady state current. The other report found just the opposite result; i.e., only the changes in the steady state current were related to grain boundary transport. It is interesting to note that the co-author of the latter report was Latanision himself, which was in conflict with their previous theories [14].

It is not known what difference should be expected in the shapes of permeation curves for mono- and poly-crystalline membranes. Should the steady state current increase in polycrystalline membranes? Should there be an early breakthrough and, if so, should there be a plateau? The problem is that there have been no theoretical calculations available which can predict the conditions under which the enhanced transport of hydrogen by grain boundaries can be experimentally revealed if it does occur. In other words, it is not known how to design a conclusive experiment.

It is well established that for the case of self and substitutional lattice diffusion the grain boundary diffusivity is indeed much greater than the lattice diffusivity. Several mathematical models have been successfully used to analyze test results. In most cases, grain boundary diffusivities are orders of magnitude higher than lattice diffusivities. This has been believed to be due to substantially smaller activation energies of diffusion in grain boundaries [25]. Since hydrogen is a small interstitial element, its diffusion in the lattice is via an interstitial mechanism, and its lattice diffusivity is high in most metals even at room temperature. It is reasonable that the limited extra volume available in grain boundaries would not greatly increase the

mass transport of hydrogen. Therefore, the lattice and grain boundary diffusivities of hydrogen are most likely to be in the same order.

It is noted that mathematical models have been used in the analyses of those reports supporting enhanced hydrogen transport by grain boundaries [25]. These models are only applicable to cases where grain boundary diffusion is dominant; i.e. where the diffusing atom is a substitutional alloying element and diffuses via a vacancy mechanism in the bulk lattice. This results in a different coefficient several orders of magnitude less than that for grain boundary diffusion.

Gilmer et al [26] have obtained an analytical solution of grain boundary diffusion for a set of parallel straight grain boundaries in a thin film. Apparently, this geometric model is far from the reality. However, when  $K$  is very large, grain boundary diffusion dominates and lattice diffusion does not contribute significantly. Therefore, overlapping from adjacent grain boundaries can be ignored and grain boundaries can be approximated as straight parallel lines. Abraham et al [27] have proposed theoretical predictions of permeation rates using Levine and MacCallum's [28] model. Again, their model is applicable only to the cases where grain boundary transport dominates and they themselves acknowledged that the model is inappropriate where  $K < 10^5$ .

The existing models for mass transport cannot accommodate the case where the grain boundary diffusivity is of the order of the lattice diffusivity. Therefore, they are incapable of determining the maximum grain size at which grain boundary diffusion contributes significantly to mass transport through the metal. In addition, the activity of grain boundaries may well be different than that of the lattice and this could lead to a segregation effect where the equilibrium concentration of impurities in the grain boundaries is significantly different than that in the lattice. Therefore,

in order to clarify the role of grain boundaries in mass transport through metals, a model is needed which a) accommodates any value of  $K$  from zero to infinity; b) is appropriate for both large and small grain sizes; and c) includes the segregation effect.

This dissertation has developed a new model which has all these features. Following Gilmer and Farrell's [26] procedure, analytical solutions are obtained for the permeation tests and penetration tests. Since most work in this area was done in nickel, data available in the literature for the nickel-hydrogen system have been used to make the results explicit. With the guidance of the theoretical predictions, electrochemical permeation tests, silver decoration tests, and penetration tests were performed.

It is noted that degradation of materials due to impurity segregation has also been the subject of extensive study [29]. The mechanism of impurity segregation induced intergranular cracking is much better understood than for the case of hydrogen. Several approaches are available in the literature and the agreement between theories and experimental results is fair. Experimental evidence has shown that the effects of impurities and hydrogen are somewhat similar. Therefore, it would be informative to compare the intergranular cracking behavior due to hydrogen with that due to sulfur. In this way, a new mechanism of hydrogen induced intergranular cracking has been derived and is presented in this dissertation.

# Chapter 2

## Literature Review

Generally speaking, hydrogen embrittlement refers to the degradation of mechanical properties of metals and alloys due to internal or external hydrogen. Studies of this problem extend well back into the last century. There have been many reviews and conference proceedings published on hydrogen in metals since 1970's [1-9]. However, a satisfactory understanding of hydrogen embrittlement has not yet been achieved. Our present knowledge remains at a phenomenological level. In the following, a review is given to the topics that are most related to the objectives of this study.

### **2.1 Phenomenon of Hydrogen Induced Intergranular Cracking**

#### **2.1.1 Observations in Metals and Alloys**

Hydrogen can be introduced into engineering materials during processing and service applications. It has been well established that hydrogen induces or promotes intergranular cracking in many metallic materials. When specimens of various iron-base alloys are tested mechanically either after cathodic or thermal charging of hydrogen, or directly in the aqueous or gaseous hydrogen environment, fracture

occurs at reduced stress intensity levels along prior austenite grain boundaries [30-41]. In high purity iron, hydrogen also changes the fracture mode from transgranular to intergranular at 170 K [42].

It has been shown that austenitic stainless steels are also susceptible to hydrogen embrittlement. In Type 304 austenitic stainless steel sensitized by aging at intermediate temperatures (e.g., 900 K), hydrogen induced cracking occurs along the grain boundaries [43,44]. However, conflicts exist regarding fracture paths in non-sensitized stainless steels. While many researchers report transgranular cracking, intergranular cracks were obtained in solution annealed smooth bar specimens which were stressed while being charged [43]. Intergranular cracking was also obtained in a stable austenitic stainless steel (Cr21-Ni6-Mn9) when tested in a high pressure hydrogen atmosphere, 173 Mpa [45].

Hydrogen induced intergranular cracking in a ferritic stainless steel (12Cr-Mo) has been observed when tensile specimens with a quenched-and-tempered microstructure were tested after cathodic charging with up to 6 wppm hydrogen [46,47]. In a high strength 7075 T651 aluminum alloy, Gest and Troiano [48] observed cracking along grain boundaries where the specimens had undergone hydrogen charging.

Nickel and Ni base alloys are typical in this group. With clean grain boundaries, fracture occurs in a ductile manner, and the cross-section reduces to a needle point. When hydrogen is introduced, the fracture mode changes to intergranular brittle failure at room or subzero temperatures [10-13].

### **2.1.2 Impurity Effects**

Segregation of impurities to grain boundaries can either increase or decrease the tendency of hydrogen induced intergranular fracture. Kimura and Kimura [45] performed tensile tests during hydrogen charging. A specially prepared, high purity

iron fractured along grain boundaries after a few percent elongation. The specimen, however, was ductile if it was doped with carbon to about 20 wppm. They concluded that carbon segregation at grain boundaries prevents grain boundary fracture. Their work was consistent with that of Shin et al. [49] who found carburization of pure iron to 185 appm prevented intergranular cracking. A similar effect was reported by Funkenbusch et al. [50] for phosphorus in Monel 400 alloys. They suggested that P improves atomic packing along grain boundaries which in turn reduces the concentration of embrittler.

The influence of sulfur, phosphorus and antimony segregation on intergranular hydrogen embrittlement in nickel was studied by Bruemmer et al. [51]. They found that sulfur was the critical grain boundary segregant due to its large enrichment at grain boundaries,  $10^4 \sim 10^5$  times the bulk content. There was a direct relationship between sulfur coverage and hydrogen -induced intergranular failure. Phosphorus was shown to be significantly less effective than sulfur or antimony in inducing the intergranular hydrogen embrittlement of Ni. Since phosphorus segregated strongly at grain boundaries and limited sulfur enrichment, the addition of phosphorus to Ni even improved ductility and reduced the tendency for intergranular cracking.

An interesting effect of oxygen was revealed by Ogino and Yamasaki [52] who investigated the influence of vacuum annealing on intergranular hydrogen embrittlement of Ni. They observed a high susceptibility to intergranular hydrogen embrittlement due to vacuum annealing compared to that annealed in dry hydrogen. The deleterious effect of vacuum annealing was presumed to be due to the penetration of oxygen along grain boundaries during annealing.

In conclusion, although impurities have various intrinsic effects on grain boundary strengths, they have to compete for the grain boundary sites among themselves.

Therefore, the overall effect on grain boundary embrittlement due to hydrogen must be determined case by case.

## 2.2 Grain Boundary Diffusion

### 2.2.1 Grain Boundary Structure

#### 2.2.1.1 Grain Boundary Crystallography

A grain boundary is the region where two ordered structures (i.e. the two adjoining crystal lattices) meet, and therefore, it should also possess an ordered structure. First, suppose two lattices (made up of different color) extend throughout all of the space and coincide at an origin, and then let lattice 2 rotate around the origin for certain angle. The two infinite, rigid, interpenetrating lattices form the so-called dichromatic pattern [53]. The points of these two lattices coincide on a superlattice which is called the coincidence site lattice, CSL [54]. By discarding appropriate atoms from both sides of the desired grain boundary plane, and allowing the entire bicrystal system to relax, a boundary is thus produced. During the relaxation, atoms in the grain boundary core will adjust their positions. The final atomic structure of some particular grain boundaries (e.g. symmetric tilt boundaries) has been obtained from atomistic calculations using the method of molecular statics [55,56] which assumes the atoms interact via a pairwise central force potential in calculating the minimum energy configuration of the bicrystal ensemble.

The calculations have revealed that (1) the periodicity of the relaxed structure is identical to the periodicity of the plane in the CSL parallel to the boundary plane; (2) the core is relatively narrow, no more than a few atom distances in thickness; (3) since it is impossible to pack atoms into a boundary region at the same high density as in the perfect crystal, excess volume inevitably exists in the core with

some atoms in loose environments and others squeezed in one direction or another. However, the density of the core structure and the average number of near neighbors surrounding each atom are only slightly lower than in the perfect crystal.

#### **2.2.1.2 Intrinsic Grain Boundary Dislocations**

There is considerable evidence that boundaries of relative short wavelength periodicity, which are parallel to relatively dense planes of the CSL, are often of relatively low energy compared with more general boundaries with longer periodicities [57,58]. When the crystal misorientation deviates from the special misorientation producing the dense CSL the boundary can minimize its energy by preserving patches of the special low energy boundary and introducing an array of grain boundary dislocations, which accommodates the difference in misorientation between the special misorientation and the actual boundary misorientation. The result is a structure consisting of an array of intrinsic grain boundary dislocations (IGBDs) embedded in a boundary structure of relatively low energy. Therefore, IGBDs are part of the equilibrium structure of grain boundaries.

#### **2.2.1.3 Extrinsic Grain Boundary Dislocations**

Extrinsic grain boundary dislocations (EGBDs) are extra dislocations present in the boundary as a result of the history of the specimen. Unlike IGBDs, they do not act in a systematic way to accommodate the crystal misorientation.

EGBDs can be produced by the impingement and dissociation of lattice dislocations [59]. The Burgers vectors of perfect EGBDs are vectors of the so-called DSC lattice and in certain special cases, partial EGBDs may also exist [60]. The DSC lattice is formed by all possible translation vectors that preserve the dichro-

matic pattern mentioned above. For the simple cubic structure, DSC lattice is the reciprocal lattice of the CSL [61]. An important feature of many EGBDs is their association of a step in the boundary plane at the dislocation; such a step appears whenever the translational shift in the dichromatic pattern produced by introducing the dislocation has a non-zero component normal to the boundary plane [62].

#### 2.2.1.4 Point Defects in Grain Boundary

Molecular statics calculations of the structure of vacancies and interstitials in the cores of a variety of large-angle grain boundaries have been performed [63,64]. The relaxations around a point defect in a grain boundary depend upon the type of metal, the crystal misorientation, the grain boundary plane orientation, etc. In metals represented by "hard" interatomic potentials, e.g. tungsten, the vacancies tend to produce more widely spread displacements in the core, whereas for "soft" metals, e.g. copper, the displacements are more localized. The vacancy itself remains as a distinguishable point defect in the irregular core structure; its binding energy to the core varies from site to site in a grain boundary, generally being attractive.

An interstitial atom produces large outward atomic displacements in its vicinity, and its binding energies are generally considerably larger than that for the vacancies. The interstitial formation energies are approximately twice as large than that for vacancies.

There has been a considerable amount of experimental work that is generally consistent with the above calculated results. Direct observations of the intersection of boundaries with the free surfaces in the field ion microscope confirmed that the grain boundary core is quite narrow [65]. Direct lattice imaging in the electron microscope for a tilt boundary in gold confirmed the main features of the calculated

grain boundary core structure [66].

### 2.2.2 Fast Grain Boundary Diffusion

It has been clearly demonstrated that substitutional atoms diffuse orders of magnitude more rapidly along grain boundaries than the crystal lattice at temperatures appreciably below the melting point [67-69]. Fig.2.1 shows the diffusivity spectrum for fcc metals deduced by Gjostein [67]. Balluffi [24] has concluded in a most recent review that fast grain boundary diffusion occurs by a vacancy mechanism in the vast majority of boundaries including small- and large-angle boundaries. The atom jumping occurs by vacancy exchange between a variety of sites in the grain boundary core.

The enhanced transport is due to the fact that both the formation and motional components of the activation energy for diffusion are smaller in grain boundaries than in the lattice, which has been confirmed by experimental measurements. The ratio of two activation energies is found to be about 0.5 for the average high-angle grain boundaries in random polycrystalline specimens and about 0.7 for special boundaries including the cases of the epitaxial and textured films [70].

One observation worth noting is the anisotropy of diffusivity in tilt boundaries: the boundary diffusion rates in symmetric boundaries are usually faster along the tilt axis than perpendicular to it. In the case of silver self diffusion along [001] symmetric tilt boundaries, the ratio was observed to be high ( $> 10$ ) for small tilt angles [71]. This can be interpreted on the basis of the structural unit model of grain boundaries given above.

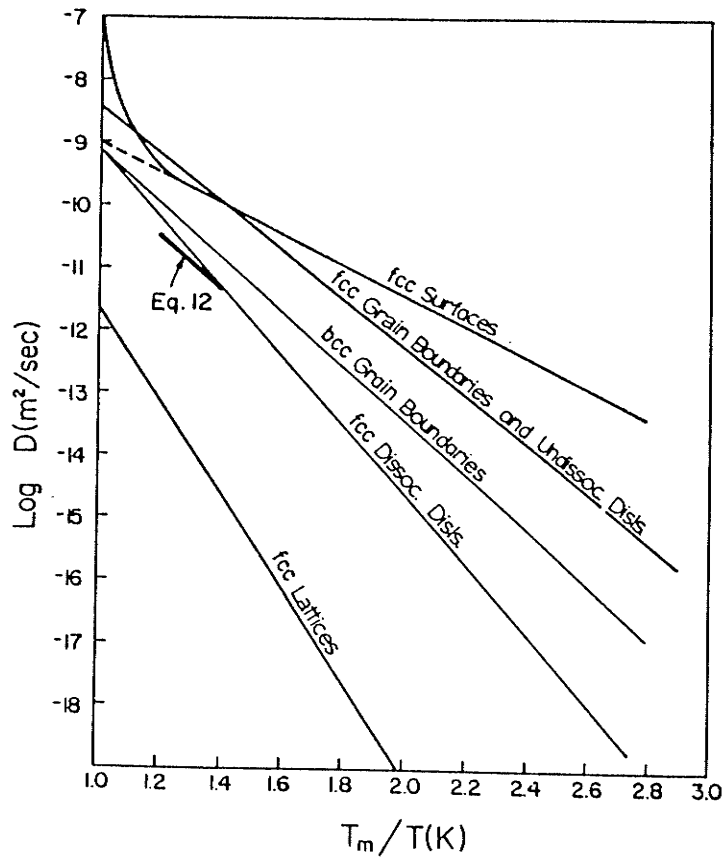


Figure 2.1: Diffusivity spectrum for fcc metals [24,63].

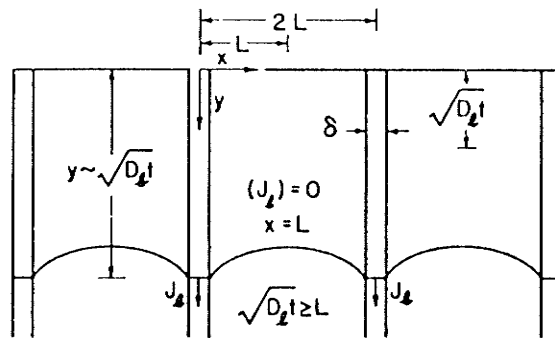
## 2.2.3 Models of Grain Boundary Diffusion

### 2.2.3.1 Grain Boundary Diffusion Kinetics

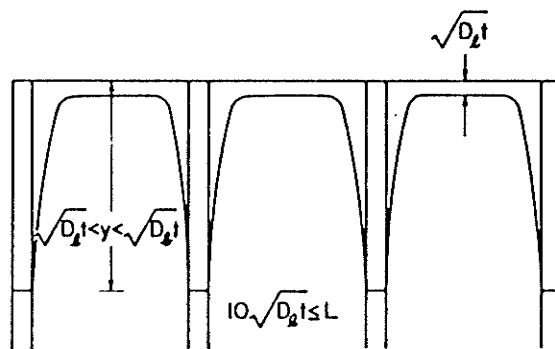
Preferential diffusion along fast diffusion paths may give rise to several limiting types of behavior, in some of which the kinetics of diffusion remain, on a macroscopic scale, in apparent agreement with Fick' law. These possible types of behavior have been classified by Harrison [72] into three types of kinetics. As grain boundary diffusion can seldom be decoupled from the lattice, the diffusing species is likely to leak into the adjoining lattice. The extent of this leakage determines the types of these kinetics, or in other words, the extent to which lattice diffusion influences the material transport along grain boundaries determines the kinetic regime which prevails.

The three types of kinetics are shown in Fig.2.2 [73]. Type B can be considered as the general case, and types A and C are two opposite limiting cases which give rise to simple overall kinetics. In a hypothetical model, a transition from type A through B to C may be thought to occur when the mobility of diffusant in the boundaries is increased by orders of magnitude from the bulk mobility value. In practice, in any system in which diffusion can be studied continuously from very short to very long times, the behavior will initially be type C, and will develop into type B and ultimately type A.

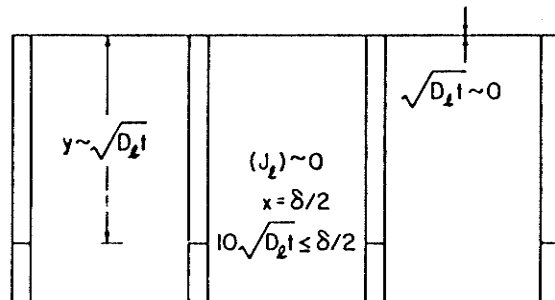
Originally, all analytical solutions regarding grain boundary diffusion were proposed for self diffusion processes. Therefore, impurity effects were not taken into account. Gibbs [74] was the first to incorporate the solute segregation factor  $s$  into the analysis to deal with diffusion of substitutional impurities. In most cases, this does not cause any severe problem in mathematical derivations. Therefore, in the following,  $s$  is added in the solutions without specific explanations.



(a) A-KINETICS



(b) B-KINETICS



(c) C-KINETICS

Figure 2.2: Schematic representation of three types of kinetics. Vertical lines indicate grain boundaries, curved lines are isoconcentration contours. The diffusion source coincides with the top horizontal lines.

### 2.2.3.2 An Isolated Grain Boundary

Grain boundary diffusion measurements in bulk materials invariably involve B-kinetics, where the analysis can be simplified to considering an isolated grain boundary as shown in Fig.2.3. This case has been dealt with and discussed by several researchers [75-78]. Whipple obtained an exact solution for the concentration in the lattice,  $C_l$ , for infinite source conditions where

$$C_l = C_1 + C_2. \quad (2.1)$$

Here,  $C_1$  is the lattice concentration which is due to the ordinary planar diffusion in the lattice, that is

$$C_1 = C_0 \operatorname{erfc}(\eta/2) \quad (2.2)$$

and  $C_2$  is the contribution out from grain boundaries :

$$C_2 = \frac{\eta C_0}{2\sqrt{\pi}} \int_1^K \frac{d\sigma}{\sigma^{3/2}} \exp(-\eta^2/4\sigma) \times \operatorname{erfc} \left[ \frac{1}{2} \sqrt{\frac{K-1}{K-\sigma}} \left( \varepsilon + \frac{\sigma-1}{\beta} \right) \right]. \quad (2.3)$$

The solution is written in terms of reduced variables which are defined as follows:

$$\begin{aligned} \eta &= \frac{y}{\sqrt{D_l t}} \\ \varepsilon &= \frac{x-a}{\sqrt{D_l t}} \\ K &= \frac{D_g}{D_l} \\ \beta &= \frac{(K-1)as}{\sqrt{D_l t}} \end{aligned} \quad (2.4)$$

Gilmer and Farrell [79] used Fourier-Laplace transforms to obtain following solutions for finite thickness system and constant source conditions:

$$C_1 = 1 - \frac{4}{\pi} \sum_{m=1}^{\infty} \frac{1}{2m-1} \sin(\mu_{2m-1}\eta) \exp(-\mu_{2m-1}^2) \quad (2.5)$$

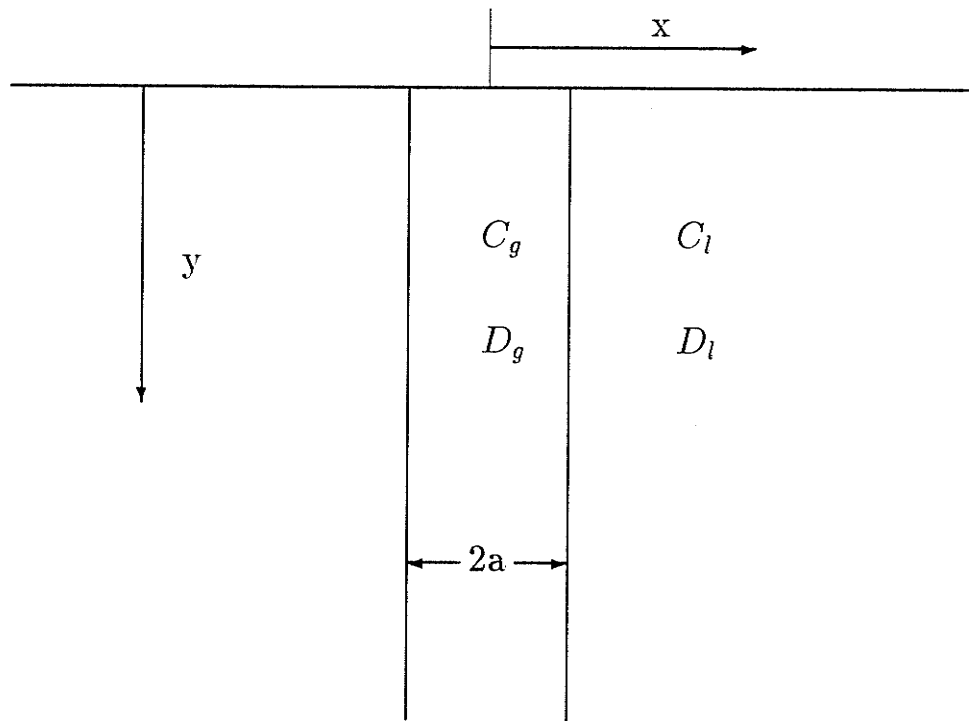


Figure 2.3: Isolated grain boundary diffusion model in the B-kinetics regime.

and

$$C_2 = \frac{2C_0}{\eta_0} \int_1^K d\sigma \sum_{m=1}^{\infty} \sin(\mu_{2m-1}\eta) \exp(-\mu_{2m-1}^2\sigma) \mu_{2m-1} \times \operatorname{erfc} \left[ \frac{1}{2} \sqrt{\frac{K-1}{K-\sigma}} \left( \varepsilon + \frac{\sigma-1}{\beta} \right) \right] \quad (2.6)$$

where

$$\begin{aligned} \eta_0 &= \frac{L}{\sqrt{D_1 t}} \\ \mu_{2m-1} &= \frac{(2m-1)\pi}{2\eta_0} \end{aligned} \quad (2.7)$$

### 2.2.3.3 Parallel Grain Boundaries

When overlapping of the diffusion fields of the adjoining grains cannot be ignored, solutions for isolated grains are not expected to account for the kinetic behavior. The analysis has to consider the periodic boundary arrangement. The simplest form is an array of parallel and equally spaced grain boundaries which has been solved by Gilmer and Farrell [26] for finite thickness system. Their model is shown in Fig.2.4. They construct a solution given by

$$C_l(x, y, t) = 1 - \sum_{n,m=1}^{\infty} A_{nm} X_{nm}(x) Y_n(y) T_{nm}(t) \quad (2.8)$$

where the terms are chosen for reasons of symmetry as

$$\begin{aligned} X_{nm} &= \cos(\alpha_{nm}x) \\ Y_n &= \sin(\beta_n y) \\ T_{nm} &= \exp[-D_1 t(\alpha_{nm}^2 + \beta_n^2)] \end{aligned} \quad (2.9)$$

Values of  $\beta_n$  are determined by the boundary condition at  $y = h$ . Values of  $\alpha_{nm}$  can be obtained from the following transcendental relationship obeyed at the coupling

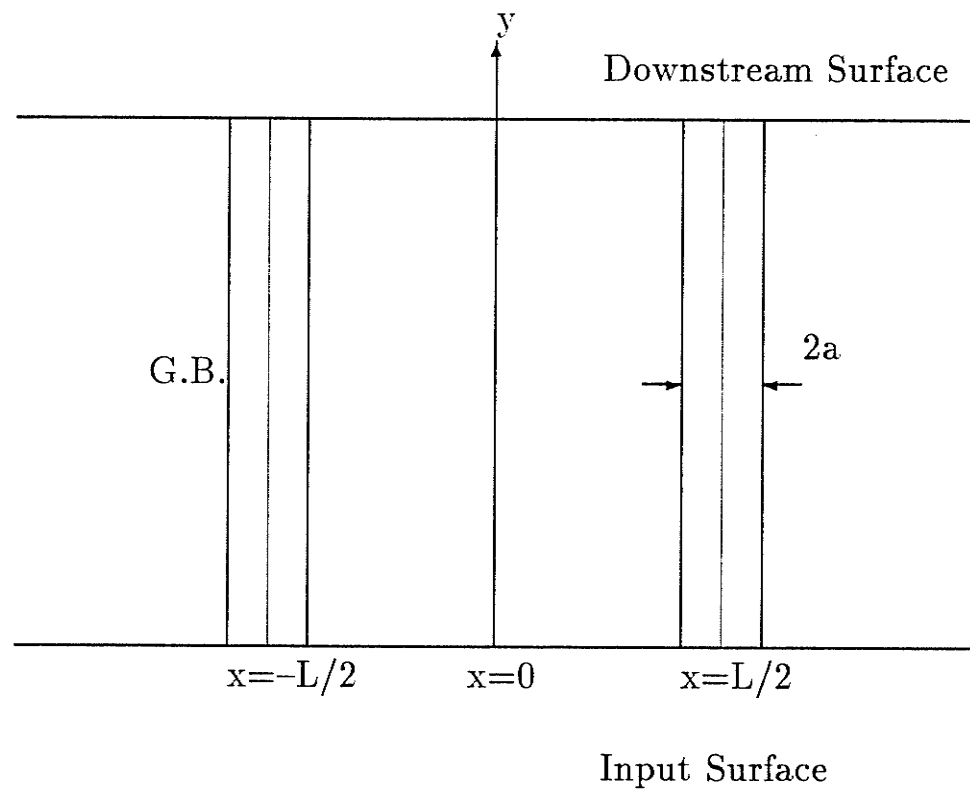


Figure 2.4: Geometric model of grain boundary diffusion for parallel grain boundaries.

interface  $x = L/2 - a$ :

$$(K - 1)\beta_n^2 - \alpha_{nm}^2 = (2\alpha_{nm}/a) \tan(\alpha_{nm}L). \quad (2.10)$$

The constants  $A_{nm}$  can be obtained from

$$A_{nm} = \frac{-4B[\sin(\alpha_{nm}L/2) + a\alpha_{nm} \cos(\alpha_{nm}L/2)]}{L\alpha_{nm}\{(1 + 4a/L)[\cos(\alpha_{nm}L/2)]^2 + [\sin(\alpha_{nm}L/2)]^2\}}. \quad (2.11)$$

where, again,  $B$  is determined by the boundary condition at  $y = h$ .

It is worth noting that only the simplest form of geometric periodicity of grain boundaries was used in this model, which is reasonable for the case of grain boundary diffusion in thin films. When grain size is in the same order or smaller than the thickness of the film, their geometric model is no longer suitable.

#### 2.2.4 Conflicts Regarding Grain Boundary Diffusion of Hydrogen

Many researchers in this field consider that grain boundaries are fast diffusion paths for hydrogen. Calder et al [80] obtained grain boundary diffusivities of tritium in 304- and 316-stainless steel through direct measurement of tritium concentration profiles. Fisher's [75] and Suzuoka's [76] models were used in their analysis. Comparing with the bulk diffusion coefficient obtained in the same materials [81] they reported a very high ratio of grain boundary diffusivity to lattice diffusivity,  $K = D_g/D_l \approx 10^8$ . However, this has never been proven by other experiments, not even by autoradiography tests performed by themselves.

Tsuru and Latanision [14] used the electrochemical permeation technique [16] to investigate grain boundary diffusion of hydrogen in nickel and observed an almost instant increase in the anodic current which saturated in a few minutes well before the main transient started. They attributed this first saturation to rapid grain

boundary diffusion and by simply comparing two saturations a  $K$  ratio of 60 was derived. Lee et al [19] used the thermal analysis technique to obtain an indication that also supports enhanced grain boundary transport of hydrogen in nickel.

Contrary to these observations, several attempts reported in the literature have failed to demonstrate any effect of grain size on the measured diffusion coefficients [82] or other related parameters [83,84]. Further, Siderenko and Sidorak [85] reported that the grain boundary diffusivity of hydrogen in nickel was smaller than that of the lattice diffusivity; i.e.  $K < 1$ . The activation energy for hydrogen diffusion along grain boundaries was higher than that in the lattice. However, they used an over-simplified equation to calculate  $D_g$ :

$$D_{\text{eff}} = D_l + \alpha D_g \quad (2.12)$$

where  $D_{\text{eff}}$  is the measured effective diffusivity and  $\alpha$  is the volume percentage of grain boundaries in the specimen. If segregation factor is taken into account, their conclusion might be different. Nevertheless, their results suggest that hydrogen diffusion is not enhanced by grain boundaries. Therefore, it is seen that grain boundary diffusion of hydrogen is one of the most controversial problems in hydrogen embrittlement research.

## **2.3 Mechanisms of Hydrogen Embrittlement**

### **2.3.1 General Mechanisms**

Hydrogen is a versatile embrittler. Hydrogen embrittlement can take place in many ways, some of which are understood quite well and appropriate mechanisms have been established. For instance, hydrogen attack at high temperatures has been attributed to reactions which produce methane [86,87]. Hydrogen embrittlement in certain materials such as Ti, Zr, Nb, etc. has been attributed to the formation of

Table 2.1: Fugacity -Pressure relationship for gaseous hydrogen at 298K (atm)

$f$	28.1	247	896	1860	3060	6880	12500	$1.1 \times 10^5$	$9.64 \times 10^5$	$3.0 \times 10^6$
$p$	27.7	217	609	987	1315	1955	2510	5045	8130	9930

hydrides which are brittle in nature [88-90]. However, despite the great effort made in the past two decades, there has been no consensus on the mechanism in general. In the following, only three major mechanisms are reviewed which, from the author's point of view, have received the most experimental support and may play a role in many cases.

### 2.3.1.1 Internal pressure theory

Originally proposed by Zapffe [91], this model states that supersaturated hydrogen atoms precipitate as molecular hydrogen gas in the microvoids or cracks and at the interfaces between nonmetallic inclusions and the matrix metal, exerting an internal pressure which lowers the apparent fracture stress [92].

According to Hirth [7], the equilibrium atomic fraction of hydrogen in iron,  $C$ , in hydrogen gas at a fugacity of  $f$  (in atm) is

$$C = 0.00185\sqrt{f} \exp(-3440/T) \quad (2.13)$$

with  $T$  in K. At low pressures ( $< 200$  atm), fugacity  $f$  can be replaced by pressure  $p$ . At 300 K and 1 atm, eqn.(2.13) gives  $C = 0.02$  appm. Therefore, when the material is supersaturated, say to 20 appm, Eqn.(2.13) gives the corresponding hydrogen fugacity of  $10^6$  atm. Using data listed in Table 2.1 [93], one finds the internal pressure of the precipitated hydrogen to be as high as over 8000 atm, sufficient to create blisters or cracks without external stress. However, crack propagation was observed in dry hydrogen at subatmospheric pressure [94], where one cannot expect such a

degree of supersaturation. The suggestion that moving dislocations can transport hydrogen to the critical sites [95,96] may help extend this theory to be applicable to hydrogen embrittlement in low fugacity hydrogen, but there has been an argument regarding how large this effect could be [97]. Recently, Latanision has concluded that dislocation transport of hydrogen in Ni is limited by grain boundaries. Therefore, no apparent effect could be observed in polycrystalline specimens [98,99].

A critical question with this model is that it cannot explain the reversability of hydrogen embrittlement; i.e., the recovery of mechanical properties after degassing of hydrogen, which is a common feature in many cases.

### **2.3.1.2 The Decohesion Theory**

This model was proposed in the mid-fifties by Troiano [100,101] and developed further by Oriani [36,102]. The idea is that hydrogen dissolved in a steel concentrates in regions of positive hydrostatic component of stress, weakening the cohesive force between metal atoms, permitting the nucleation of a microcrack within the plastic enclave. The crack propagates only when the local tensile stress just equals the local maximum cohesive strength per unit area as reduced by the local hydrogen concentration.

The decohesion model has a degree of semi-quantitative success in describing the static phenomena of hydrogen embrittlement of high strength steels and has been extended to low strength steels by Oriani. However, there has been no direct experimental evidence for hydrogen induced decohesion. It is extremely difficult to devise a feasible experiment to measure the cohesive force between metal atoms in the presence of large amount of dissolved hydrogen.

Theoretical calculations using atomistic computer simulation and a quantum

mechanical approach have been made recently, which suggest that dissolved hydrogen does decrease the force resisting the co-linear separation of metal atoms, so that the basic postulate of the decohesion model is supported by theory [103,104].

### 2.3.1.3 The Localized Slip Theory

Beachem [105] proposed the idea that hydrogen lowers the work required for fracture by enhancing slip in 1972. He suggested that the hydrogen concentrated by the stress field of the crack facilitates severe, localized crack tip deformation; i.e., hydrogen embrittlement is a phenomenon that is brittle in macro-scale but plastic in micro-scale. This idea was resisted for a long time, but now has been widely accepted owing to some unambiguous experimental support.

Lynch [106] noted very small ( $\leq 0.1\mu m$ ) dimples on what have been called cleavage surfaces. Birnbaum et al [107,108] strained thin nickel foils within a high-voltage transmission electron microscope filled with low pressure hydrogen and observed the crack tip *in situ*. They reported direct observations of a highly localized rupture mechanism along active slip planes.

Lynch has detailed this mechanism recently [106], which is shown in Fig.2.5. In the ductile crack growth, the egress of dislocations nucleated from near-crack-tip sources (A), which are exactly on slip planes intersecting crack tips, produces an increment of crack advance,  $\delta a$ . But dislocations from sources (B) and (C) produce only opening or contribute to the general strain ahead of cracks; i.e., most dislocations produce crack blunting rather than crack growth. However, when hydrogen atoms are absorbed between the first few atomic layers, they will weaken interatomic bonds there and thereby facilitate the shear movement of atoms right at the crack tip. Therefore, dislocation nucleation is limited to this small region.

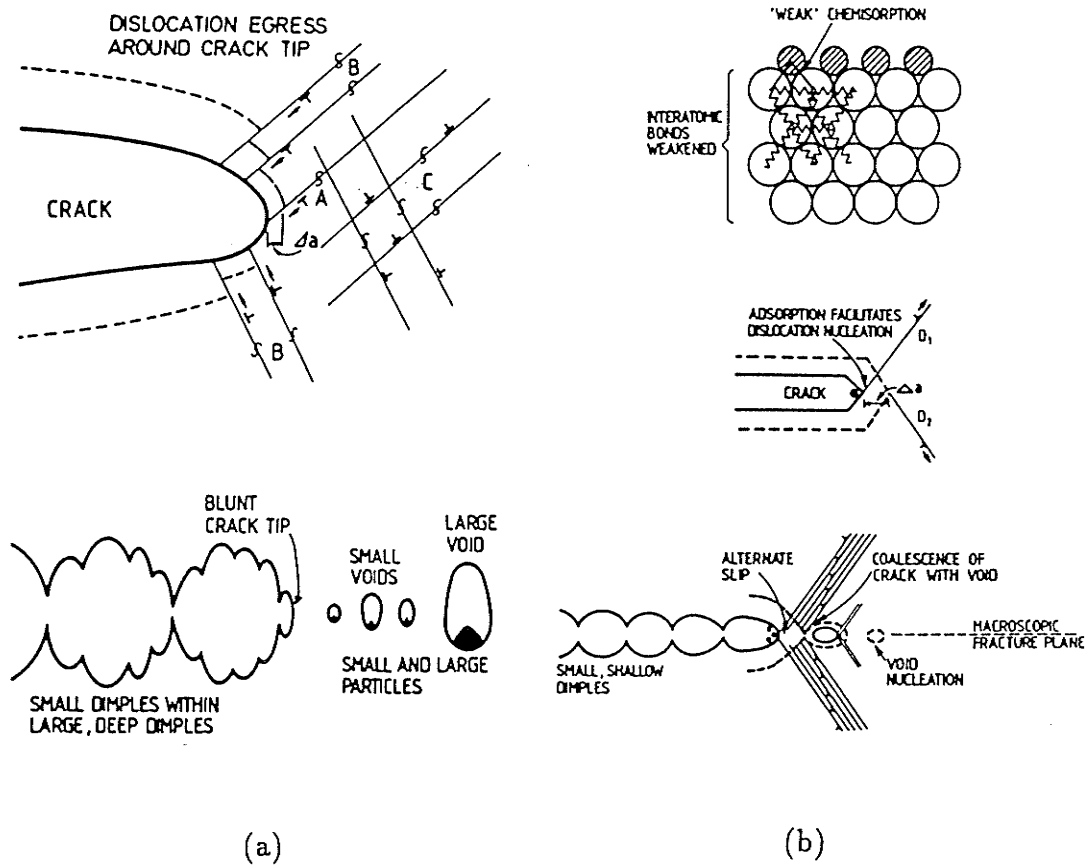


Figure 2.5: Localized-slip mechanism of hydrogen induced cracking: (a) ductile rupture, (b) when hydrogen is present.

All dislocations injected would produce an increment of crack advance through an alternate-slip mechanism. Consequently, less blunting occurs at the crack tip, strains ahead of crack are lower, and voids are formed only just ahead of the crack. This explains the observation of small and shallow dimples on fracture surfaces.

It has been realized by more and more researchers that the decohesion model and localized slip model may not be as competitive as they look, but rather complementary. Oriani [9] argued that the two models may both manifest a somewhat different aspect of the same disturbance of the metal-metal bond caused by hydrogen. If the strength of the atomic bond is reduced by hydrogen, both cleavage and slip may be enhanced. This, from the author's point of view, might be proven by future investigations to be the common ground of all of the above three mechanisms.

### **2.3.2 Mechanisms for Intergranular Cracking**

Since the hydrogen decohesion theory was put forward in the early days of hydrogen embrittlement research, and also since it had been well documented that grain boundaries are fast diffusion paths in metals and alloys, the mechanism of hydrogen induced intergranular cracking seemed to be quite straight forward. However, as the localized slip model of hydrogen embrittlement becomes more and more popular, some researchers started re-thinking the mechanism of hydrogen induced intergranular cracking.

Birnbaum et al [108] investigated hydrogen induced intergranular cracking in Fe, Ni, and IN 903 alloy. Contrary to the generally accepted concepts of hydrogen related intergranular fracture which assume that the fracture occurs in the grain boundary, they observed that the hydrogen related intergranular fracture in these materials occurs in the vicinity of but not in the grain boundary, being a result of highly localized plastic fracture along slip planes which are active in the vicinity

of the boundary. They proposed that the essential difference between intergranular and transgranular fracture modes in hydrogen embrittlement of these systems is in the localization of the hydrogen. Intergranular fracture is observed if the hydrogen concentration at the grain boundary is higher than at other places in the solid.

Lee and Latanision [109] studied hydrogen induced intergranular cracking and the impurity effects in Ni. They proposed a model as shown in Fig.2.6, in which the detrimental effect of impurity segregation is attributed to the enhanced entry of hydrogen at grain boundary intersections with the free surface. According to this idea, as well as Birnbaum's [108], the reason for intergranular fracture in the presence of hydrogen is that hydrogen enters the metal along grain boundaries, which are the loci of the segregated impurities. As pointed out by Morgan and McMahon [110], their model implies that (1) grain boundaries are fast diffusion paths for hydrogen, and (2) the diffusing hydrogen remains in the grain boundaries and is not dispersed into the grain interiors. Therefore, whether hydrogen diffuses more rapidly along grain boundaries becomes an essential issue in understanding the mechanism of hydrogen induced intergranular fracture.

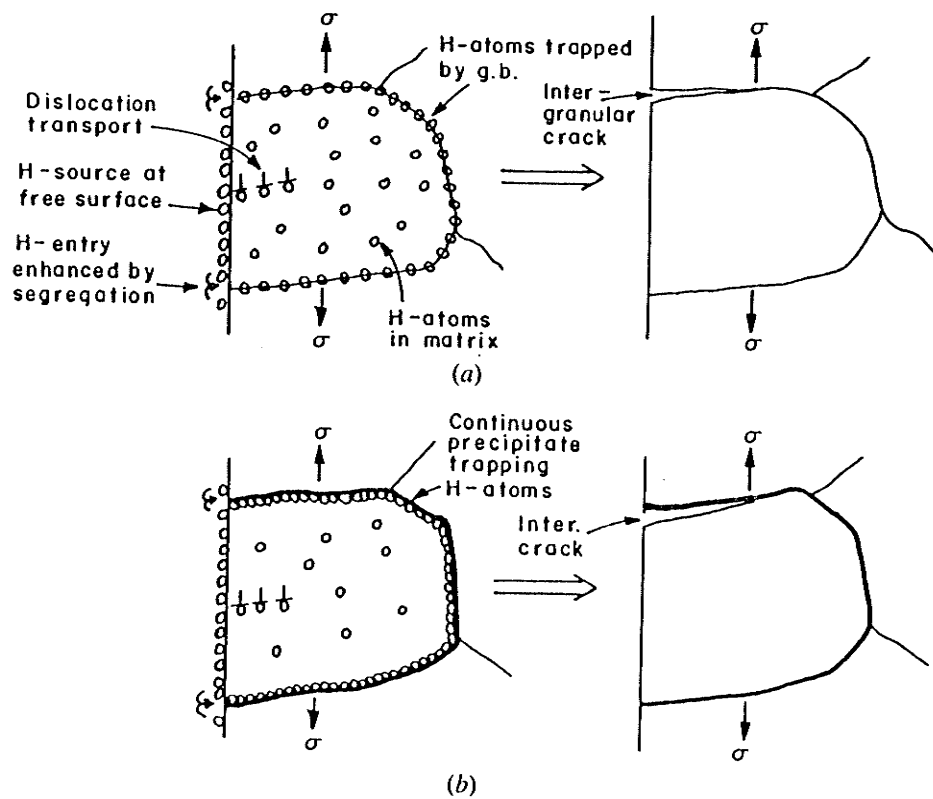


Figure 2.6: Latanision's model for hydrogen induced intergranular fracture in Ni.

## Chapter 3

# Theoretical Modeling of Grain Boundary Diffusion

### 3.1 Geometric Grain Boundary Model

Consider a thin membrane of polycrystalline metal with uniform grain size and initially free from hydrogen. The effect of those grain boundaries parallel to the membrane is neglected. Considering that the volume fraction of grain boundaries is small in most cases, this assumption is reasonable as long as the binding energy is not too high. This is true at least in the nickel–hydrogen system. Secondly, we assume all grain boundaries are perpendicular to the surface of the membrane. This means that the membrane is composed of hexagonal prisms as shown in Figure 3.1. Each of these grain boundary planes is a plane of mirror symmetry; therefore, there will be no net exchange between any particular grain and its neighbors. The problem of determining the concentration in the aggregate is then reduced to determining the concentration of one grain. To facilitate calculation, the hexagonal grain boundary segments are replaced by a tubular cylinder with a thickness equivalent to the grain boundary width as shown in Figure 3.2. The central radius of this equivalent tube is defined as  $L/2$  where  $L$  is the average grain size.

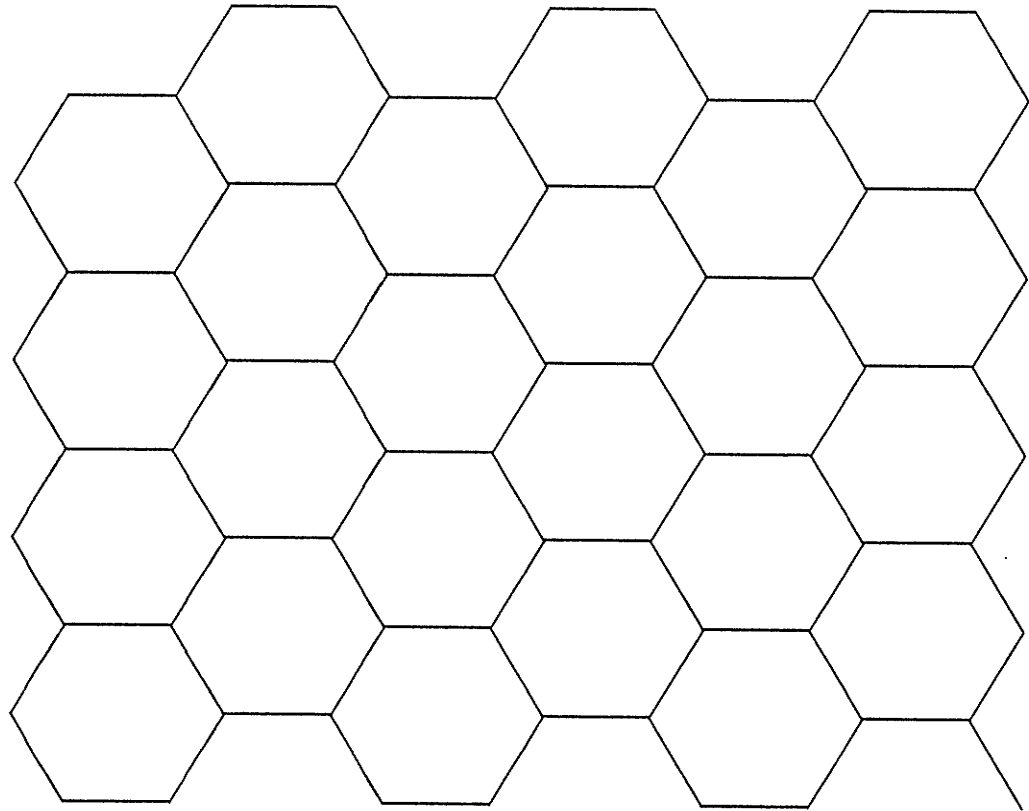


Figure 3.1: Grain boundary aggregate. All grain boundaries are assumed perpendicular to the free surface of the membrane, i.e., into the paper. Those parallel to the surface are neglected.

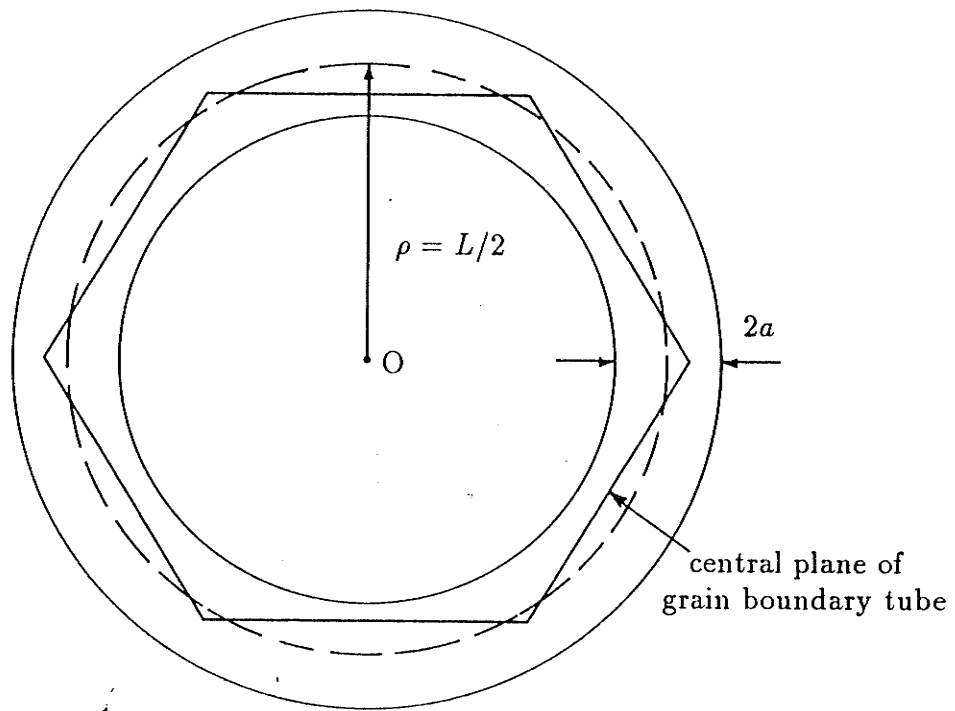


Figure 3.2: The equivalent grain boundary tube.  $z$  direction is into the paper.

In the grain boundary, the concentration  $C_g$  satisfies

$$D_g \nabla^2 C_g = \frac{\partial C_g}{\partial t} \quad (3.1)$$

and within the grain

$$D_l \nabla^2 C_l = \frac{\partial C_l}{\partial t}. \quad (3.2)$$

It is further assumed that the equilibrium distribution of hydrogen in the lattice and grain boundaries follows the Boltzmann statistics; therefore, the boundary conditions at  $\rho = L/2 - a$  are

$$C_l = \frac{1}{s} C_g \quad (3.3)$$

$$D_l \frac{\partial C_l}{\partial \rho} = D_g \frac{\partial C_g}{\partial \rho} \quad (3.4)$$

where  $s$  is the segregation factor which is determined by the binding energy,  $E_b$ :

$$s = \exp(E_b/RT). \quad (3.5)$$

Since the grain boundary width is small compared with the grain diameter even in microcrystalline material, the local curvature should be small. In other words, the two interfaces of a small segment of grain boundary can be considered to be straight and parallel. Therefore, it can be assumed that the central plane of the equivalent grain boundary tube at  $\rho = L/2$  is a plane of mirror symmetry for  $C_g$ ; i.e.

$$C_g = C_g^{(1)}(z, t) + \frac{(\rho - L/2)^2}{2} C_g^{(2)}(z, t) \quad (3.6)$$

which is similar to Whipple's approximation.[77]

Substituting into eqns.(3.1), (3.3) and (3.4) and using eqn.(3.2) one can find a single boundary condition which must be satisfied by  $C_l$  at  $\rho = L/2 - a$ , i.e., at the interface between grain interior and grain boundary itself

$$D_g \left[ \frac{\partial^2 C_l}{\partial \rho^2} + \frac{2}{L} \left( 1 + \frac{L}{2asK} \right) \frac{\partial C_l}{\partial \rho} \right] = (K - 1) \frac{\partial C_l}{\partial t}. \quad (3.7)$$

In the above derivations, the terms of order  $a^2$  and higher have been neglected.

### 3.2 Case 1: Permeation Test

During a permeation test, the boundary conditions for the  $z$  direction are

$$C_l|_{z=0} = C_0 \quad (3.8)$$

$$C_l|_{z=h} = 0 \quad (3.9)$$

where  $h$  is the membrane thickness,  $C_0$  the concentration at the input surface.

Following the standard procedures of solving partial differential equations one can find  $C_l$  to have the following form which satisfies the boundary condition expressed by eqn.(3.7):

$$C_l = C_0 \left\{ 1 - \frac{z}{h} + \sum_{n=1}^{\infty} \sum_{m=1}^{\infty} A_{nm} J_0(\alpha_{nm} \rho) \times \sin \frac{n\pi z}{h} \exp \left[ -D_{lt} \left( \alpha_{nm}^2 + \frac{n^2 \pi^2}{h^2} \right) \right] \right\} \quad (3.10)$$

where  $J_0$  and  $J_1$  are Bessel functions of zero and first order, respectively. Substituting into eqn.(3.7) gives

$$\sum_{n=1}^{\infty} \sum_{m=1}^{\infty} A_{nm} \left\{ (K - 1) D_l \left( \alpha_{nm}^2 + \frac{n^2 \pi^2}{h^2} \right) J_0(\alpha_{nm} L/2) + D_g \frac{\partial^2 J_0(\alpha_{nm} \rho)}{\partial \rho^2} \Big|_{\frac{L}{2}-a} + D_g \frac{\partial J_0(\alpha_{nm} \rho)}{\partial \rho} \Big|_{\frac{L}{2}-a} \left( \frac{2}{L} + \frac{1}{asK} \right) \right\}$$

$$\times \sin \frac{n\pi z}{h} \exp[-D_1 t(\alpha_{nm}^2 + \frac{n^2 \pi^2}{h^2})] = 0 \quad (3.11)$$

This is true only when the content in { } equals zero, i.e.,

$$(K-1)D_1(\alpha_{nm}^2 + \frac{n^2 \pi^2}{h^2})J_0(\alpha_{nm}L/2) + D_g \frac{\partial^2 J_0(\alpha_{nm}\rho)}{\partial \rho^2} \Big|_{\frac{L}{2}-a} + D_g \frac{\partial J_0(\alpha_{nm}\rho)}{\partial \rho} \Big|_{\frac{L}{2}-a} (\frac{2}{L} + \frac{1}{asK}) = 0. \quad (3.12)$$

Using the properties of Bessel functions

$$\frac{dJ_0(x)}{dx} = -J_1(x) \quad (3.13)$$

and

$$J_2(x) - \frac{2J_1(x)}{x} + J_0(x) = 0 \quad (3.14)$$

we obtain the equation which must be satisfied by  $\alpha_{nm}$

$$[\alpha_{nm}^2 - (K-1)\frac{n^2 \pi^2}{h^2}]J_0(\alpha_{nm}L/2) + \frac{\alpha_{nm}}{as}J_1(\alpha_{nm}L/2) = 0. \quad (3.15)$$

The initial condition is

$$C_l|_{t=0} = 0. \quad (3.16)$$

Substituting into eqn.(3.10) yields

$$\sum_{n=1}^{\infty} \sum_{m=1}^{\infty} A_{nm} J_0(\alpha_{nm}\rho) \sin \frac{n\pi z}{h} = -(1-z/h) \quad (3.17)$$

which implies

$$\sum_{m=1}^{\infty} A_{nm} J_0(\alpha_{nm}\rho) = -\frac{2}{n\pi}. \quad (3.18)$$

Multiplying with  $J_0(\alpha_{nm}\rho)\rho$  and integrating from  $\rho=0$  to  $L/2-a$  gives

$$A_{nm} = \frac{-8[J_1(\alpha_{nm}L/2) + as\alpha_{nm}J_0(\alpha_{nm}L/2)]}{n\pi L\alpha_{nm}\{(1 + \frac{4as}{L})[J_0(\alpha_{nm}L/2)]^2 + [J_1(\alpha_{nm}L/2)]^2\}}. \quad (3.19)$$

It should be pointed out that the eigenfunctions  $\alpha_{nm}$  and  $\alpha_{nm}$  are not orthogonal. The derivation of eqn.(3.19) is more involved than orthogonal conditions.

### 3.2.1 Calculating the Permeation Current

The density of the permeation current,  $i_{total}$ , equals the total current through an individual grain divided by the total area of the grain. Thus, it can be expressed as

$$i_{total} = \frac{I_l + I_g}{\pi(\frac{L}{2})^2} \quad (3.20)$$

where  $I_l$  and  $I_g$  are the permeation currents through the grain interior and grain boundaries, respectively.

For each grain, we have

$$I_l = FD_l \int_0^{L/2-a} 2\pi \left. \frac{\partial C_l}{\partial z} \right|_{z=h} \rho d\rho \quad (3.21)$$

and

$$I_g = FD_g \int_{L/2-a}^{L/2} 2\pi \left. \frac{\partial C_g}{\partial z} \right|_{z=h} \rho d\rho \quad (3.22)$$

where  $F$  is the Faraday constant. Again, since the grain boundary width is small,  $C_g$  changes little across the grain boundary. Therefore, from eqn.(3.3) it can be approximated that

$$\left. \frac{\partial C_g}{\partial z} \right|_{z=h} = s \left. \frac{\partial C_l}{\partial z} \right|_{\rho=L/2-a, z=h} \quad (3.23)$$

Substituting into eqn.(3.22) yields

$$I_g = as\pi LFD_g \left. \frac{\partial C_l}{\partial z} \right|_{\rho=L/2-a, z=h} \quad (3.24)$$

Using eqn.(3.10), one obtains the final form of the total permeation current density:

$$\begin{aligned} i_{total} = & \frac{4FD_lC_0}{h} \left\{ \frac{1}{4} + \frac{asK}{L} - \sum_{n=1}^{\infty} \sum_{m=1}^{\infty} (-1)^n \left[ \frac{J_1(\alpha_{nm}L/2)}{\alpha_{nm}} + asK J_0(\alpha_{nm}L/2) \right] \right. \\ & \left. \times \frac{n\pi}{L} A_{nm} \exp[-D_l t(\alpha_{nm}^2 + \frac{n^2\pi^2}{h^2})] \right\}. \end{aligned} \quad (3.25)$$

### 3.2.2 Calculating the Lag Time

In the literature, the time lag method has been widely used to determine the diffusion coefficient from a permeation test. The total amount of diffusing substance,  $Q$ , which has passed through the membrane in time  $t$  can be obtained by integrating  $i_{total}$  with respect to  $t$ . The lag-time is, by definition, obtainable from the equation

$$Q|_{t \rightarrow \infty} = 0. \quad (3.26)$$

For lattice diffusion, we have [111]

$$t_{lag} = \frac{h^2}{6D_l}. \quad (3.27)$$

The solution becomes more complicated if grain boundary enhanced transport is taken into account. According to eqn.(3.26), one can derive

$$t_{lag} = \sum_{n=1}^{\infty} \sum_{m=1}^{\infty} (-1)^n \frac{4n\pi A_{nm}}{LD_l(\alpha_{nm}^2 + \frac{n^2\pi^2}{h^2})} \frac{[\frac{J_1(\alpha_{nm}L/2)}{\alpha_{nm}} + asK J_0(\alpha_{nm}L/2)]}{1 + \frac{4asK}{L}} \quad (3.28)$$

This can be further simplified by using eqn.(3.15) to eliminate the  $A_{nm}$ 's

$$t_{lag} = \sum_{n=1}^{\infty} \sum_{m=1}^{\infty} \frac{(-1)^n 32h^2 [J_1(\alpha_{nm}L/2) + as\alpha_{nm}J_0(\alpha_{nm}L/2)]^2}{(L + 4asK)n^2\pi^2\alpha_{nm}^2 D_l [(L + 4as)J_0^2(\alpha_{nm}L/2) + LJ_1^2(\alpha_{nm}L/2)]} \quad (3.29)$$

### 3.3 Case 2: Penetration Test

When hydrogen is charged into the membrane from both sides, the boundary conditions for the  $z$  direction are

$$\left. \frac{\partial C_l}{\partial z} \right|_{z=h/2} = 0 \quad (3.30)$$

$$C_l|_{z=0} = C_l|_{z=h} = C_0. \quad (3.31)$$

where again  $h$  is the membrane thickness,  $C_0$  the concentration at the input surface.

A similar procedure gives

$$C_l = C_0 \left\{ 1 + \sum_{n=1}^{\infty} \sum_{m=1}^{\infty} A_{nm} J_0(\alpha_{nm}\rho) \sin \frac{(2n-1)\pi z}{h} \times \exp[-D_l t (\alpha_{nm}^2 + \frac{(2n-1)^2\pi^2}{h^2})] \right\}. \quad (3.32)$$

Substituting into eqn.(3.7) gives the following equation from which  $\alpha_{nm}$ 's can be calculated:

$$[\alpha_{nm}^2 - (K - 1)\frac{(2n - 1)^2\pi^2}{h^2}]J_0(\alpha_{nm}L/2) + \frac{\alpha_{nm}}{as}J_1(\alpha_{nm}L/2) = 0. \quad (3.33)$$

The initial condition requires that

$$\sum_{n=1}^{\infty} \sum_{m=1}^{\infty} A_{nm} J_0(\alpha_{nm}\rho) \sin \frac{(2n - 1)\pi z}{h} = -1 \quad (3.34)$$

indicating

$$\sum_{m=1}^{\infty} A_{nm} J_0(\alpha_{nm}\rho) = -\frac{4}{(2n - 1)\pi}. \quad (3.35)$$

Multiplying with  $J_0(\alpha_{nm}\rho)\rho$  and integrating from  $\rho=0$  to  $L/2 - a$  gives

$$A_{nm} = \frac{-16[J_1(\alpha_{nm}L/2) + as\alpha_{nm}J_0(\alpha_{nm}L/2)]}{(2n - 1)\pi L\alpha_{nm}\{(1 + \frac{4as}{L})[J_0(\alpha_{nm}L/2)]^2 + [J_1(\alpha_{nm}L/2)]^2\}}. \quad (3.36)$$

If we assume that when hydrogen concentration in grain boundaries reaches a critical value,  $C_g^*$ , the fracture mode will change to intergranular, then the penetration depth of this intergranular cracking,  $z^*$ , can be numerically calculated from

$$C_g^* = SC_0\{1 + \sum_{n=1}^{\infty} \sum_{m=1}^{\infty} A_{nm} J_0(\alpha_{nm}L/2) \sin \frac{(2n - 1)\pi z^*}{h} \times \exp[-D_1 t(\alpha_{nm}^2 + \frac{(2n - 1)^2\pi^2}{h^2})]\}. \quad (3.37)$$

# Chapter 4

## Theoretical Results and Discussion

### 4.1 Permeation Curves

The FORTRAN programs used in the following calculations are listed in Appendix A. All results were obtained on an Amdahl System at the Computer Center, University of Manitoba. A data bank for Bessel functions is needed.

#### 4.1.1 Comparison with Literature Data

Since predicted permeation curves are based on eqn.(3.10), it is necessary to verify this equation before discussion of the permeation curves. The present model should be able to accommodate the case of a single isolated grain boundary in a semi-infinite system; i.e., Whipple's model [77]. In this case,  $\sqrt{D_1 t}$  is small compared to the grain size and the membrane thickness. Therefore, the boundary condition at  $Z = h$  is inconsequential and there should be no interaction with adjacent grain boundaries. Whipple has calculated this situation for  $K \gg 1$ . Some calculated results of the present model are compared with the results of Whipple in Figure 4.1. It can be seen that all data points (circles) calculated from eqn.(3.10)

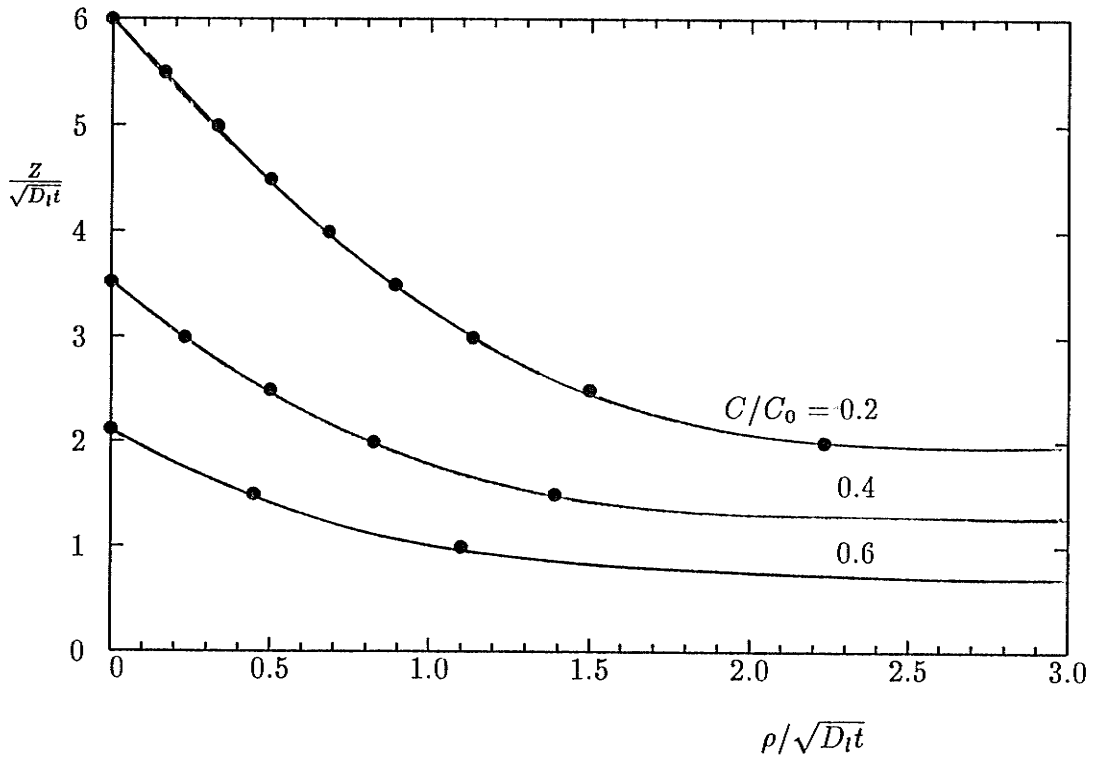


Figure 4.1: Comparison of the present theory with that of Whipple [77] for  $K = 10^6$  and  $S = 1$ . The circles are calculated from eqn.(3.10) for  $K \times S = 10^6$ . The solid curves are Whipple's results.

fall on Whipple's curves. This not only verifies eqn.(3.10) but also suggests that Whipple's model can be considered a special case of the present model. It is therefore concluded that the present model can be used in cases where  $K \gg 1$ .

Some predicted curves calculated by computer from eqn.(3.25) for several  $K$  values are shown in Figure 4.2. As a check, the curve for  $K = 1$  was obtained both from eqn.(3.25) and that for lattice diffusion [111]. The two curves were found exactly coincident. This indicates the validity of the present solution in cases where  $K$  is small. Therefore, the present model can be used for a large range of  $K$  ratio.

It is interesting to find from the computer calculated results that although the membrane thickness appears in eqn.(3.15) while the lattice diffusivity and the time do not, the configuration of a permeation curve does not change with the value of  $D_l$  or  $h$  if the permeation flux is normalized by its steady state value and the time reduced to  $D_l t/h^2$ . This is just like in the case of conventional bulk diffusion. Therefore, all calculation results are shown in normalized flux vs reduced time. Nevertheless, data used in the calculation are also shown in the figures.

#### 4.1.2 Effect of $K$ Ratio

As shown in Figure 4.2, a higher  $K$  value shifts the normalized permeation curve to the left. On the other hand, from eqn.(3.25), when  $t \rightarrow \infty$ , i.e. at the steady state,

$$i_s = i_{total}|_{t \rightarrow \infty} = \frac{FD_l C_0}{h} \left\{ 1 + \frac{4asK}{L} \right\}. \quad (4.1)$$

We note that the first term of the right hand side is the contribution of the lattice and the second that of the grain boundaries. Therefore, a higher  $K$  value also raises

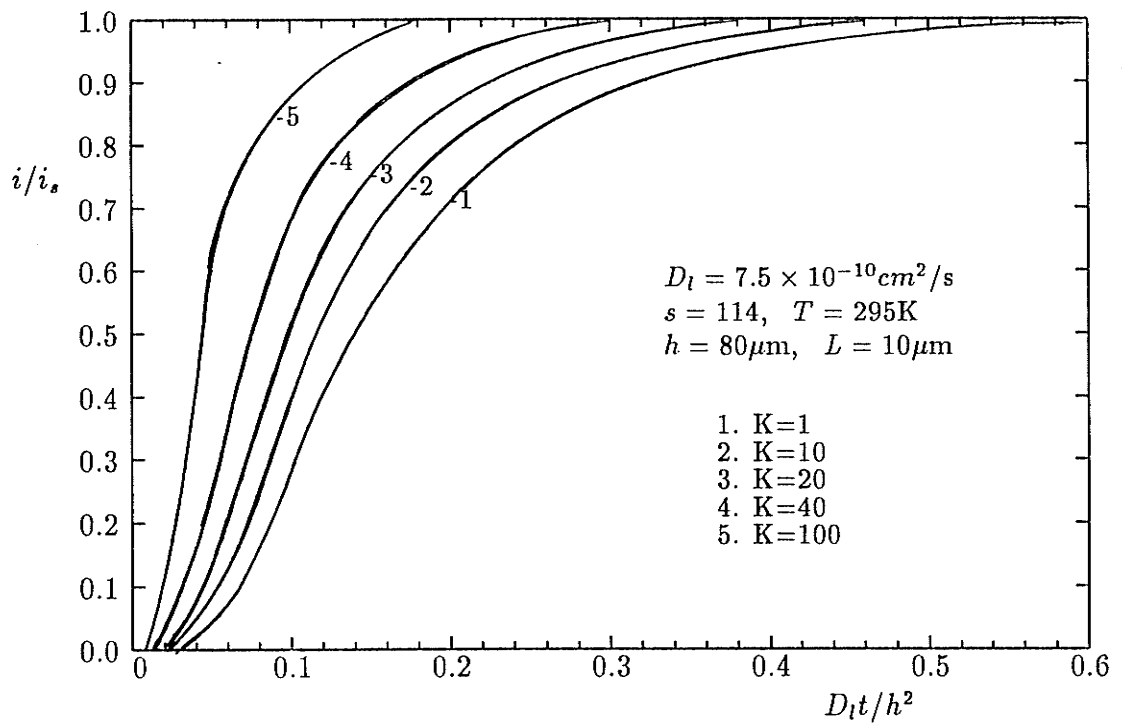


Figure 4.2: Normalized permeation rate vs reduced time for various  $K$  values.

the curve as shown in Figure 4.3. However, since  $a$  is very small, this effect can be seen only when  $s/L$  is sufficiently large. In Ni,  $s$  is in the order of 100 at room temperature. If grain size is  $10\mu\text{m}$ , only when grain boundary transport is dominant ( $K > 40$ ) can one expect a detectable increase in  $i_s$ .

On the other hand, it should be emphasized here that one has to be cautious to conclude a high  $K$  ratio just because a higher  $i_s$  is observed in fine grained membranes. As revealed by eqn.(4.1), the segregation factor contributes to  $i_s$  exactly the same as the  $K$  ratio does. Therefore, the effect of the segregation factor should be distinguished from that of the ratio of the two diffusivities when experimental results are analyzed.

### 4.1.3 Effect of Segregation Factor $s$

An advantage of the present model over Whipple's model is that it takes the segregation factor into account. When the grain boundary concentration approaches saturation, the equilibrium state should be expressed with a Fermi-Dirac distribution. However, this will make the diffusion equations nonlinear. Therefore, the Boltzmann equation was used in this study. For hydrogen diffusion in nickel, the binding energy of hydrogen in the grain boundary is relatively small, being suggested as 11.6 kJ/mol [13], so if the surface concentration on the incoming side is not too high, a Boltzmann distribution is a fair approximation.

From eqn.(4.1) and Figure 4.4, it can be seen that a higher  $s$  value has similar effects as a higher  $K$ ; i.e. raising the permeation curves and shifting them to the left. From eqn.(3.10), however, it is apparent that changes in  $s$  and  $K$  are not necessarily linearly proportional. This can also be seen from Fig.4.1. The calculated concentration profiles using the values of  $K = 10^4$  and  $S = 100$  or the values

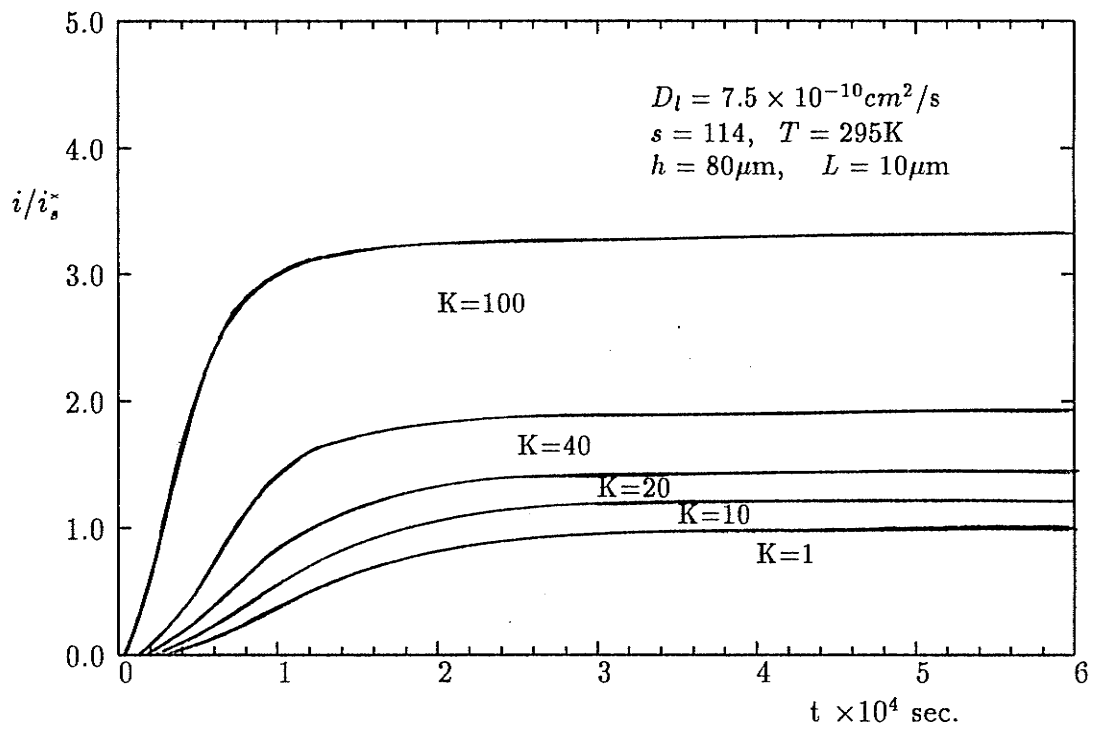


Figure 4.3: Permeation rate vs time for different  $K$  values.  $i_s^*$  is the steady state current corresponding to the bulk diffusion.

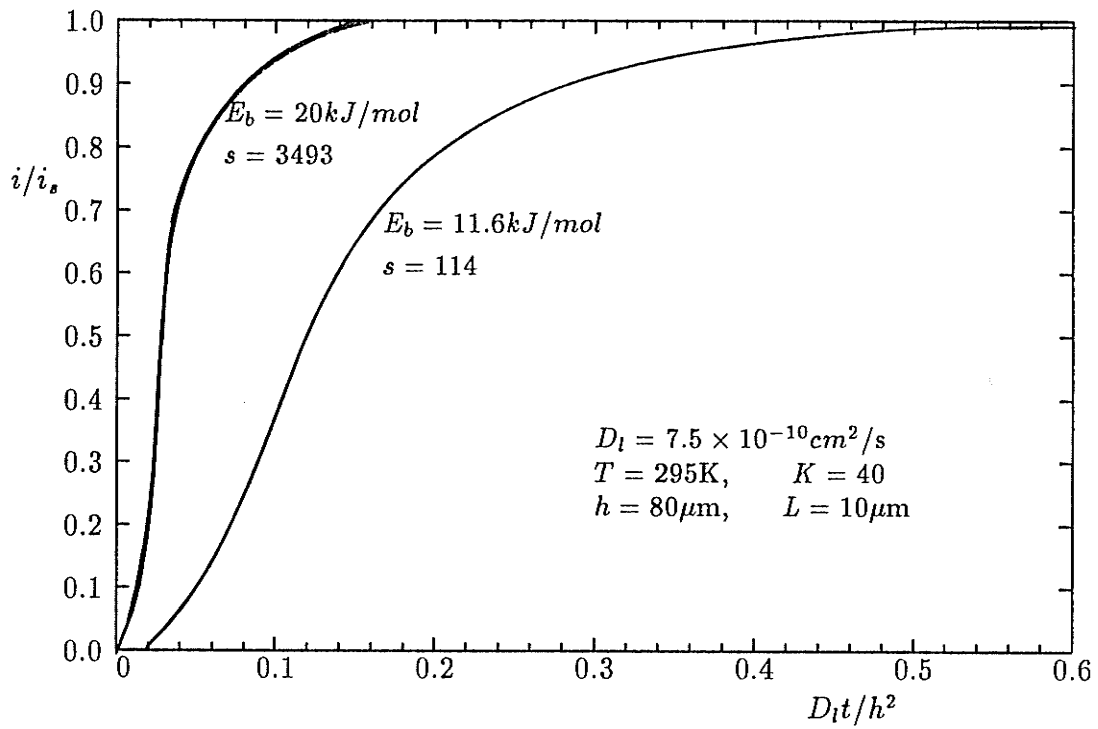


Figure 4.4: Normalized permeation rate vs reduced time with different binding energy.

of  $K = 10^6$  and  $S = 1$  are exactly identical; i.e., the concentration contours are determined by the product of the segregation factor and the value of the  $K$  ratio, a decrease in  $K$  can be compensated by an increase in the segregation factor. However, this is true only when grain boundary diffusion is dominant; i.e.,  $K$  is no less than  $10^3$ . When  $K$  is small, an increase in the segregation factor cannot compensate a decrease in  $K$ . This is quite apparent since when  $K$  approaches unity, the diffusion process in the lattice can be treated as independent of that in grain boundaries and the problem simply reduces to lattice diffusion. Even in that case, as long as  $s/L$  is sufficiently large, one still expects to see a larger  $i_s$  in fine grained membranes. That is, a higher  $i_s$  without a notable shift to the left in the recorded permeation curve must be a result of the segregation effect.

#### 4.1.4 Effect of Grain Boundary Width

Throughout the derivations in Chapter 3, it is noted that the half grain boundary width,  $a$ , always occurs with the segregation factor,  $s$ ; therefore, they have exactly the same effect; i.e. a higher value of  $s$  has the same effect as a wider grain boundary. Thus, the curve on the left in Fig.4.4 can be considered as similar to the case with the same segregation factor as the curve on the right but with a grain boundary width about 30 times greater.

#### 4.1.5 The Break-through Time

There seems to be confusion in the literature regarding the break-through time. By definition, the break-through time is the intersection of the tangent at the inflection point on the anodic current with its original background level [17]. For bulk diffusion with constant input concentration, the break-through time,  $t_b$ , can be

shown to be

$$t_b = 0.0507 \frac{h^2}{D_l}. \quad (4.2)$$

Since the permeation curve has an s-shape,  $t_b$  is always greater than actual break-through time,  $t_a$ , which is the point when the permeation flux becomes detectable by the monitoring system and can be derived mathematically as follows. The total diffusing substance  $Q$  which has passed through the membrane in time  $t$  is

$$\frac{Q}{LC_0} = \frac{D_l t}{h^2} - \frac{1}{6} - \frac{2}{\pi^2} \sum_{n=1}^{\infty} \frac{(-1)^n}{n^2} \exp\left(\frac{-n^2 \pi^2 D_l t}{h^2}\right). \quad (4.3)$$

Let  $Q = 0$ , we have

$$t_a = \frac{h^2}{D_l} \left[ \frac{1}{6} + \frac{2}{\pi^2} \sum_{n=1}^{\infty} \frac{(-1)^n}{n^2} \exp\left(\frac{-n^2 \pi^2 D_l t_a}{h^2}\right) \right]. \quad (4.4)$$

This equation can be solved by iteration which yields

$$t_a = 0.0203 \frac{h^2}{D_l}. \quad (4.5)$$

It is clear that in the experiment, the measured actual break-through time depends on the detecting sensitivity of the monitor. Repeating the same procedure with different sensitivities, the constant in eqn.(4.5) was found to be 0.0223 and 0.0284 for detecting sensitivities of 0.01% and 0.1%, respectively. Thus,  $t_a$  is substantially smaller than  $t_b$  for common monitoring techniques. Some researchers [14,27] appear to have neglected this fact and used  $t_b$  instead of  $t_a$  as a criterion to determine if hydrogen atoms have reached the downstream surface via lattice diffusion.

For the case of enhanced transport by grain boundaries, the actual break-through time,  $t_{ag}$ , will be greatly reduced from that for lattice diffusion alone. Since

there is no simple equation for  $t_b$  in the present model, several  $R$  ratios are calculated and listed in Table 4.1 and Table 4.2 where

$$R = \frac{t_{ag}}{t_a}. \quad (4.6)$$

It can be seen that a high  $K$  ratio or a large binding energy combined with a small grain size results in a single break-through time which could be a small fraction of that for lattice diffusion. This is also shown in Figure 4.5 for a grain size of  $10\mu\text{m}$ . One can see that the larger the product of  $s$  and  $K$ , the more left the predicted curves. Same is true for coarser grained membranes. However, when grain size is smaller, i.e.  $1\mu\text{m}$ ,  $K$  has a stronger effect on  $t_{ag}$  than  $s$  does. For example,  $t_{ag}$  is about half ( $R=0.0508$ ) for  $K=100$  and  $s=114$  of that ( $R=0.1125$ ) for  $K=10$  and  $s=3493$ .

#### 4.1.6 Time Lag Method for Measuring the Diffusion Coefficient

As shown in Chapter 3, there is no simple equation for  $t_{lag}$  for the case of enhanced transport by grain boundaries. However, from eqn.(3.29) one can write

$$t_{lag} = \beta \frac{h^2}{D_l} \quad (4.7)$$

where

$$\beta = \sum_{n=1}^{\infty} \sum_{m=1}^{\infty} \frac{(-1)^n 32 [J_1(\alpha_{nm}L/2) + as\alpha_{nm}J_0(\alpha_{nm}L/2)]^2}{(L + 4asK)n^2\pi^2\alpha_{nm}^2 [(L + 4as)J_0^2(\alpha_{nm}L/2) + LJ_1^2(\alpha_{nm}L/2)]}. \quad (4.8)$$

Several  $\beta$  values are calculated and shown in Table 4.3 and Table 4.4. Again, it

Table 4.1: Calculated  $R$  ratios of actual breakthrough time to that without enhanced grain boundary transport. Detecting sensitivity is 0.1%. Binding energy is 11.6 kJ/mol.

$L$ ( $\mu\text{m}$ )	$K = 1$	$K = 10$	$K = 20$	$K = 40$	$K = 100$
0.1	1.0000	0.1378	0.0706	0.0355	0.0144
1.0	1.0000	0.3752	0.2211	0.1207	0.0508
10	1.0000	0.8310	0.6934	0.5107	0.2640
100	1.0000	0.9773	0.9450	0.8587	0.5545
1000	1.0000	0.9983	0.9934	0.9789	0.8669

Table 4.2: Calculated  $R$  ratios of actual breakthrough time to that without enhanced grain boundary transport. Detecting sensitivity is 0.1%. Binding energy is 20 kJ/mol.

$L$ ( $\mu\text{m}$ )	$K = 1$	$K = 10$	$K = 20$	$K = 40$	$K = 100$
1	1.0000	0.1125	0.0566	0.0284	0.0113
10	1.0000	0.1893	0.0899	0.0402	0.0138
30	1.0000	0.2435	0.1041	0.0431	0.0142
100	1.0000	0.2943	0.1165	0.0455	0.0147

Table 4.3: Calculated  $\beta$  values for various  $K$  ratios and grain sizes. Binding energy is 11.6 kJ/mol ( $s = 114$ ).

$L$ ( $\mu\text{m}$ )	$K = 1$	$K = 10$	$K = 20$	$K = 40$	$K = 100$	$K = 10^*$
0.1	0.1667	0.0230	0.0118	0.0059	0.0024	0.0167
1.0	0.1667	0.0625	0.0369	0.0203	0.0086	0.0188
10	0.1667	0.1389	0.1172	0.0893	0.0521	0.0355
100	0.1667	0.1633	0.1598	0.1531	0.1361	0.1050
1000	0.1667	0.1663	0.1659	0.1652	0.1630	0.1568

\*  $E_b = 20$  kJ/mol

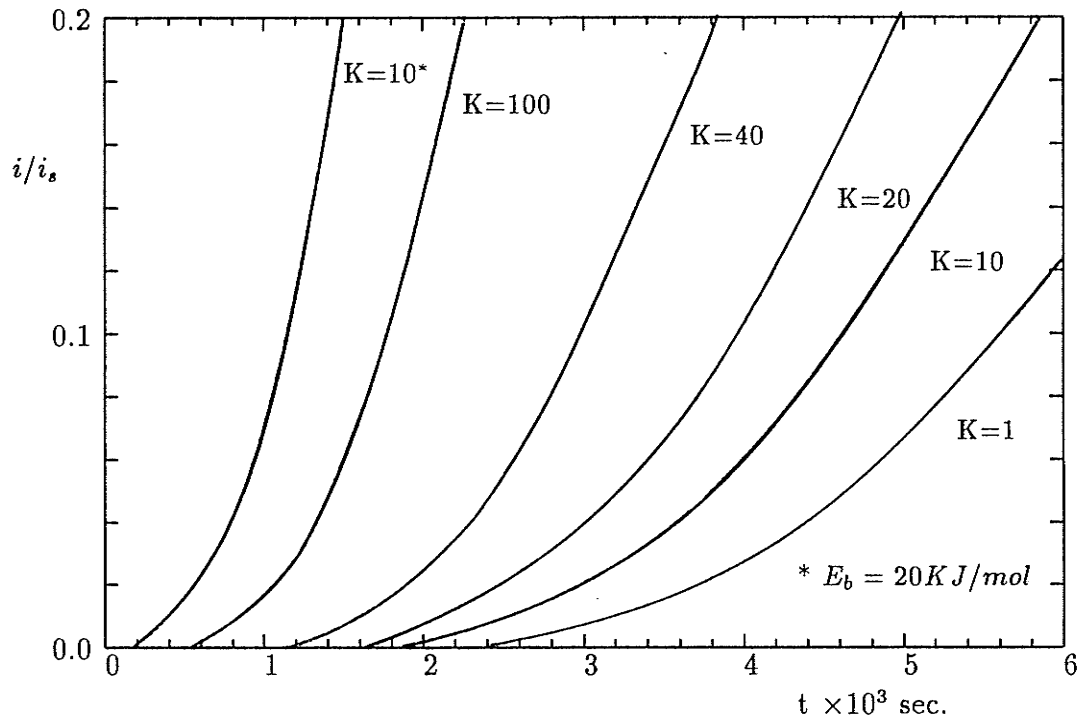


Figure 4.5: Early stage of permeation curves shown in Figure 4.2.

Table 4.4: Calculated  $\beta$  values for  $K=0$  with different grain size and binding energy.

$E_b$ (KJ/mol)	$L = 0.1\mu\text{m}$	$L = 1.0\mu\text{m}$	$L = 10\mu\text{m}$	$L = 100\mu\text{m}$
11.6	0.5451	0.2045	0.1705	0.1670
20.0	70.86	1.331	0.2831	0.1782

can be seen that when grain size is as small as  $1\mu\text{m}$ ,  $K$  has a stronger effect on the lag-time than the segregation factor does. It should be noted that  $K$  has been set at zero in Table 4.4. This does not mean that  $D_g$  is zero, in which case the problem reduces to that of bulk diffusion alone. The zero value of  $K$  implies that  $D_g$  is many orders of magnitude smaller than  $D_l$ , where grain boundaries have become saturable traps for hydrogen. As can be seen from Table 4.4, if the binding energy is high, grain boundaries can greatly retard hydrogen transport in the material in fine grained specimens ( $< 10\mu\text{m}$ ). However, for the Ni-H system, this effect will not be observed in the ordinary range of grain sizes ( $> 1\mu\text{m}$ ).

Eqn.(3.29) can also be written

$$t_{lag} = \frac{h^2}{6D_{\text{eff}}} \quad (4.9)$$

where

$$D_{\text{eff}} = \frac{1}{6\beta} \times D_l. \quad (4.10)$$

Therefore, if one uses the time lag method to determine the diffusion coefficient where grain boundary enhanced transport does occur, the measured diffusion coefficient,  $D_{\text{eff}}$ , will be larger than the lattice diffusion coefficient since  $6\beta < 1$ . Obviously, the upperbound of  $1/6\beta$  is set by the value of  $K$ . It is seen from Table 4.3 that when  $K = 10$ ,  $L=0.1\mu\text{m}$ , and  $E_b=20$  kJ/mol,  $1/6\beta = K$ ; i.e., C-kinetics has been reached (see section 2.2.3.1).

It is noted that Tables 4.1 and 4.3 are identical except for a constant factor of 6; i.e., multiplying a figure in Table 4.3 by 6 yields the number at the corresponding location in Table 4.1. Further calculations have confirmed that this is not a special exception. In other words, if the detecting sensitivity used to obtain

Table 4.1 is changed to some other value, results will be the same. This implies that all calculated curves in Fig.4.2 are similar curves. This seems to suggest that, in order to reveal so-called fast grain boundary transport, it is not more helpful to detect early stages of a permeation test than to simply find the lag-time. However, since the absolute value of  $i_s$  also increases with  $K$ , a higher detecting sensitivity results in an earlier observation of the breakthrough, which is beneficial for revealing grain boundary transport.

It is inconvenient to use eqn.(3.29) to obtain  $t_{lag}$ . Substituting into eqn.(3.25) and using eqn.(3.26) yields the following equation for several sets of parameters as shown in Table 4.5:

$$i_{total}|_{t=t_{lag}} / i_s \approx 0.616 \quad (4.11)$$

Thus, no matter what role grain boundaries may play in enhancing the mass transport of hydrogen, the lag-time can always be obtained by noting the time at which the permeation flux is 0.616 times the steady state value.

#### 4.1.7 Maximum Grain Size to Reveal Grain Boundary Transport

One of the primary objectives of the present study was to determine the maximum grain size above which the effect of grain boundaries on the diffusion process cannot be detected in conventional experiments. A set of curves for different grain sizes are shown in Figure 4.6. Since  $K$  is not expected to be large for the case of interstitial lattice diffusion,  $L$  has to be quite small if enhanced transport of hydrogen by grain boundaries is to be detected. For the case of nickel, the grain size has to be as small as  $10\mu\text{m}$ . In such derivations we have used a rather small binding en-

Table 4.5: Calculated permeation rates at lag-time. Binding energy is 11.6KJ/mol.

$L$ ( $\mu\text{m}$ )	$K = 1$	$K = 10$	$K = 20$	$K = 40$	$K = 100$	$K = 10^*$
1	0.6168	0.6168	0.6168	0.6166	0.6164	0.6168
10	0.6168	0.6167	0.6167	0.6164	0.6155	0.6153
100	0.6168	0.6167	0.6165	0.6162	0.6143	0.6102
1000	0.6168	0.6167	0.6166	0.6166	0.6164	0.6149

\*  $E_b = 20\text{KJ/mol}$

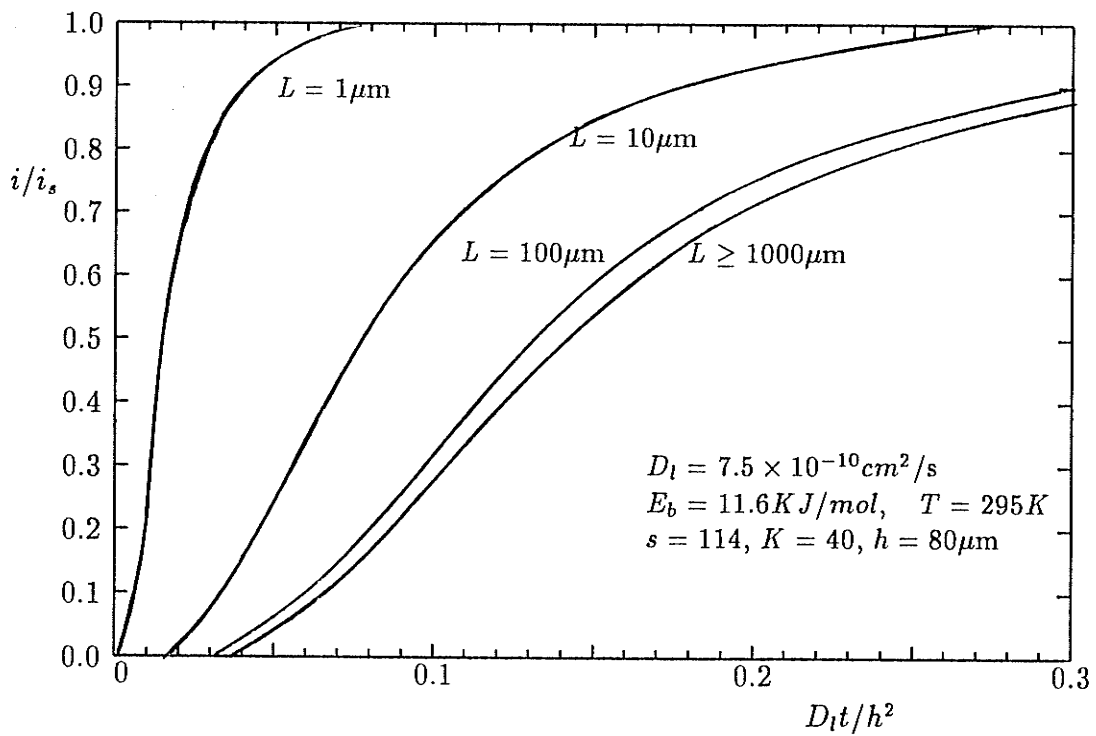


Figure 4.6: Normalized permeation rate vs reduced time for various grain sizes.

ergy (11.6 kJ/mol) and assumed the narrowest grain boundary width ( $5 \times 10^{-10}$  m). However, in the literature a higher value for the binding energy of hydrogen in grain boundaries is sometimes suggested [7], as is a greater grain boundary width [13]. This would make the enhanced transport of hydrogen by grain boundaries more apparent and thus easier to detect. Therefore, we conclude that a grain size of  $10\mu\text{m}$  in most metal-hydrogen systems is capable of revealing enhanced transport of hydrogen by grain boundaries if grain boundaries are indeed fast diffusion paths. This conclusion explains why some researchers found no grain size effect on measured diffusivities since grain sizes used in their work were of the order of  $100\mu\text{m}$  [82-84]. Also, for those investigations in which grain boundary enhanced transport is reported [14,20,77], the value of  $K$  would have to be very large ( $K \gg 40$ , Fig.4.6) which is questionable where lattice diffusion occurs interstitially.

#### 4.1.8 Early Stages of the Transient

Figure 4.7 shows the relative contributions of grain boundary and lattice diffusion for fine grained nickel. It is clear that for this case, the grain boundaries play a relatively more important role than the lattice at all stages. In the very early stages, the grain boundary contribution is more significant than in the later stages. This is due to the fact that the first breakthrough occurs at the grain boundary areas and then spreads to grain interior areas on the downstream surface. It is seen that the relative contribution of grain boundaries has become constant well before the steady state is established. Thus, a high  $K$  value will not result in an early saturation of permeation flux entirely from grain boundaries as reported by Tsuru et al [14]. That situation is possible only when grain boundary and lattice diffusion processes are totally independent, or in other words, where there is no leakage from

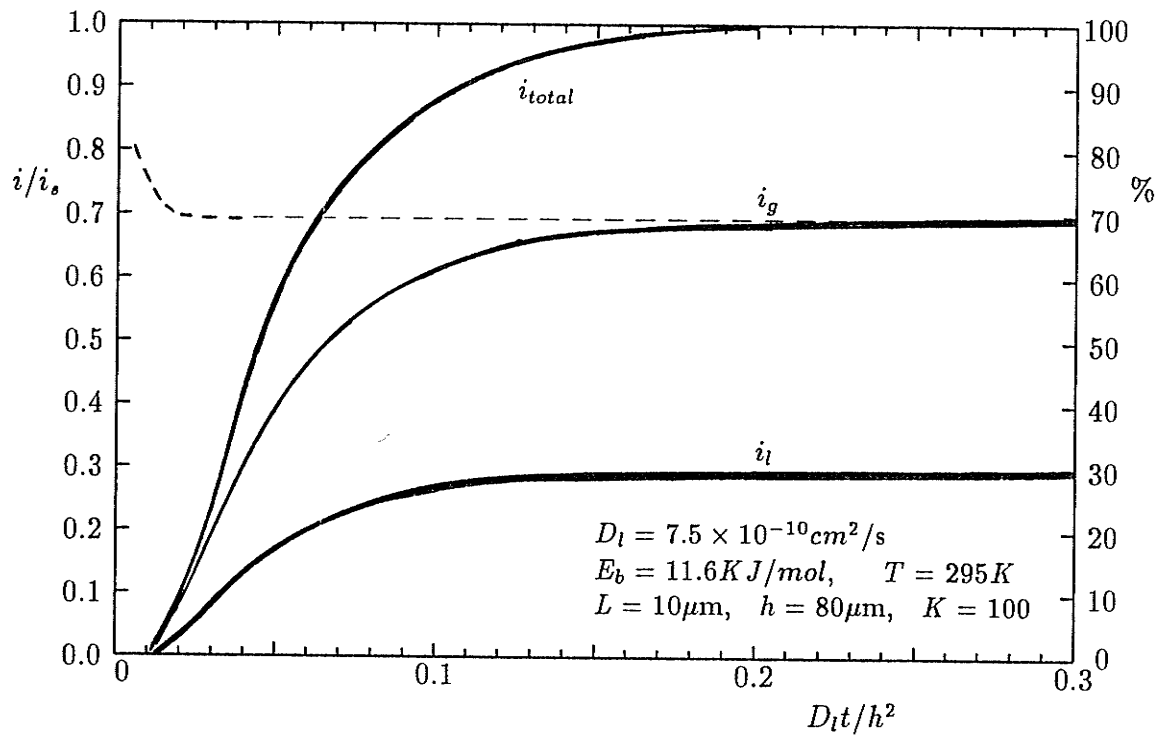


Figure 4.7: Normalized permeation rates from grain boundary areas and the grain interiors for  $K = 100$  where grain boundary transport becomes dominant. ---: Percentage of grain boundary contribution.

grain boundaries to grain interiors. In reality, however, there must be some kind of partitioning even if the equilibrium state could not be established.

## 4.2 Penetration Curves

The penetration depth of the critical concentration for grain boundaries to fracture can be revealed experimentally by the measurement of intergranular cracking depth in membranes fractured at low temperature to avoid redistribution of hydrogen. In order to reveal fast transport by grain boundaries, the experiment is usually performed under such conditions that [77]

$$\frac{(K - 1)as}{\sqrt{D_l t}} \gg 1.0. \quad (4.12)$$

The above equation means that the time should be small since  $K$  is not expected to be large for the case of hydrogen diffusion where  $D_l$  is large. However, a small time means that a large experimental error can be involved. This may well be the reason that Birnbaum's data were unreliable.

The calculated penetration curves using the new model are shown in Fig.4.8 and Fig.4.9 for two grain sizes, where  $C_g^* = 0.2$ ,  $h=0.02$  cm,  $D_l=7.5 \times 10^{-10}$  cm<sup>2</sup>s<sup>-1</sup>, and  $E_b = 11.6$  kJ/mol. It is seen that the time for the center of a membrane to fracture intergranularly is also sensitive to the value of  $K$  ratio especially for fine grained specimens. If grain boundaries play a key role in the transport of hydrogen, complete intergranular cracking will be observed after a charging period significantly shorter (Curve 3) than required by lattice diffusion alone (Curve 1). Therefore, the theoretical calculations have revealed a means to detect the enhanced transport of hydrogen by grain boundaries in which large experimental errors can be avoided.

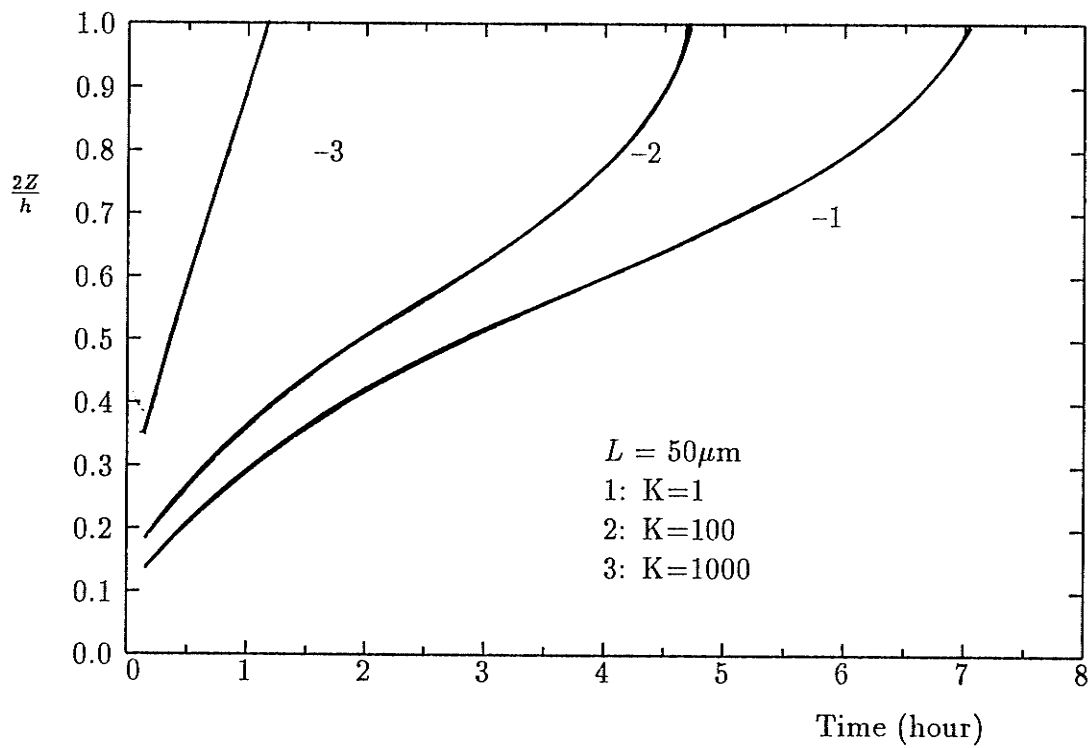


Figure 4.8: Calculated penetration curves. Grain size  $50\mu\text{m}$ . Curve 1 represents the lattice diffusion. The contribution from the grain boundaries is 50% for curve 2 and >99% for curve 3.

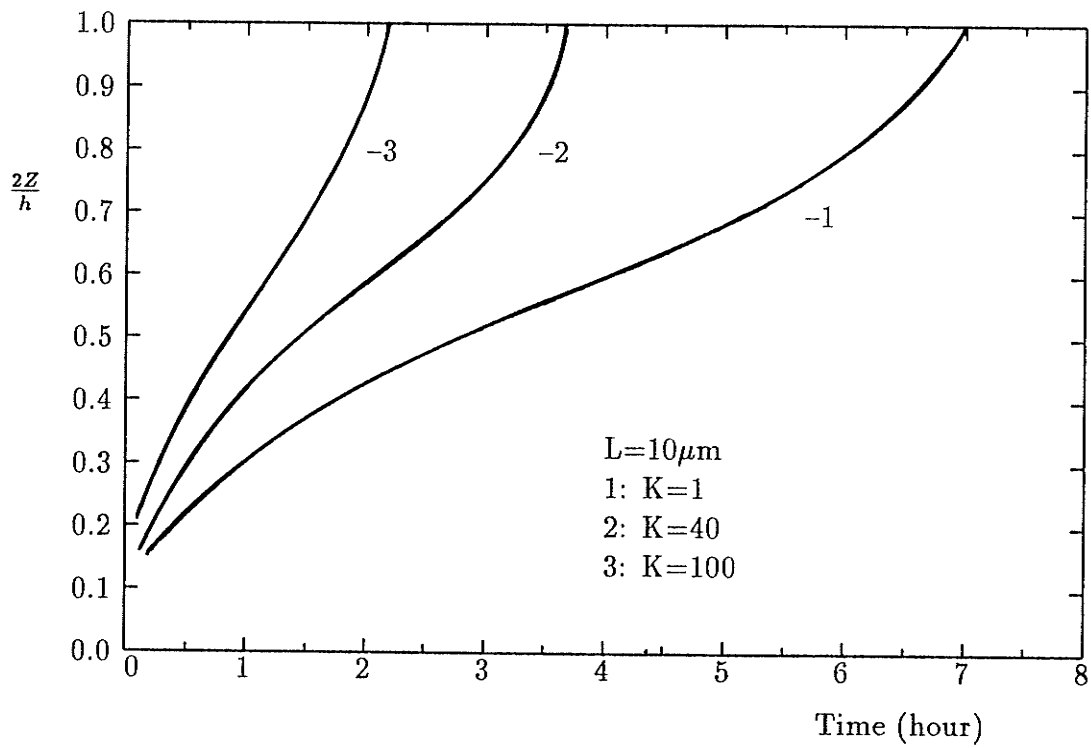


Figure 4.9: Calculated penetration curves. Grain size  $10 \mu\text{m}$ . Curve 1 represents the lattice diffusion. The contribution from the grain boundaries is 60% for curve 2 and >90% for curve 3.

# Chapter 5

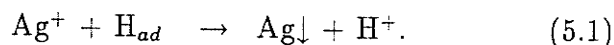
## Modification of the Silver Decoration Technique

### 5.1 Introduction

Great effort has been made in developing new techniques that will provide more direct and informative results and thus lead to a better understanding of the mechanism of hydrogen embrittlement.

In the early 1960's, Devanathan and Stachurski [16] developed the electrochemical double-cell permeation technique. This technique enabled researchers to investigate diffusion behavior of hydrogen, trapping phenomena, surface effect, and other effects in metals and alloys. It has also been modified to study dislocation transport of hydrogen during deformation [112,113]. A thermal analysis technique developed by Lee and his co-workers [114,115] is useful in the study of various traps for hydrogen in metallic materials. These two techniques, although useful, do not provide direct evidence of the distribution of hydrogen in the material. A few techniques exist that are capable of providing such evidence; e.g., tritium autoradiography reveals the distribution of trapped hydrogen in a surface layer. However, since long exposure periods are required [116], it cannot be used in a dynamic way. Recently, Schöber and Dieker [15] proposed a variation of the Ag-crystal decoration technique

which is based on the assumption that adsorbed atomic hydrogen is active and able to reduce silver ions in a specific solution into metal crystals through the decoration reaction



The Ag crystals then deposit on the spot where hydrogen atoms escape from the metal. The microstructural distribution of hydrogen fluxes can be revealed by observing the deposited crystals under an optical microscope or a scanning electron microscope (SEM). This technique has been used in various metals and alloys in this study in an attempt to identify the role of grain boundaries in mass transport of hydrogen. However, inconsistent results were obtained during tests. Poor reproducibility was also found by other research groups. Therefore, an investigation of the technique itself was performed which has led to a new interpretation of the decoration process. The decoration behavior of grain boundaries will be addressed in this chapter.

## 5.2 Experimental

Ni270 (99.98%) and Pd (99.9%) were used in the present investigation. As received Ni270 and Pd plates were cold rolled from 1.0 mm to 0.12 mm thickness. Ni specimens were annealed at 1323 K for 30 min. followed by water quenching whereas Pd specimens were annealed at 1273 K for 30 min. followed by air cooling. Pd specimens were mechanically polished to 0.05 $\mu\text{m}$  aluminum oxide powder since there is no convenient electropolishing method, and Ni270 specimens were initially mechanically polished to 6 $\mu\text{m}$  and then electropolished in 60%  $\text{H}_2\text{SO}_4$  at 5.5v for

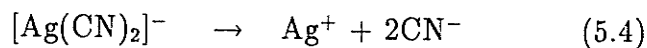
about 8 minutes.

The current density for cathodic hydrogen charging was 100 A/m<sup>2</sup> which was applied only on half of the specimen surface. Re-electropolishing was done at 5.5v for 1 min. on the whole surface in order to eliminate any contamination due to hydrogen charging. When necessary, outgassing was performed in vacuum at 0.00053 pa ( $4 \times 10^{-6}$  torr) for a given period of time at room temperature. During decoration, the whole specimen surface was immersed in the decoration solution. Therefore, two distinguished areas were obtained on the specimen surface; one had undergone hydrogen charging whereas the other was free from hydrogen. The hydrogen-free area was used as a reference.

Silver deposits were observed both under an optical microscope and the SEM (JXA-840). An X-ray diffractometer was used to determine the chemical composition and the structure of silver compounds that deposited on the specimen surfaces. Three stock solutions were used for the silver decoration tests and were prepared by adding (A) 20 ml, (B) 28 ml or (C) 40 ml of a 4% KCN aqueous solution to 10 ml of 12% AgNO<sub>3</sub> solution. According to Schöber and Dieker [15], the following reactions take place:



Simple calculation shows that 25 ml of 4% KCN solution will consume about 10 ml of 12% AgNO<sub>3</sub> solution without any residual precipitates of AgCN from reaction (5.2). Since the dissociation reaction



is the first step of the decoration process [15], an increase in the concentration of  $\text{CN}^-$  in the solution will shift reaction (5.4) to the left, and therefore, solutions A, B and C will all have different decoration capabilities. These stock solutions were used for decoration tests in dilutions of 1:50 as suggested by Schöber and Dieker [15].

## 5.3 Results and Discussion

### 5.3.1 In the Absence of Hydrogen

Results of the decoration tests on Ni and Pd specimens without hydrogen charging are summarized in Table 5.1. It can be seen that Ni is active either in solution A which can be considered as a saturated AgCN solution or in solution C which has surplus  $\text{CN}^-$  ions. Deposits on an electropolished and uncharged Ni270 specimen decorated in solution A for 12 hours are shown in Figure 5.1. Two kinds of deposits are evident, small white particles in the background and long needles randomly distributed in groups. Both these deposits were high in silver as determined by energy dispersive spectrum (EDS) analysis on the SEM. X-ray diffractometer analysis showed the presence of both pure silver and AgCN crystals. Therefore, the long needles are most likely AgCN crystals.

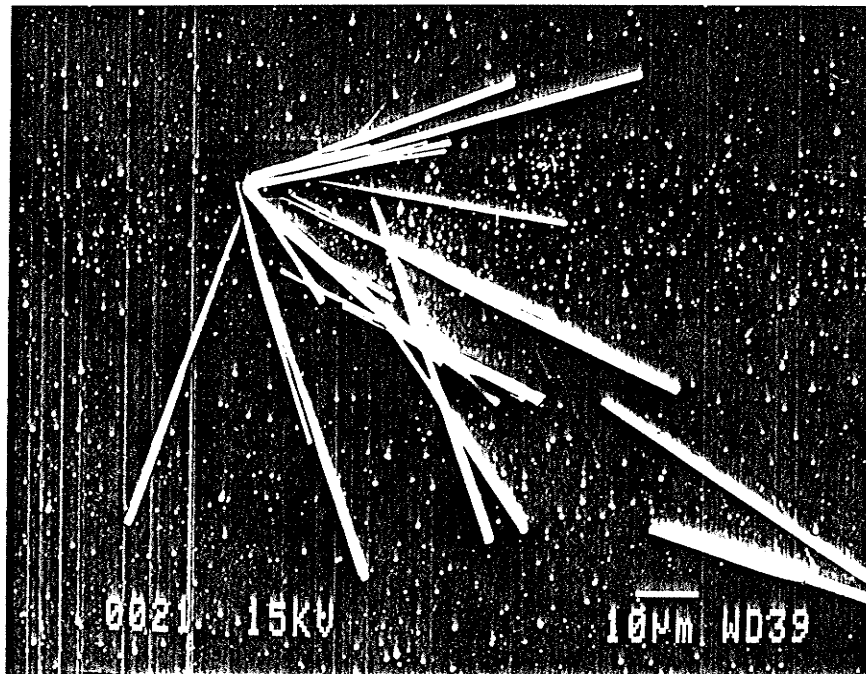
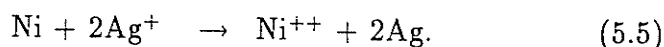


Figure 5.1: Deposits on Ni270 (electropolished and uncharged) decorated in solution A for 12 hours.

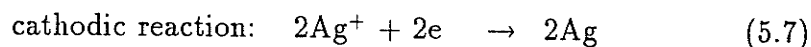
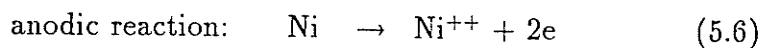
Table 5.1. Results of decoration tests without hydrogen charging

	solution A	solution B	solution C
Ni	white deposits formed in 10 min.	no deposits up to 24 hrs.	white deposits formed in 10 min.
Pd	white deposits formed in 10 min.	no deposits up to 24 hrs.	no deposits up to 24 hrs.

Deposits formed during decoration in solution C for 5 hours are shown in Figure 5.2. These deposits were identified as pure silver crystals by EDS and X-ray diffractometer. They are of the same size and equiaxial in shape. Since Ni is chemically more active than silver, the following direct displacement reaction might take place:



This reaction may play an important role in the early stages of growth of the particles which is supported by the fact that no deposits were observed on Pd decorated in this particular solution since Pd is chemically more stable than Ag. In the later stages the following reactions may also take place:



which will result in the deposition of silver particles of various shapes not related to the microstructural distribution of hydrogen flux.

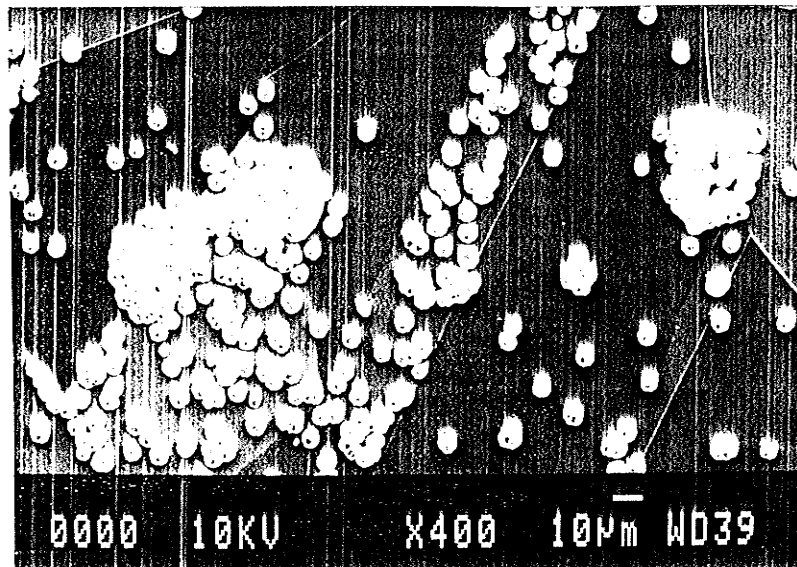
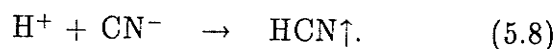


Figure 5.2: Silver particles on an electropolished and uncharged Ni270 specimen decorated in solution C for 5 hours.

Deposits on a mechanically polished and uncharged Pd surface decorated in solution A for 8 hours are shown in Figure 5.3. The dark area on the bottom left is the reference region which was above the liquid line during decoration. The white particles in Figure 5.3 were confirmed by EDS and X-ray diffractometer as silver crystals and AgCN compounds. These deposits formed a denser layer in a shorter time than that on Ni specimens in the same solution. Since Pd is more stable than silver, the displacement reaction cannot take place. In addition, this solution has the lowest concentration of  $\text{CN}^-$  ions; therefore, these deposits are attributed to the stronger catalytic nature of Pd and possibly to the effect of impurities in the Pd used in the present investigation. It was found that these deposits dissolved completely in solution C within a short time suggesting a high percentage of AgCN in the deposits since only AgCN can dissolve in solution C rapidly.

From the above results, it is evident that a change in chemical composition of the decoration solution can result in various decoration behaviors without hydrogen charging. Even inert Pd cannot always be inactive in the decoration solution. Therefore, in order to obtain a reference state where no silver deposits are observed, the chemical composition of the decoration solution has to be controlled. In fact, if the decoration reaction takes place in the presence of adsorbed hydrogen atoms, the resulted hydrogen ions will enter into the solution [reaction (5.1)], and the following reaction may take place:



This will change the concentration of  $\text{CN}^-$  ions in the solution. Consequently, it seems unavoidable that different reactions occur in the various stages of the decoration process. Ideally, in using the silver decoration technique, there should be a

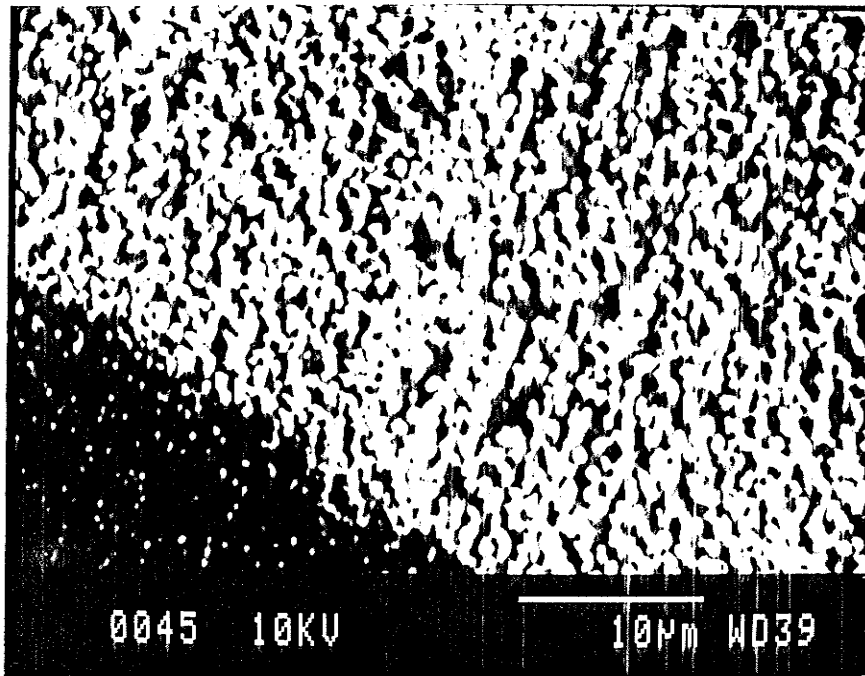


Figure 5.3: Deposits on uncharged Pd surface after decoration in solution A for 8 hours.

direct relationship between the escaping hydrogen atoms and the depositing silver atoms; i.e., a one-to-one correspondence. This would give quantitatively the number of hydrogen atoms escaping from the surface. However, various reactions, e.g. reactions (5.6) and (5.7), other than the decoration reaction [reaction (5.1)] may become involved during the later stages of deposit growth. Therefore, the number of deposited silver atoms would be greater than that due to escaped hydrogen alone. On the other hand, absorbed hydrogen atoms can also escape from the material through recombination to form molecules of  $H_2$  and this hydrogen will not cause silver deposits. It is concluded that the silver decoration technique cannot be used quantitatively.

### 5.3.2 In the Presence of Hydrogen

Since both Ni and Pd are inactive in solution B, the subsequent decoration tests with hydrogen charging were performed only with this solution. Details of such tests on Ni are summarized in Table 5.2. It was found that the reference area showed no deposits after decoration on all the samples indicating that the silver deposits truly resulted from hydrogen charging. However, it is well known that cathodic charging activates metal surfaces, so that the charging procedure has two effects. First, it re-activates the specimen surface by reducing the oxidation film which is formed during pre-electropolishing [117]. Secondly, it loads hydrogen into the specimen which will escape from the surface after switching off the charging current. The silver decoration technique can be used with confidence only when the surface effect can be deducted from the total decoration behavior. This aspect will be explored in the following procedure.

Table 5.2. Procedures of decoration tests in Ni charged with hydrogen

specimen	Hydrogen charging	Outgassing	Re-electro-polishing	Outgassing	Decoration	Results
No.1	30 min.	nil	1 min.	nil	9 hrs.	Fig.5.4
No.2	30 min.	nil	1 min.	70 hrs.	30 min.	Fig.5.5
No.3	30 min.	26 hrs.	1 min.	nil	30 min.	Fig.5.6

Immediately after re-electropolishing and rapid washing, specimen No.1 was immersed in the decoration solution and the resulting surface deposits are shown in Figure 5.4. Under these test conditions, 10 minutes of decoration was adequate and able to produce results similar to those reported by Schöber and Dieker [15]. To see the growth behavior of the deposited particles, the decoration period was extended to 9 hours for this specimen. It can be seen that both grain interiors and grain boundaries are decorated. The silver deposits particularly on the grain boundaries have been attributed to local hydrogen flux by Schöber and Dieker [15]. However, some large hexagonal crystals are evident in the grain interiors which are unlikely to be related to local distribution of hydrogen flux. Specimen No.2 (Table 5.2) was outgassed for 70 hours after re-electropolishing. The decoration behavior in this specimen (Figure 5.5) was similar to that of specimen No.1; i.e., the grain boundaries were decorated. As expected, the size of the silver deposits in this specimen was smaller because of the shorter decoration period (30 min.).

The average concentration,  $C_{av}$ , in a membrane of uniform initial concentration,

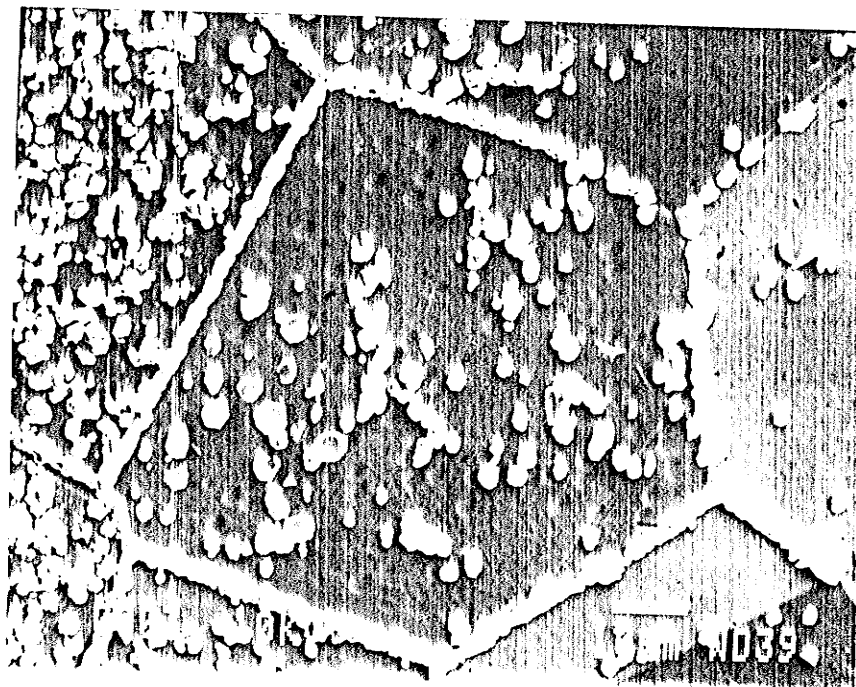


Figure 5.4: Decoration deposits on Ni270 surface after hydrogen charging and re-electropolishing in solution B for 9 hours.

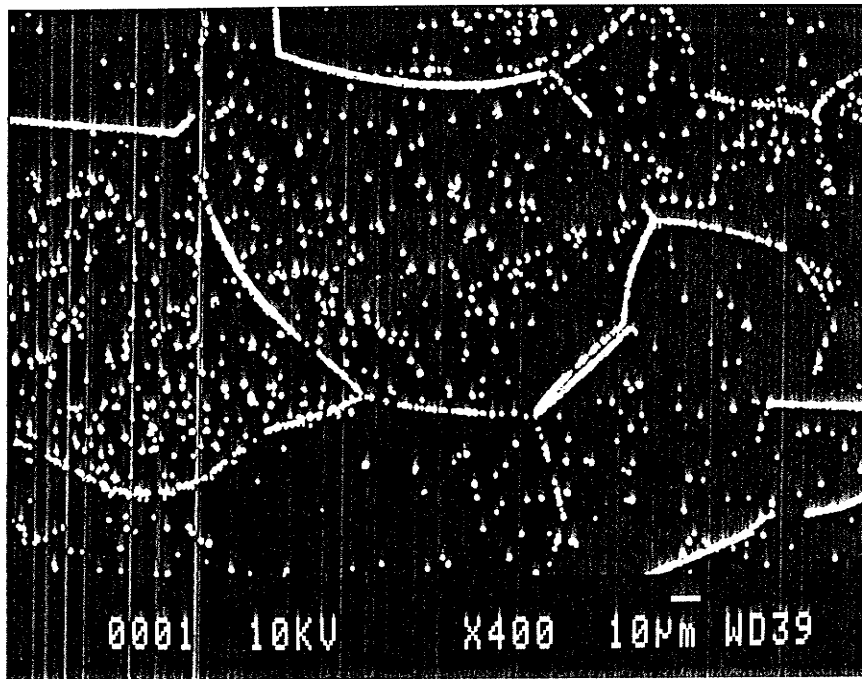


Figure 5.5: Silver particles in charged area on Ni270 decorated in solution B for 30 min. Grain boundaries are decorated.

$C_0$ , during degassing can be approximated as the following when  $C_{av}$  is much smaller than  $C_0$  [118]:

$$\frac{C_{av}}{C_0} = \frac{8}{\pi^2} \exp\left(-\frac{\pi^2 D_{eff} t}{h^2}\right) \quad (5.9)$$

where  $h$  is the thickness of the membrane and  $D_{eff}$  is the effective diffusivity. Substituting  $D_{eff} = 6.3 \times 10^{-14} \text{m}^2/\text{s}$  which is the lattice diffusivity of hydrogen in nickel [119] and  $h = 0.01 \text{cm}$  into the above equation, one finds that at  $t = 30 \text{h}$ ,  $C_{av}/C_0 \leq 0.001$ , i.e., degassing is essentially completed even if no effect of fast diffusion paths was considered. In the case of specimen No.2, the charging period was far from reaching the equilibrium state. Therefore, it should take less time for complete degassing than calculated from eqn.(5.9). In another experiment, specimen No.3 was outgassed for only 26 hours *before* re-electropolishing and decorated for the same time as specimen No.2. In this specimen grain boundaries were not decorated (Figure 5.6) and silver deposits were observed only on the grain interiors in the charged area. This implies that the degassing was indeed completed in 26 hours and the hydrogen flux at grain boundary areas had stopped prior to the decoration process in this specimen. This further shows that hydrogen fluxes from grain boundaries in specimen No.2 during the decoration period should not exist since the specimen was outgassed for a longer period (70 hours). Therefore, it can be concluded that outgassing completed *after* re-electropolishing has no significant effect on the subsequent decoration process.

From the above discussion, it is seen that while outgassing extinguishes the hydrogen flux at grain boundaries, it does not eliminate silver deposition. The only consistent explanation is that the silver deposits observed on the surface of specimen

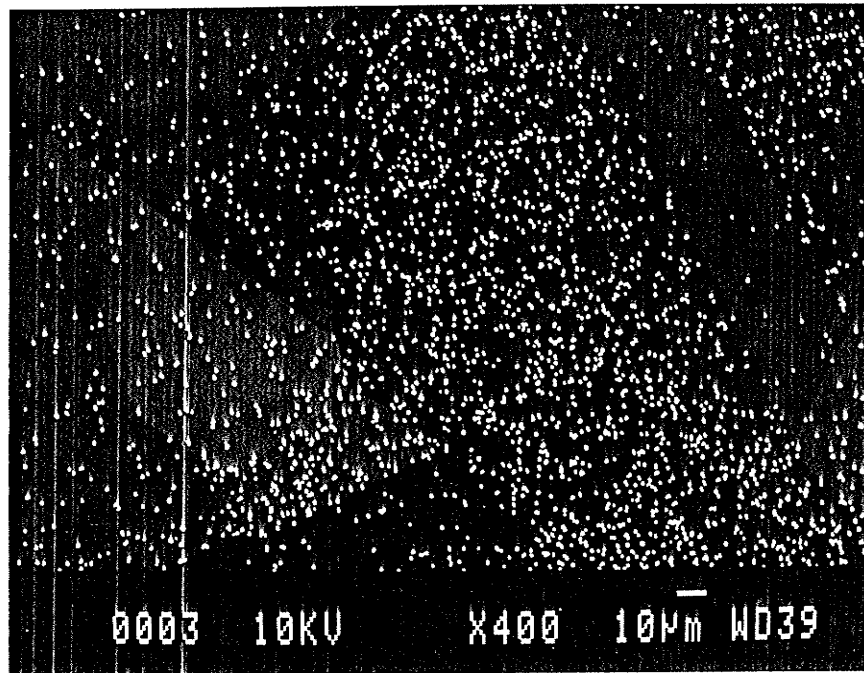


Figure 5.6: Silver particles in charged area on Ni270 degassed for 26 hours before re-electropolishing and decorated in solution B. Grain boundaries are not decorated.

No.2 were due to surface effects. As for the silver deposits observed on specimen No.1, although they are similar to those on specimen No.2, they can be due to surface effects as well as hydrogen fluxes via reaction (5.1). Therefore, it can be concluded that silver deposition due to hydrogen oxidation [reaction (5.1)] is not the only deposition process which can occur.

The above observations suggest that the stage at which the re-electropolishing is applied is of utmost importance. If it is applied immediately after charging as for specimens No.1 and 2, a hydrogen outgassing flux would still exist at grain boundary areas and therefore these areas could not be rendered inactive during re-electropolishing; i.e., no oxidation film could form on the grain boundary intersections with the free surface. Another, less likely, possibility is that during re-electropolishing, the hydrogen flux may result in the formation of compounds (e.g. hydrides) which retain hydrogen and consequently result in silver deposits through an unknown process. Nevertheless, it is still a surface effect. Therefore, even if there is an outgassing period between re-electropolishing and decoration, surface effects lead to deposition of silver crystals. Conversely, deposited silver crystals were not observed along grain boundaries when re-electropolishing was applied after outgassing (specimen No.3) because the grain boundaries were inactivated due to the lack of a hydrogen flux. It is concluded that this technique can reveal hydrogen flux at grain boundaries which occurred during re-electropolishing rather than during decoration.

It should be noted that since the charging period for specimen No.3 was only 30 minutes while the outgassing period was 26 hours, a detectable hydrogen flux in grain interiors would not be expected during either re-electropolishing or decoration. However, after decoration the grain interiors exhibited silver deposits while the grain

boundaries were free implying that grain boundaries are more liable to inactivation than the grain interiors. The length of re-electropolishing was 1 minute which was sufficient to make the grain boundary areas inactive but insufficient to deactivate the grain interiors. If re-electropolishing was prolonged to 5 min. or longer, no silver deposits were observed on either grain boundary areas or grain interiors after decoration.

From the above observations, it can be concluded that damage to the oxidation film on the metal surface will lead to silver deposition. This is consistent with Schöber and Dieker's [15] results that only electropolished surfaces did not have silver deposits when hydrogen was not present. Therefore, in order to separate the decoration response due to hydrogen flux from that due to surface effects during decoration an oxidation film has to be re-built. This is impossible if the decoration is performed on the charged surface since it has also been shown that an oxidation film cannot form at grain boundaries during re-electropolishing if hydrogen flux is still there. Therefore, the silver deposits observed at grain boundaries on specimen No.1 cannot be unambiguously attributed to local hydrogen fluxes as originally proposed [15]. In fact, there is no evidence thus far that the proposed decoration reaction [reaction (5.1)] takes place during decoration.

However, when thin Ni membranes were decorated in solution B partly on one side (i.e. downstream side) while being charged with hydrogen from the other side, it was found that silver deposits occurred on the downstream side predominantly in the region opposite the charging area after a certain period. Since this side has not undergone hydrogen charging, the oxidation film formed during pre-electropolishing should still be intact at least before hydrogen atoms reach it. Therefore, this surface could be used as a reference. The difference in the decoration response in the

region opposite the charging area and in the surrounding reference area must be due to hydrogen permeation. It was found that the time interval between starting the charging current and observing silver deposits increased with the thickness of the membrane, and that if the membrane was cold worked without annealing, the time interval became much longer which can be attributed to the trapping of hydrogen by deformation induced dislocations [120]. These observations can be considered as evidence that silver deposits on the downstream surface are indeed related to the hydrogen permeation process, possibly through the proposed decoration reaction (5.1). However, there is another possibility that hydrogen atoms may react with the oxidation film before they reduce silver ions in the solution therefore re-activating the surface in turn causing silver deposition.

The above observations do not clearly confirm the decoration reaction itself, but do provide a means of obtaining useful information regarding grain boundary transport of hydrogen. By decorating the downstream surface at various stages corresponding to a permeation test, dynamic information regarding hydrogen flux at grain boundaries can thus be obtained. If grain boundaries are fast diffusion paths for hydrogen, atomic hydrogen will emerge on the downstream surface in grain boundary areas first. A pattern of grain boundaries decorated by silver particles will be expected either through reaction (5.1) or through re-activation of the surface film. On the other hand, the escaping hydrogen flux at grain boundary areas on the charging surface can also be investigated by changing the interval between terminating the cathodic charging current and applying re-electropolishing. When there is no silver deposition on these areas, it may be concluded that the local hydrogen flux has stopped. The application of this technique to grain boundary transport of hydrogen in solution annealed Ni270 will be given in the following chapters.

Schöber and Dieker [15] observed silver deposits in straight lines in a slightly deformed hydrogen charged specimen. They correlated these deposits to dislocations at slip lines and drew the conclusion that dislocations provide short circuit paths for hydrogen diffusion. In the present study it was found that cold work increased the interval before silver deposits were observed, which is an indication that dislocations are not fast diffusion paths. Further, it was found that slip lines in slightly deformed and hydrogen charged specimens were essentially deposit-free on the downstream side, and that in hydrogen-free specimens silver crystals preferentially deposited in regions of higher dislocation density. In this case the deposition process was caused by an imperfect surface film. Therefore, even if dislocations do provide short circuit paths for hydrogen diffusion, the silver decoration technique is not capable of unambiguously showing this.

## 5.4 Conclusions

1. There is no one-to-one correspondence between the deposited silver atoms and escaping hydrogen atoms, i.e., the silver decoration technique does not provide quantitative information.
2. The silver decoration technique can reveal escaping hydrogen flux from the grain boundary intersections with the free surface on the charging side during re-electropolishing rather than during the decoration process.
3. Different reactions occur in the various stages of the decoration process. To obtain reliable results a perfect oxidation film must be maintained on the metal surface.
4. This technique can be used to obtain dynamic information regarding mass

transport of hydrogen in a metal membrane. Useful information about the role of grain boundaries can be obtained.

# Chapter 6

## Experimental Procedures

### 6.1 Materials

Polycrystalline high purity nickel was used in the present study. Nickel was chosen for two reasons. First, much work has been done on this metal, so it was not difficult to find data for comparison. Since Auger Electron Spectroscopy was not available in our laboratory, chemical analysis of grain boundary planes was not possible. However, many reports in the literature provide such data, and therefore the present study could proceed with reasonable confidence. Second, hydrogen changes the fracture mode in this metal from ductile rupture to brittle intergranular cracking, which makes the metal an ideal candidate for the purpose of this study.

High purity Ni270 (99.98% Ni) was used throughout the course of this study. A lower purity metal (99.9% Ni) was also used to study the effect of sulfur segregation. It was made by induction melting 99.9% nickel in vacuum at this laboratory.

### 6.2 Specimen Preparation

#### 6.2.1 Specimens for Permeation and Decoration Tests

Two grain sizes were used:  $10\mu\text{m}$  and  $150\mu\text{m}$ , which will be designated as fine and coarse grain size, respectively. The fine grain size was achieved by cold

rolling as-received nickel rod of 16mm diameter to about 0.15 mm thickness and annealing at 588K for 60 minutes. To obtain coarse grains, annealed nickel plates of 2 mm thickness were cold rolled to 0.15mm, annealed at 1323K under an argon atmosphere for 30 minutes then quenched in water. Observation of the microstructure under an optical microscope and micro-hardness measurements confirmed that full recrystallization was achieved, and grain sizes were reasonably uniform in all specimens.

All specimens were electrolytically polished on both sides in a 60% H<sub>2</sub>SO<sub>4</sub> solution at 5.5V to a nominal final thickness of 0.1mm unless otherwise stated. For membranes with coarse grains, many grain boundary segments could penetrate through the whole thickness of the membrane, which is desirable for silver decoration tests.

### 6.2.2 Specimens for Penetration Tests

Thin membrane and cylindrical specimens were used. The membrane tensile specimens had a cross section of  $4.5 \times 0.2 \text{ mm}^2$  and a gauge length of 12 mm. The rod specimens had a gauge length of 12 mm with a diameter of 2.0 mm. A fine grain size of  $10\mu\text{m}$  and a medium grain size of  $50\mu\text{m}$  were used for the membrane tensile specimens. For all specimens used, the grain size was reasonably uniform. Fine grain size was obtained by cold rolled as received nickel rod ( $\phi 16\text{mm}$ ) to 0.25 mm thickness and annealed at 588K for 60 minutes. The medium grain size was obtained by same procedure but annealed at 1173K for 5 minutes. Full recrystallization was confirmed by optical microscope observation and micro-hardness measurements. Cylindrical specimens were made from a slightly lower purity metal. Laboratory melt ingot was cold swaged to about 70% reduction in diameter, and after manufacturing, the specimens were annealed at 1173K for 10min. to get  $50\mu\text{m}$  grain size or 1323K for

1 hour to get  $150\mu\text{m}$  grain size. Sulfur segregation was introduced by aging at 873K which did not result in further change in the grain sizes. No effort was made to analyze quantitatively the sulfur concentration in grain boundaries. The degree of segregation was controlled by changing the length of aging period. All specimens were electrolytically polished in a 60%  $\text{H}_2\text{SO}_4$  solution at 5.5V.

### 6.3 Apparatus and Procedures for Electrochemical Permeation Tests

The apparatus for the permeation tests is shown in Fig. 6.1. Computer calculated results have shown that if grain boundaries are indeed fast diffusion paths for hydrogen their contribution to the total permeating current is more dominant at small times, i.e. around the actual breakthrough time,  $t_{ag}$  (see Fig.4.7). Therefore, more attention should be given to the early stages of a permeation test. Accordingly, neither side of the testing membrane was plated with Pd in order to achieve low background anodic current densities which were usually about  $1\text{ nA/cm}^2$  after anodic polarization for 24 hours at 0.0 or 0.1 V saturated calomel electrode (SCE) in 0.1N NaOH solution. Hydrogen charging was performed in 1N  $\text{H}_2\text{SO}_4$  solution with 250mg  $\text{As}_2\text{O}_3$ /l added. The chemical  $\text{As}_2\text{O}_3$  was first dissolved in distilled water by adding dilute NaOH solution. Electrolyte was pre-electrolyzed for at least 50 hours to reduce impurity deposition onto the membrane surface. A charging current density of  $1\text{mA/cm}^2$  was used. A rather large area,  $1.4\text{cm}^2$ , was exposed to the electrolytes to reduce the Joule heating effect [121]. The anodic current was measured with a digital multi-meter and recorded on a chart recorder. The sensitivity of the complete setup was such that an increase as small as 0.2 nA from the background anodic current could be detected; i.e. the sensitivity was 0.01% for detecting the

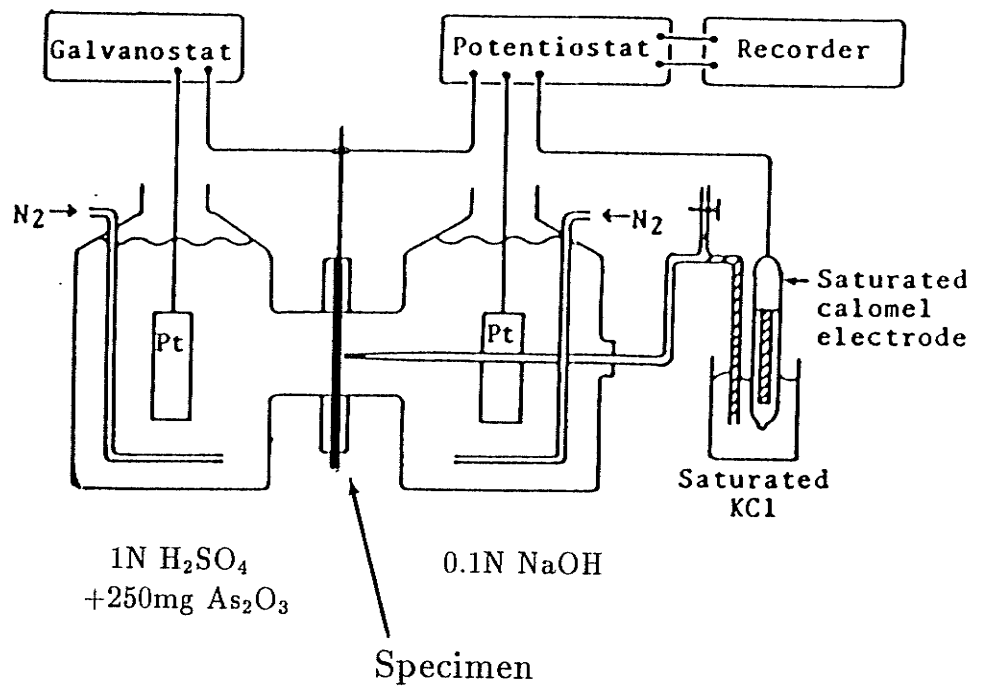


Figure 6.1: Apparatus for permeation tests.

break-through time since the steady state current was in the range of  $1 \sim 3 \mu\text{A}$ . This degree of sensitivity is essential in trying to clarify the very beginning stage of a permeation curve, since the actual breakthrough time depends on the sensitivity of the monitoring system as already shown in Chapter 4. For recording completed permeation curves, the sensitivity was set at 0.1-1.0%.

During the tests, anodic polarization was performed until the anodic current decayed to a stable background level. At this stage, even with the highest detecting sensitivity, the slope of the recorded curve was negligible. Then, within a minute, the catholyte was poured into the cathodic compartment and galvanostatic cathodic polarization was started. The anodic potential was maintained by a potentiostat at 0.0 V SCE. All tests were performed at room temperature.

## 6.4 Apparatus and Procedures for Silver Decoration Tests

The cell set up for the silver decoration tests is shown in Figure 6.2 which is similar to that for the permeation tests. Since no electrode is needed in the decoration process, the anodic compartment of the permeation cell is replaced by a decoration compartment which has two identical holes where the membrane contacts the decoration solution. The bottom one, which is opposite the charging area, forms the working area on the testing membrane while the upper one forms the reference area. The two compartments are put together by a pair of clips with the testing membrane in between. To avoid leakage, soft silicon rubber sheets with matching holes are used in between each side of the membrane and the corresponding compartment.

Care must be taken to avoid any deformation which could result in silver depo-

sition in the absence of hydrogen. Confidence with results can be obtained 1) if no silver deposits are observed when the decoration compartment has been filled with decoration solution for a long period as long as hydrogen is not charged into the membrane from the other side, and 2) if the incubation time for silver deposition increases with the thickness of the membrane.

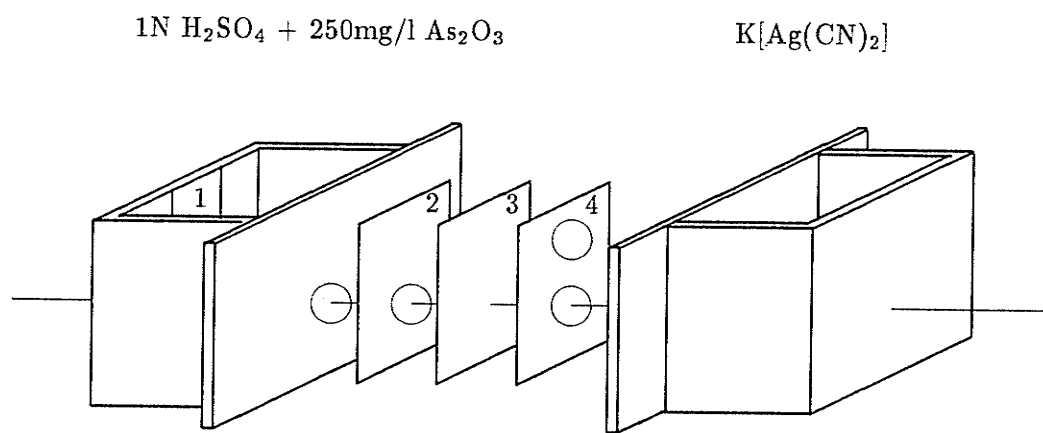
After obtaining the complete permeation curve, duplicate specimens were charged on the decoration cell, with the decoration compartment empty, for a given period corresponding to a pre-selected stage on the permeation curve. Then a dilute  $K[Ag(CN)_2]$  solution (Solution B described in Chapter 5) was added into the decoration compartment. After a given period of decoration, usually less than 10 minutes, the membrane was removed from the cell, washed and dried. The surface was then observed with an optical microscope and a scanning electron microscope (SEM). All tests were performed at room temperature.

## 6.5 Apparatus and Procedures for Penetration Tests

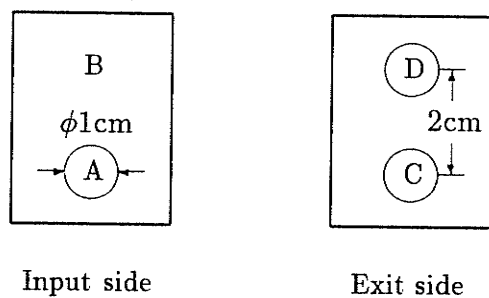
Specimens were cathodically precharged with hydrogen at room temperature for a given period in the catholyte. The charging current density was  $10 \text{ mA/cm}^2$  for most specimens unless otherwise stated. Tensile testing was carried out on an Instron screw-driven tensile test rig. A calibrated load cell (500 Kg) and constant crosshead speeds were used for all tensile tests. Due to the complexity of the test procedures, the measured tensile strengths had a scatter of 5%. No strain rate effect was found in the early tests in the range of  $10^{-2} \text{ s}^{-1}$  to  $10^{-4} \text{ s}^{-1}$ ; therefore, the strain rates in subsequent tests were adjusted so that each test would finish in about 10 minutes. Fracture surfaces were observed by scanning electron microscopy using a

JXA-840 electron microscope. The depth of intergranular cracking was obtained by averaging at least five measurements on each specimen.

For low temperature tests the specimens were mounted in the tensile testing apparatus and quenched into liquid nitrogen. Less than 3 minutes elapsed between precharging and cooling to 77K. Tensile loading was not applied until 10 more minutes had elapsed to reach thermal equilibrium. Since at 77K, hydrogen is essentially immobile, the procedure provided a means to study the effect of local hydrogen which had been preseggregated at a higher temperature.



(a)



(b)

Figure 6.2: (a). Silver decoration cell: 1. Pt electrode, 2. front rubber seal; 3. test membrane; 4. downstream rubber seal and (b). membrane with various areas described in the text.

# Chapter 7

## Experimental Results

### 7.1 Electrochemical Permeation Tests

#### 7.1.1 General Permeation Results

Figure 7.1 shows the typical experimental permeation currents with the reduced time for both coarse and fine grain sizes. For convenience of comparison, some theoretical predictions are also shown. Curve 1 is a theoretical calculation for the case  $K = 1$ , i.e. lattice diffusion alone (using  $6.3 \times 10^{-10} \text{ cm}^2\text{s}^{-1}$  for  $D_l$ ). If fast transport by grain boundaries occurs, the recorded permeation curves should fall in the area to the left of this curve. For instance, Curve 2 was obtained from eqn.(3.10) for  $K = 40$  and  $s = 114$  with a grain size of  $10\mu\text{m}$ . In this case the lattice contribution is still slightly over 50% of the total permeating flux, i.e. grain boundaries starting to be dominant, but the calculated curve is already quite far to the left of curve 1. Contrary to this, all recorded curves of the permeation tests fall to the right of the curve 1. Some curves are quite far away from curve 1 indicating possible surface contamination in those particular tests. Nevertheless, many curves are quite close to curve 1 when the value  $D_l = 6.3 \times 10^{-10} \text{ cm}^2\text{s}^{-1}$  was used to reduce the time. A typical curve is shown as Curve 3.

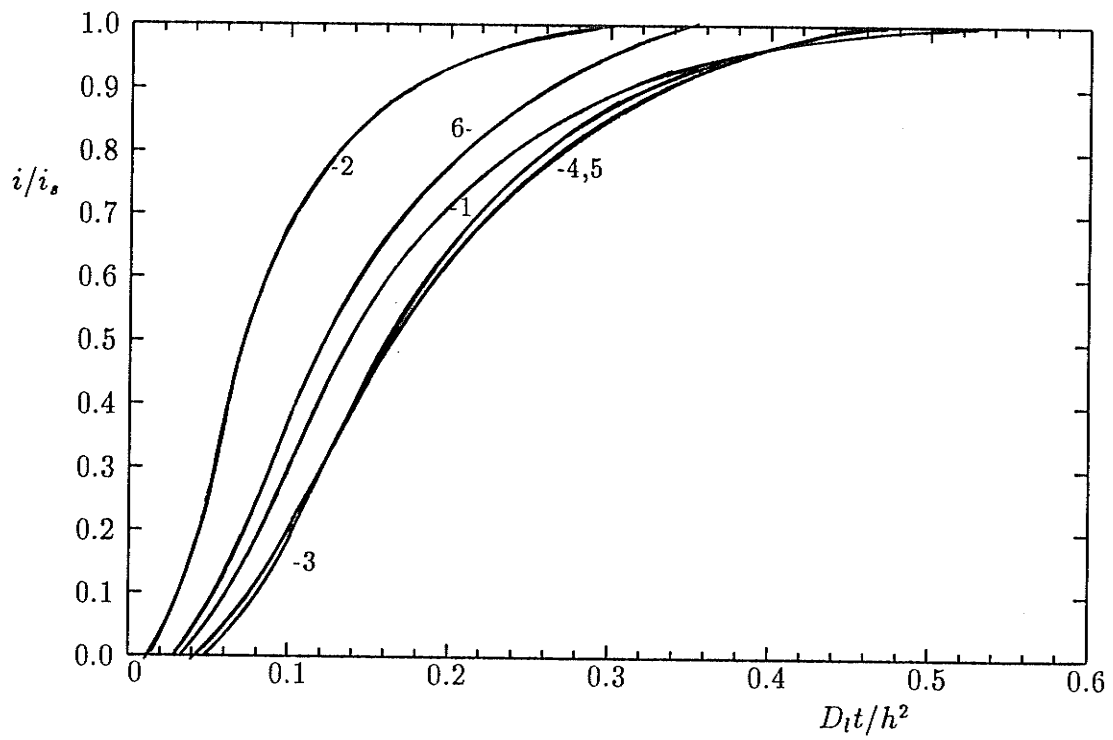


Figure 7.1: Measured permeation curves normalized by steady state value of permeation current of each individual test: 3)  $h = 0.01\text{cm}$ , 4)  $h = 0.007\text{cm}$  5)  $h = 0.01\text{cm}$  with coarse grains and 6) recharging of specimen from curve 3.

#### 7.1.1.1 Thickness Effect

A method to check if the recorded curves are related to the process of diffusion through the bulk thickness is to see if identical curves can be obtained in membranes with different thickness. This is especially important in this study since neither side was Pd plated. Curve 4 in Fig.7.1 was typically obtained on thinner membranes (70  $\mu\text{m}$ ) and is very close to Curve 3, indicating that the controlling process was indeed the diffusion of hydrogen through metal membranes and not disturbed by surface effects.

#### 7.1.1.2 Grain Size Effect

Curve 5 in Fig.7.1 was obtained from coarse grained membranes and is also close to Curve 3. In fact, curves 3, 4 and 5 are so close that it is hard to distinguish them in Fig.7.1. Therefore, the lack of a grain size effect can be concluded. This implies that lattice diffusion is the dominant process of hydrogen transport.

### 7.1.2 Effective Diffusivity

The anodic current started increasing at  $t = 90 \sim 100$  min. and continued to increase until a steady state value,  $i_s$ , was achieved at  $t \approx 18$  hrs. The lag time,  $t_{lag}$ , was about 8.5 hrs., obtained at  $i = 0.616i_s$ . Therefore, the effective diffusion coefficient was found to be  $5.4 \times 10^{-10} \text{ cm}^2\text{s}^{-1}$  from the equation [16]

$$D_{eff} = \frac{h^2}{6 \times t_{lag}} \quad (7.1)$$

This value agrees well with reported data in the literature, e.g.,  $4.5 \times 10^{-10} \text{ cm}^2\text{s}^{-1}$  by Robertson[84] and  $6.3 \times 10^{-10} \text{ cm}^2\text{s}^{-1}$  by Louthan et al [119]. It is noted that the hydrogen diffusivity in single crystal nickel at room temperature has been reported

to be  $4.3 \times 10^{-10} \text{ cm}^2\text{s}^{-1}$  [122]. Therefore, the measured diffusivity for hydrogen in nickel does not depend on grain size down to  $10 \mu\text{m}$ .

### 7.1.3 Trapping Effect

During the test, after curve 3 was completed the charging current was terminated while the recording of anodic current was continued. This procedure reveals the evolution behavior of hydrogen that remains in the membrane. However, since at this stage the recording digital meter was set on the high range, it was not possible to detect small changes in the permeation current; i.e., the detecting sensitivity was low. When the evolution transient decreased to a rather stable level which was a little higher than the original background level, i.e. before hydrogen was completely drained off, the membrane was given a recharging identical to the previous one. This time a small shift to the left was observed in the recorded curves only in the fine grained membranes. One curve ( curve 6 in Fig.7.1) shifted to the left of the theoretically predicted curve for lattice diffusion, curve 1. These observations suggest that some weak trapping effect due to grain boundaries does exist. If grain boundaries are fast diffusion paths, hydrogen in grain boundaries would have been drained off first, and therefore, one would not have seen the shift in the second run.

### 7.1.4 Early Stage Plateaus

An early plateau in the anodic current was reported by Tsuru and Latanision [14] to be caused by grain boundary transport. Two types of early rises were observed in the early runs of tests in the present study and were of same order as reported by Tsuru and Latanision, i.e. about 0.1 percent of the steady state permeation current. One was simultaneous with switching on the charging current and saturated within seconds, while the other had a short incubation time and saturated

in about three minutes. However, both types of early rises were found to be due to experimental procedures. The former was mainly related to interference of electronic circuits, which was not a surprise at such high sensitivities, and sometimes to poor sealing between the two compartments. The latter was caused by a difference in the temperature of the cathodic electrolyte from that of the anodic electrolyte. During the test, the cathodic electrolyte was added after anodic polarization had continued for at least 24 hours. Therefore, its temperature might be different than the anodic electrolyte. It is known that all electrochemical reactions are sensitive to the temperature. In our case, it was found that a small difference, 0.5K, would cause a detectable plateau. The behavior of this plateau depended on the temperature at which the cathodic electrolyte had been held. If the temperature of the cathodic electrolyte was lower than the testing membrane, a negative plateau could even be observed. After taking extreme care in every step, both types of early plateau were eliminated in the later tests.

It should be noted that the grain size used in this study ( $10\mu\text{m}$ ) was much smaller than that used by Tsuru and Latanision ( $\geq 100\mu\text{m}$ ). If the first plateau were due to grain boundary transport as suggested by Tsuru and Latanision, its magnitude (inversely proportional to the grain size) in the present study would have been about 10 times larger which should be easily detected. Therefore, it can be concluded that the early plateau is due to experimental conditions.

Fig.7.2 shows the early stages of several permeation tests. The recording system could detect an increase of 0.2 nA in anodic current and the steady state current was 1-3  $\mu\text{A}$ . Thus, the sensitivity of the system was about 0.01%, sufficient to detect any contribution of grain boundaries. It has been shown in Chapter 4 that if grain boundaries play an important role in the mass transport of hydrogen, the actual

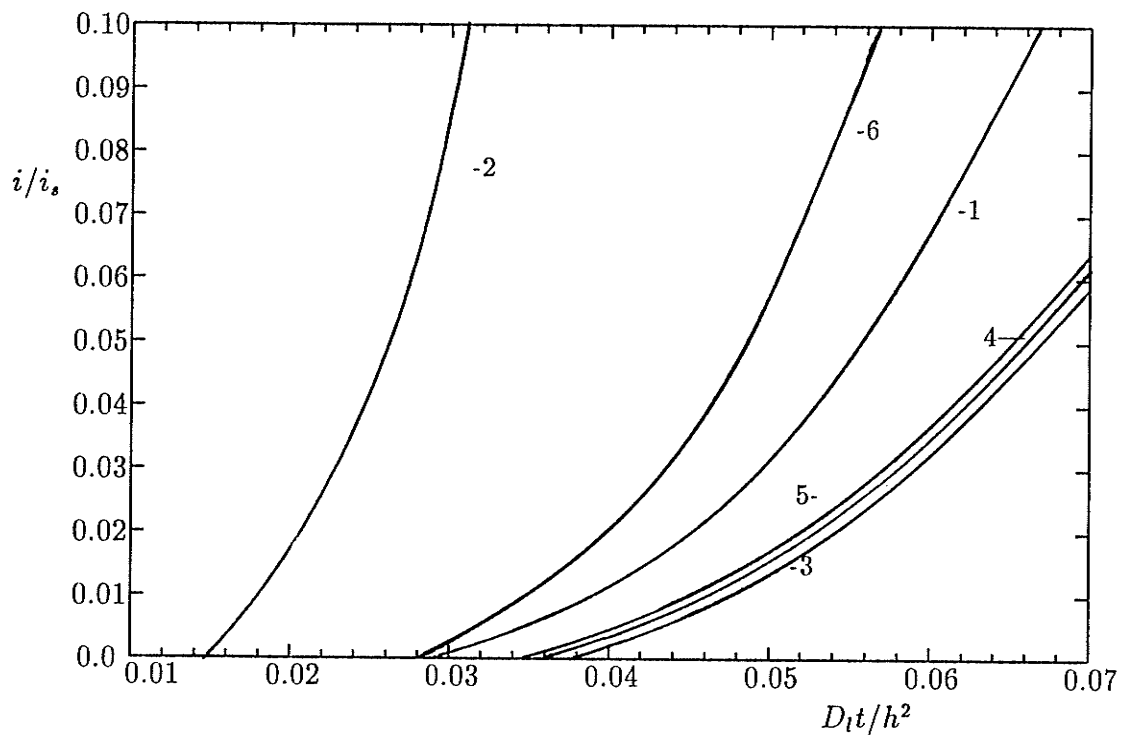


Figure 7.2: Early stages of permeation transients shown in Fig.7.1.

breakthrough time would be greatly reduced. It can be seen from Fig. 7.2 that all recorded curves do not increase until the breakthrough time corresponding to lattice diffusion (Curve 1) has passed. Therefore, based on observing the early stages of permeation curves, it can be concluded that the dominant process during the mass transport of hydrogen must be lattice diffusion.

### 7.1.5 The Steady State Permeation Rate

When  $K$  is greater than 100, grain boundary transport becomes dominant for the fine grain size. According to eqn.(4.1), at the steady state, the ratio of the grain boundary contribution to that of the lattice is  $4asK/L$ . Assuming the half grain boundary width to be  $5 \times 10^{-10}$ m and taking  $s = 100$  and  $L = 10^{-5}$ m, one expects to see a higher value of  $i_s$ , at least 3 times higher, for fine grained membranes than for coarse grained ones. However, the values of  $i_s$  were found to be scattered in a range from 1.5 to 3.0  $\mu$ A changing from membrane to membrane. There was no evidence that  $i_s$  for fine grained membranes was higher than that for coarse grained ones. That is,

$$\frac{4asK}{L} \ll 1 \quad (7.2)$$

which is equivalent to

$$K \ll \frac{L}{4as} = \frac{10^{-5}}{4 \times 5 \times 10^{-10} \times 100} = 50. \quad (7.3)$$

Therefore, it can be concluded that the measurement of the steady state permeation rates does not support the fast transport of hydrogen by grain boundaries.

To summarize, the permeation test results have clearly demonstrated that grain boundaries play no important role during the transport of hydrogen; i.e.,  $K \sim 1$ . However, the exact value of  $K$  cannot be evaluated from these results. This has to be resolved by silver decoration tests in the next section.

## 7.2 Silver Decoration Tests

### 7.2.1 Decoration Before Main Breakthrough

Since the membranes used for silver decoration tests were identical to those for permeation tests, the process of hydrogen transport in the membrane being decorated can be estimated from the measured permeation curves. Decoration was performed on the downstream surface of the membranes that had been charged with hydrogen for various periods. If the first plateau in some early runs of permeation tests was really due to an exiting hydrogen flux, one would expect to see decorated grain boundary patterns on the downstream surface when decoration was performed at any point before the main permeation curve started to increase; i.e. before  $t_a$ . However, it was found by carrying out several dozens of tests that silver deposits were observed only when the charging period had passed  $t_a$ . This further confirms that the first plateau was not related to permeating hydrogen.

### 7.2.2 Decoration Behavior of Grain Boundaries

Silver deposits were noted to appear in the reference area with much lower densities than that in the working area. This is most possibly due to later reactions in the decoration process (see Chapter 5). However, a consistent occurrence was that the grain boundaries were always free from silver deposits even when charging was prolonged to the steady state region of the permeation curve. At this stage the concentration gradient in the grain boundary,  $sC_0/h$ , should be much greater than that in the lattice,  $C_0/h$ , since the segregation factor is usually a large number. Thus, the absence of silver deposits on the grain boundary areas suggests either a small grain boundary diffusion coefficient (much smaller than that for lattice diffusion) or a severe barrier which prohibits the exit of hydrogen atoms.

In order to further clarify the situation, several membranes were tested in the following way: the membrane was tested in the permeation apparatus until the steady state was achieved, then the charging current was switched off, the membrane removed from the apparatus immediately, electrolytically polished to remove a surface layer about  $5 \mu\text{m}$  from both sides, and immersed in the decoration solution for 6 minutes. This resulted in four distinct areas on the membrane surfaces:

- A: charging area on the input side;
- B: protected area on both sides;
- C: working area on the downstream side;
- D: reference area on the downstream side.

After decoration, it was found that the distribution of silver particles on area D was basically identical to that on area B, having essentially no silver deposits or much fewer than areas A and C. This assured the effectiveness of the test. A major feature on area C was that no grain boundaries were observed to be decorated with silver deposits as shown in Fig.7.3. However, many grain boundary segments in area A were decorated with silver deposits as shown in Fig.7.4. These observations excluded the existence of a barrier on the grain boundary area prohibiting the exit of hydrogen atoms. The decorated grain boundaries in the charging area indicates that an exit hydrogen flux occurred at least during electropolishing. Therefore, the lack of decorated grain boundaries in the downstream surface implies the following:

$$D_g \frac{sC_0}{h} \ll D_l \frac{C_0}{h} \quad (7.4)$$

or

$$K = \frac{D_g}{D_l} \ll \frac{1}{s}. \quad (7.5)$$

Since  $s$  is large, we have

$$K \ll 1. \quad (7.6)$$

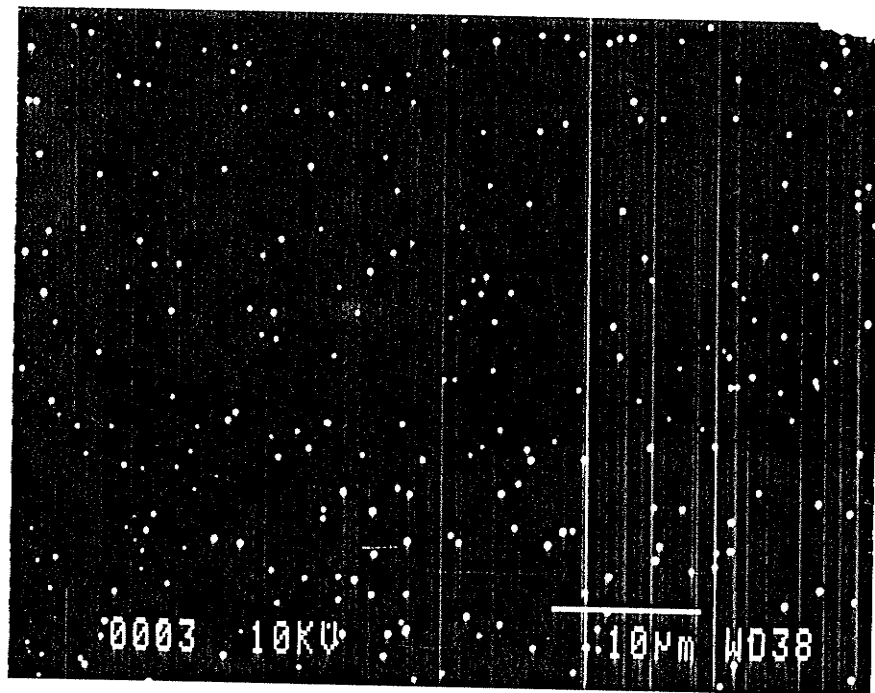


Figure 7.3: Non-decorated grain boundaries on area C of the downstream surface of Ni membrane. SEM 2000x.

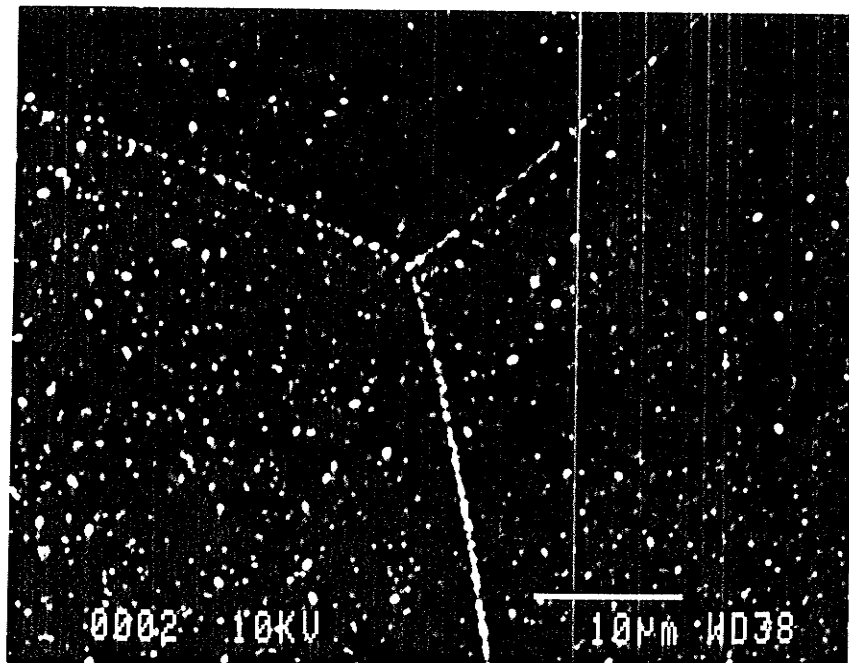


Figure 7.4: Silver particle decorated grain boundaries on area A of the charging surface of Ni membrane. SEM 2000x.

That is, the absence of decorated grain boundaries on the downstream surface was caused by a small grain boundary diffusion coefficient compared with  $D_l$ . On the other hand, however, the presence of decorated grain boundaries on the charging area implies that  $D_g$  is comparable to  $D_l$  on that side. Thus, it is concluded that the value of  $D_g$  is concentration dependent.

### 7.2.3 Effect of Segregated Sulfur

Similar procedures were applied to aged membranes in which grain boundaries were segregated with sulfur. Basically, similar results were obtained except for an interesting finding that when the downstream side was decorated after steady state had been established, some grain boundaries were decorated by silver particles, Fig.7.5. These tiny particles were not symmetrical about the grain boundary plane, being sometimes entirely within one grain. This is considered as evidence that sulfur increases local hydrogen activity around the grain boundaries.

## 7.3 Sulfur Induced Grain Boundary Cracking

### 7.3.1 In the Absence of Hydrogen

In the specimens with medium grain size and free from hydrogen, the measured ultimate strengths at 77K and room temperature without sulfur segregation were consistent with the data listed in the Metal Handbook [123] for both materials. The lower purity material has a little higher strength, ~5%, which is in the same order of the experimental scatter range. Therefore, the ultimate strengths are averaged as Curve b in Fig.7.6.

According to the equicohesive temperature theory, at temperatures lower than the equicohesive temperature, the grain boundary strength is higher than grain

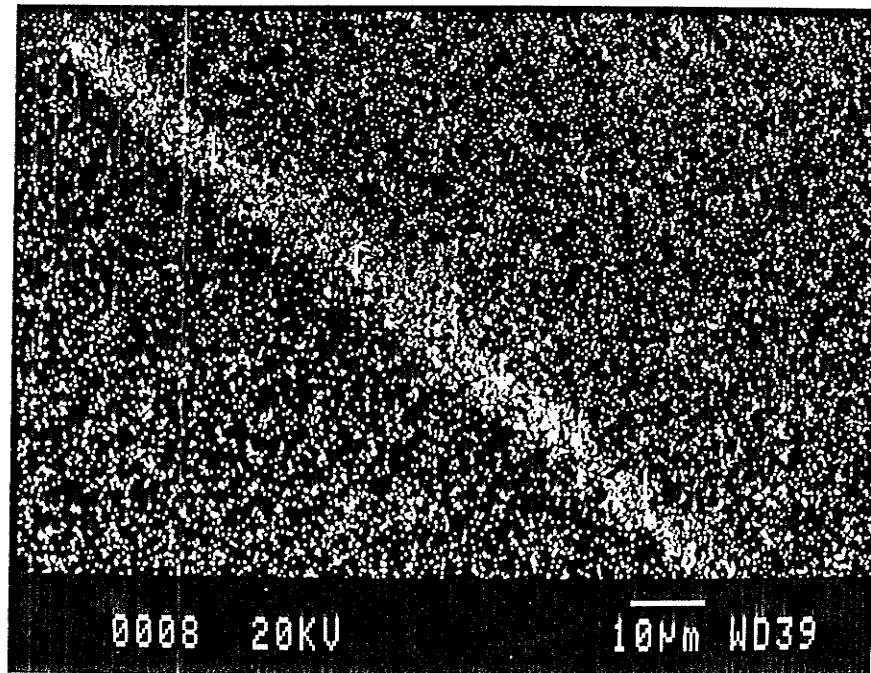


Figure 7.5: Silver particle in the vicinity of a grain boundary on downstream surface of Ni membrane with segregated sulfur. SEM 1000x.

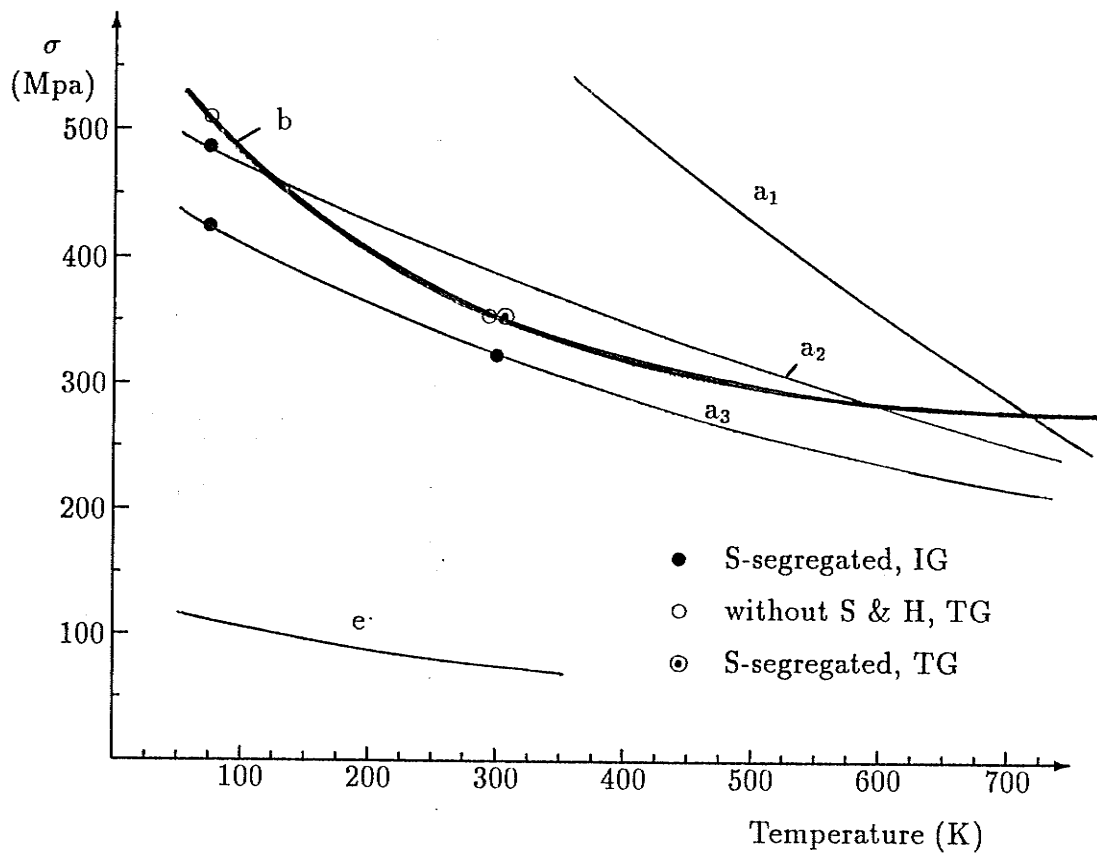


Figure 7.6: The ultimate strength and elastic limit vs temperature for grain size  $50 \mu\text{m}$ . Curves  $a_1$ ,  $a_2$  and  $a_3$  represent grain boundary strengths affected by segregated sulfur. Curve  $e$  is the elastic limit.

interiors and intergranular fracture will be observed only in the region above this temperature. This is shown by curves  $a_1$  and b in Fig.7.6 where data for Ni201 (99.5% Ni) has been used at temperatures above the room temperature since no data for Ni270 is available. Therefore, Curve  $a_1$  represents grain boundary strengths in the material.

When sulfur was introduced by annealing at 873K for 20 minutes, intergranular cracking was observed at 77K (with large plasticity) but not at room temperature. The grain boundary strength was lowered to the position of Curve  $a_2$  which is above the grain interior strength (Curve b) around room temperature. Fig.7.7 shows the intergranular fracture surface obtained at 77K. A large amount of plasticity is quite apparent. Note the existence of many small grains on the fracture surface.

When sulfur segregation was further increased by extending annealing to 24 hours, the ultimate strength was lowered further and intergranular cracking observed at both temperatures. The grain boundary strength became Curve  $a_3$  which is now entirely under Curve b. The fracture surfaces sometimes had microvoids as shown in Fig.7.8. Sulfur segregation was confirmed by EDS analysis on the scanning electron microscope (Fig.7.9); therefore, these microvoids are believed to be caused by sulfide formation. Unmatching striations with wider spacing and matching fine structures can both be seen (Fig.7.10). The latter suggests that a certain degree of plasticity which was continuous across the grain boundary had occurred before fracture. These observations indicate that the grain boundary fracture process competes with the grain strength and when the applied stress reaches the grain boundary strength which has been reduced by sulfur, intergranular cracking occurs. This agrees well with the decohesion theory of impurity segregation induced intergranular cracking.



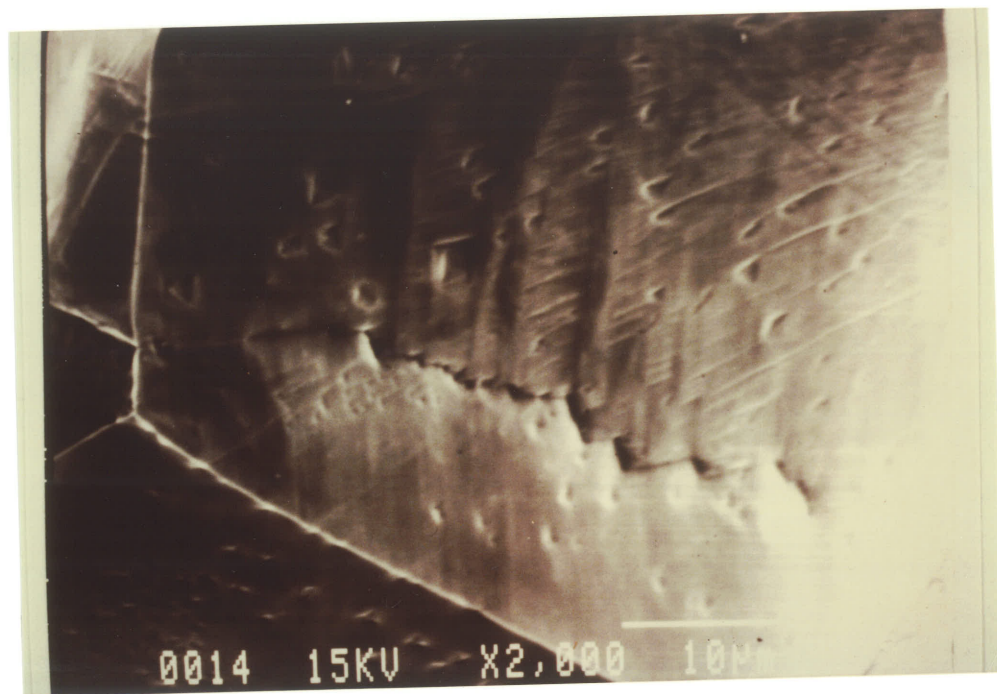


Figure 7.8: SEM fractograph of microvoids on fracture surfaces of a specimen which was fractured intergranularly at 77K with segregated sulfur at grain boundaries.



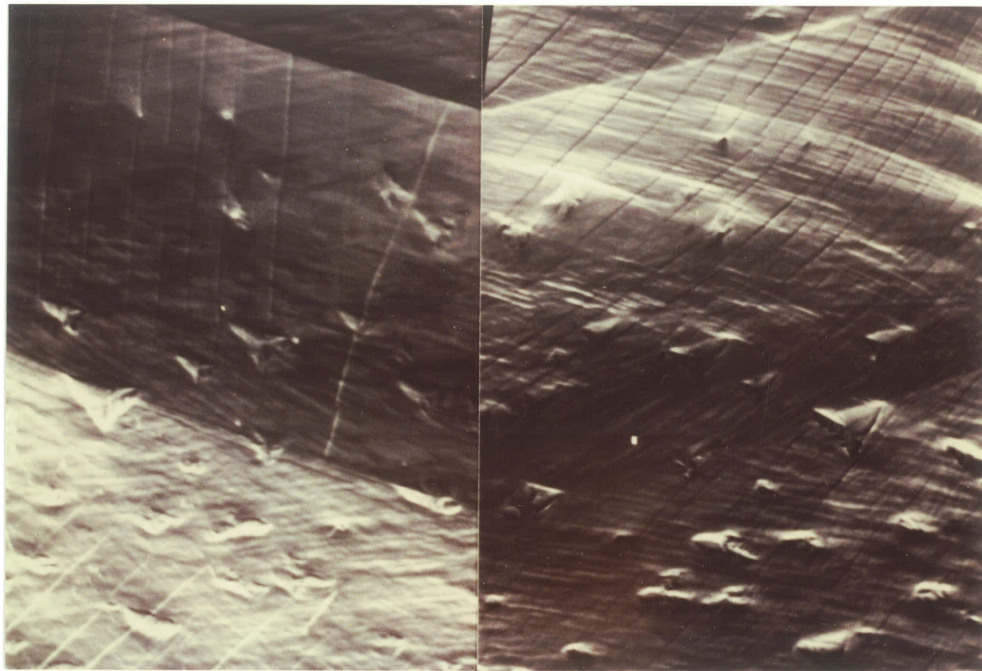


Figure 7.10: SEM fractograph of matching fracture surfaces on a specimen which was fractured intergranularly at 77K with segregated sulfur at grain boundaries.

### 7.3.2 Combined with Hydrogen Effect

When hydrogen was introduced into the aged specimens, the fracture strength was lowered further but was still above the yield stress. The fracture surface looks more brittle as shown in Fig.7.11. The photograph was taken at the surface edge of a rod specimen, which would have fractured intergranularly even if it had not been charged with hydrogen. A small grain almost dropped off, indicating extremely severe embrittlement around all its surfaces.

## 7.4 Hydrogen Effect on the Fracture Mode

### 7.4.1 Medium and Coarse Grained Specimens

#### 7.4.1.1 SEM Observations of Fracture Surfaces

Fracture surfaces in specimens with grain sizes of 50  $\mu\text{m}$  and 150  $\mu\text{m}$  were intergranular (Fig.7.12) except for the central area in the unaged specimens with short precharging periods, which was ductile rupture with dimples of various sizes (Fig.7.13). There was a transition band in between as shown in Fig.7.14. These three micrographs were taken in sequence on a single specimen, so that one could put them in order of 7.12, 7.14, and 7.13 to see a complete picture of fracture mode transition.

Generally speaking, the morphology observed is consistent with those reported in the literature [109,124]. A common occurrence on intergranular fracture surfaces is the existence of many rather straight lines, Fig.7.15. These lines are not matching on the two fracture surfaces and, therefore, are believed to be formed by release of dislocations in the pileups after fracture. Matching striations were observed only rarely, one example being shown in Fig.7.16. It can be seen that these striations are different than the straight lines of Fig.7.15; much more plasticity is evident in

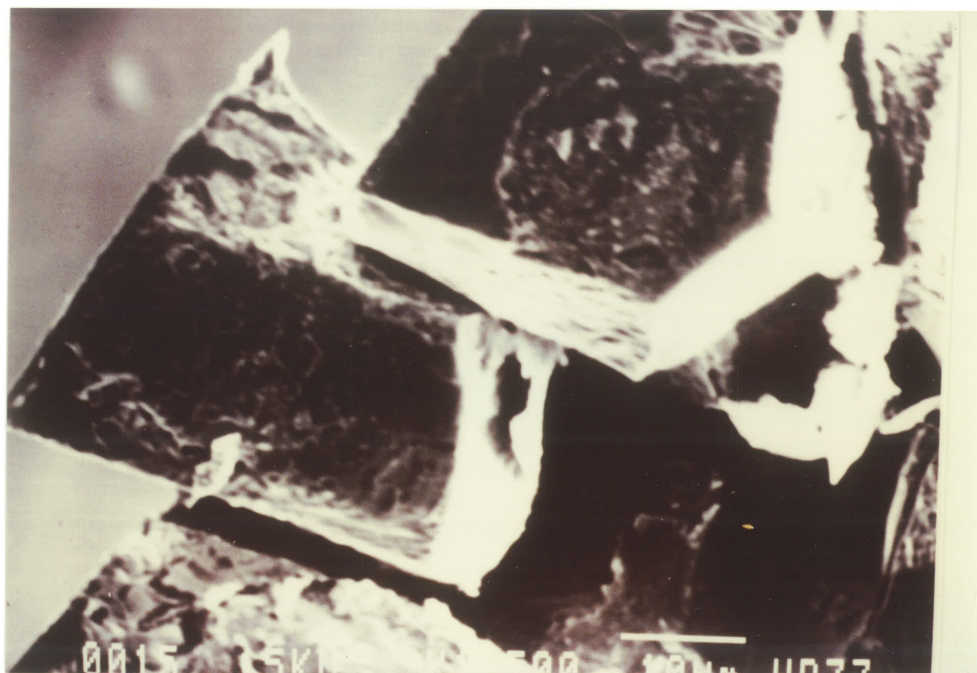


Figure 7.11: SEM fractograph of a coarse grained specimen fractured at 77K with segregated sulfur and pre-charged hydrogen.



Figure 7.12: SEM fractograph of a coarse grained rod specimen fractured at 77K with pre-charged hydrogen, close to charging surface.

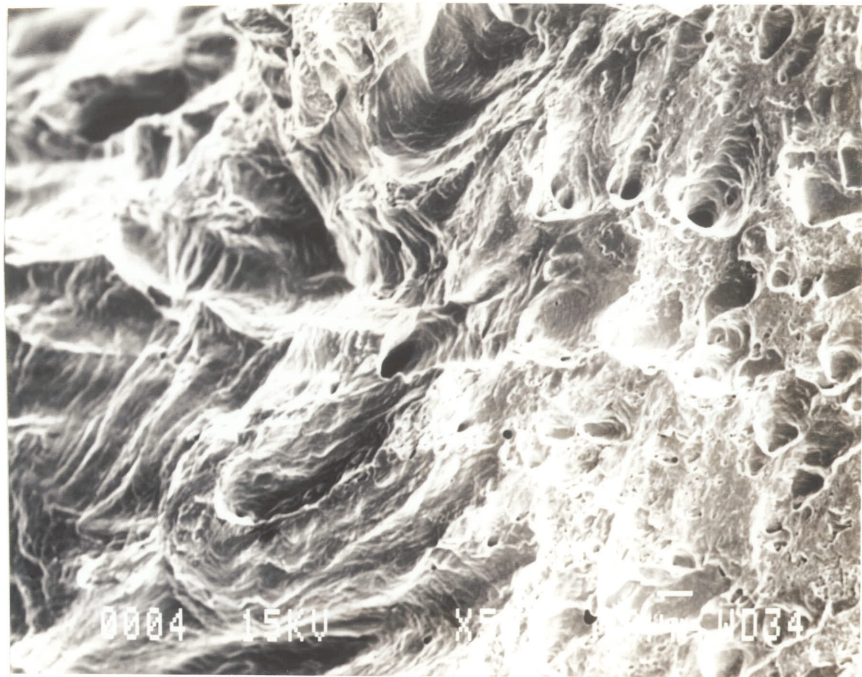


Figure 7.13: SEM fractograph of a coarse grained rod specimen fractured at 77K with pre-charged hydrogen, close to the center.

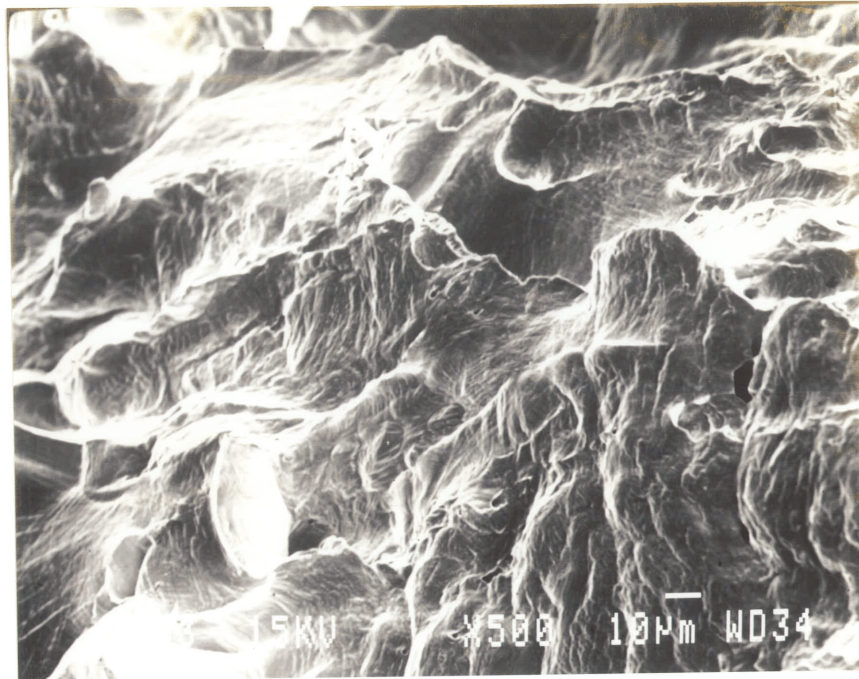


Figure 7.14: SEM fractograph of a coarse grained rod specimen fractured at 77K with pre-charged hydrogen, transition band.

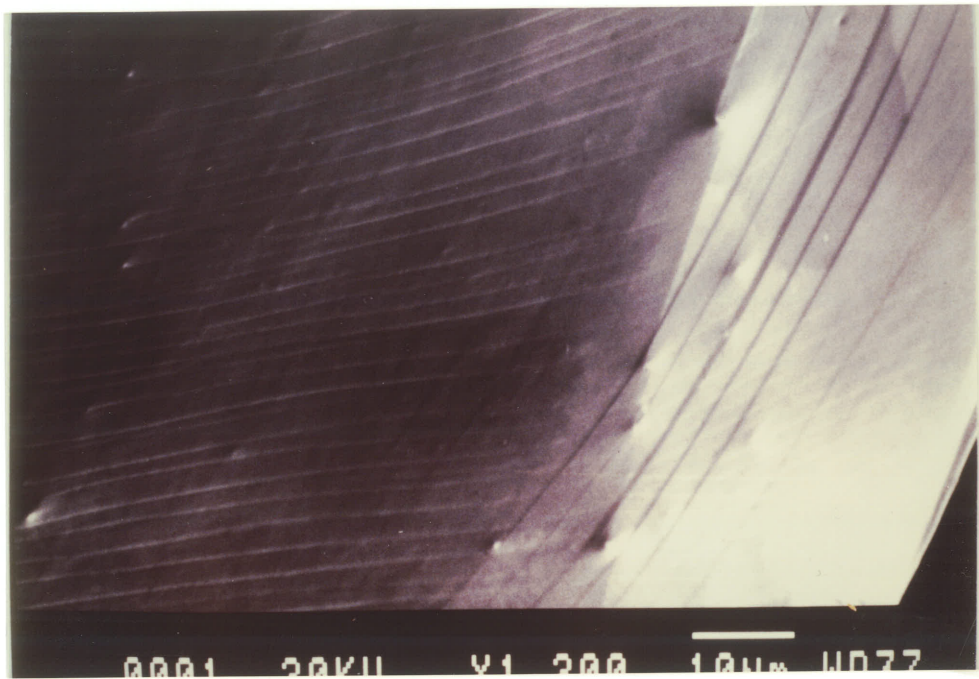


Figure 7.15: SEM fractograph of a coarse grained specimen fractured at 77K with pre-charged hydrogen.

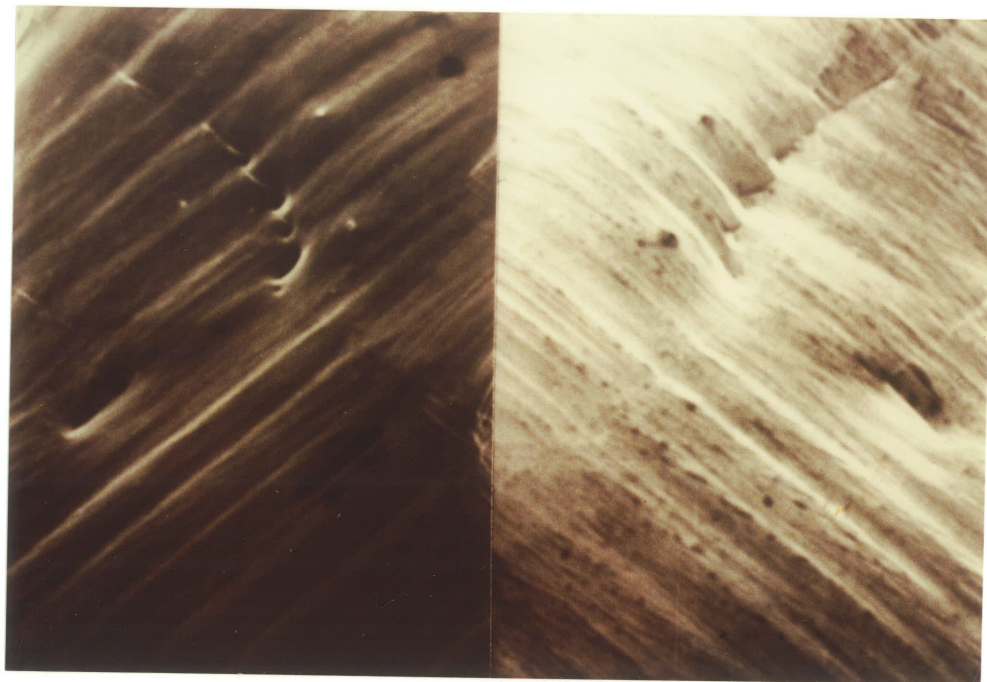


Figure 7.16: Matching striations on fracture surfaces of a specimen fractured at 77K with pre-charged hydrogen.

this case. Another feature is that the fracture surfaces consist of larger grains than average (Fig.7.17), which is in contrast with the case of sulfur induced intergranular fracture (Fig.7.7).

#### 7.4.1.2 Binding Energy and Critical Concentration for the Grain Boundary Plane to Fracture

The intergranular fracture depth is defined as the depth from the surface to the point where plasticity becomes apparent. As shown in Fig.7.18, it is not difficult to experimentally measure this depth, since its location is reasonably well defined. The measured depths of intergranular cracking in the membrane specimens with  $50\mu\text{m}$  grains charged for different periods are shown in Fig.7.19. Included are three curves calculated from eqn.(3.37). Curve 1 represents the lattice diffusion ( $K=1$ ). Curves 2 and 3 are calculated for  $K=100$  where grain boundary contribution becomes comparable to that of lattice (Curve 2 for grain size  $50\mu\text{m}$ , grain boundary contribution  $\sim 50\%$ ) or plays major role (Curve 3 for grain size  $10\mu\text{m}$ , grain boundary contribution  $>90\%$ ). In the calculation, Birnbaum's data [20] for the binding energy, lattice diffusivity and the ratio of the critical concentration,  $C_g^*$ , to the surface concentration,  $C_g^{\text{sur}}$ , were used; i.e.,  $E_b=11.6\text{ kJ/mol}$ ,  $D_l=5.11\times 10^{-10}\text{ cm}^2/\text{s}$  and  $C_g^*/C_g^{\text{sur}}=0.2$  which corresponds to 10 at%. If grain boundary transport dominates, the experimental curves should shift to shorter times. It can be seen that the measured data are at slightly longer times than Curve 1. If the trapping effect is not considered, the measured data could be estimated by a curve  $C_g^*/C_g^{\text{sur}} >0.2$ ; i.e.,  $C_g^* >10\text{ at}\%$ . Since the present study has shown the trapping effect of grain boundaries,  $C_g^*$  should not be much greater than 10 at%. On the other hand, if grain boundary trapping in Ni is considered to be severe, then the measured data



Figure 7.17: SEM fractograph of a specimen fractured at 77K with pre-charged hydrogen. Average grain size was  $50\mu\text{m}$ .



Figure 7.18: SEM fractograph of a medium grained specimen fractured at 77K with pre-charged hydrogen. The intergranular fracture depth is clearly seen.

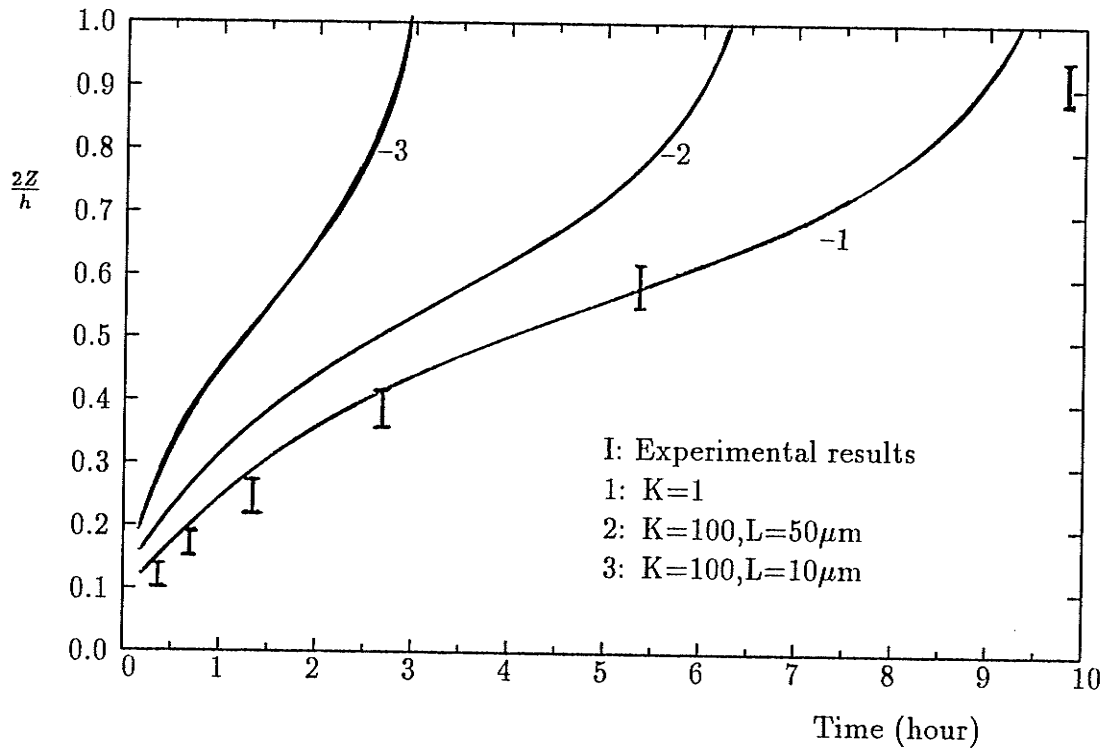


Figure 7.19: Measured IG cracking depths (normalized by half thickness of the membrane) vs pre-charging periods in unaged specimens with a grain size of  $50\mu\text{m}$ . All curves are calculated from eqn.(3.10). Curve 1 represents the lattice diffusion. The contribution from the grain boundary ies is 50% for curve 2 and  $>90\%$  for curve 3. Thickness  $h$  is  $190\mu\text{m}$  (after polishing).

would imply that  $C_g^*$  might be smaller than 10 at%. Since grain boundary trapping has been confirmed to be weak in Ni [125],  $C_g^*$  is unlikely to be below 10 at%. Therefore, it is reasonable that the measured data can be approximated by Curve 1 with the addition of a small trapping effect. Birnbaum's assumption that a critical concentration for intergranular cracking to occur appears correct, and for this grain size the critical concentration should be close to 10 at%. Floreen and Westbrook [126] reported that nickel specimens precharged with hydrogen up to 2000 appm at 365K did not fracture intergranularly at 77K. Using  $E_b=11.6$  kJ/mol, one finds  $C_g^* > 10$  at%. Therefore, the values of  $E_b$  and  $C_g^*$  determined by Birnbaum's group are supported by the consistency of these independent studies.

It is noted that the experimental curve locates to the right of the curve for lattice diffusion alone (Fig.7.19). This is consistent with the permeation and decoration test results that the hydrogen pre-segregated at grain boundaries causing intergranular cracking was transported mainly through lattice diffusion with grain boundaries acting only as hydrogen traps.

The stress-strain curves in specimens with medium grain size ( $50 \mu\text{m}$ ) saturated with hydrogen by prolonged charging are shown in Fig.7.20. The tensile strengths obtained from these curves as well as from fine grained specimens are shown in Fig.7.21. Curve d represents the fracture stress for the medium grain size specimens. It is seen that the fracture stress was greatly reduced ( $\sim 60\%$  deduction ) to a level about twice the elastic limit (Curve e) for medium grained specimens at both temperatures.

## 7.4.2 Fine Grained Specimens

A striking contrast to the above behavior of medium and coarse grained specimens was that when the same procedure was applied to the fine grained specimens,

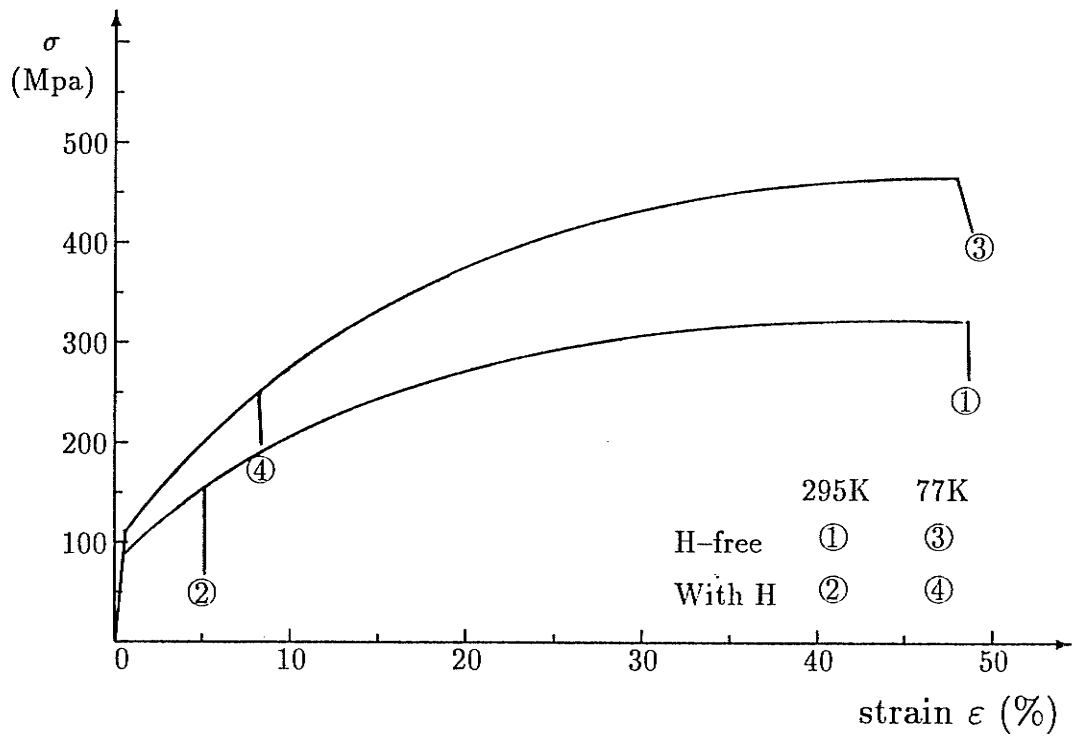


Figure 7.20: Stress strain curves in specimens saturated with hydrogen. Grain size  $50 \mu\text{m}$ .

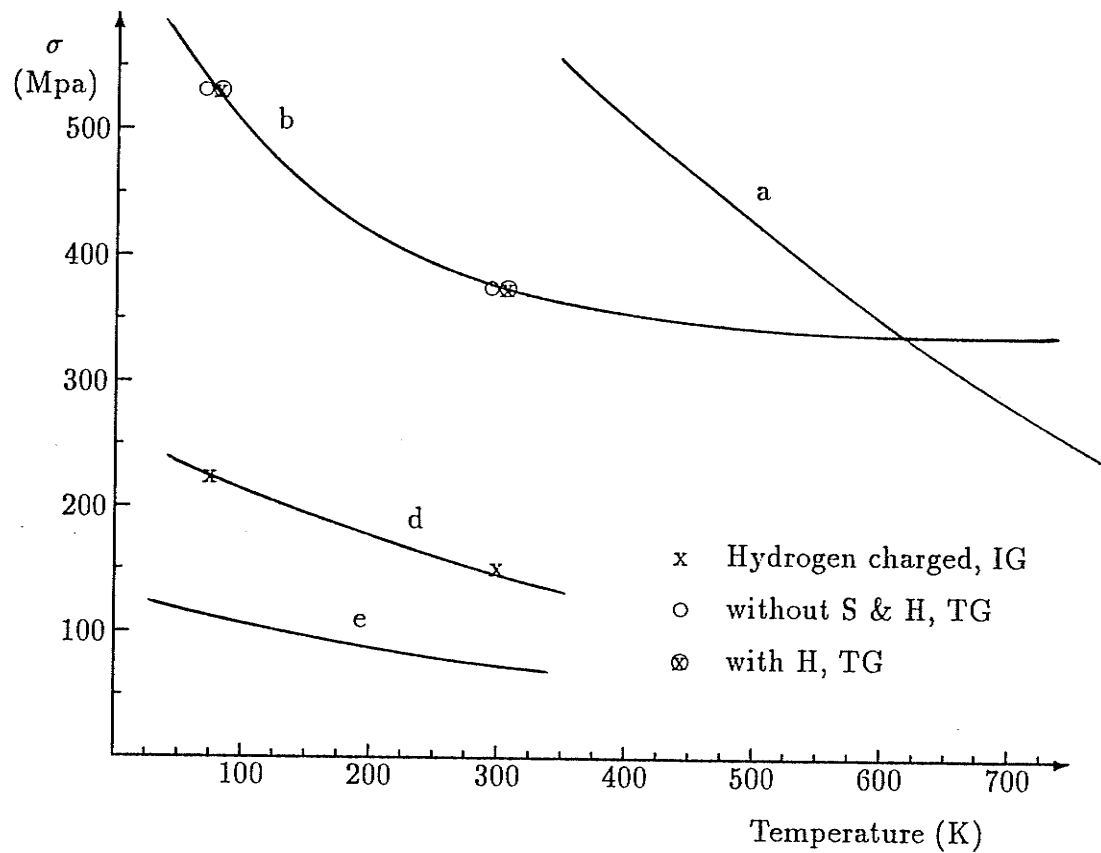


Figure 7.21: The ultimate strength and elastic limit vs temperature for grain size  $10 \mu\text{m}$ . Curve a represents grain boundary strengths. Curve d is obtained from hydrogen pre-saturated specimens with a grain size of  $50 \mu\text{m}$ . Curve e is the elastic limit.

no intergranular cracking could be obtained even when the precharging was prolonged to 70 hours. According to eqn.(3.32), in such long charging periods both grain interior and grain boundaries in the membrane should have been well saturated with hydrogen even if the  $K$  ratio is assumed to be zero; i.e., assuming hydrogen is transported only through the lattice. Nevertheless, the fracture stress surprisingly returned to curve b (Fig.7.21) which was obtained from specimens without sulfur or hydrogen segregation. The stress-strain curves look like as if hydrogen was not charged, Fig.7.22, if the surface damage is deduced.

The cross-section of the specimen at fracture reduced to a line (Fig.7.23). Shown in Fig.7.24a is the transgranular fracture surface of a large grain which was on the fracture path. A-A is the surface edge of the specimen, area B is the charging surface, which shows an embrittled surface layer, and area C is the transgranular fracture surface. Compared with the rupture surfaces of hydrogen-free area, Fig.7.24b, it is evident that dimples are shallow and much smaller. On the charging surface, many shallow cracks were observed mainly perpendicular to the stress axis on the side-face of the specimens, which are due to hydride formation. Such cracks in a specimen precharged at  $100\text{mA}/\text{cm}^2$  are shown in Fig.7.25. These cracks are along  $\{100\}$  planes as determined by the texture structure  $(100)\langle 001\rangle$  and sometimes along grain boundaries. This is consistent with the results of Vehoff and Klameth [127] who suggested that hydrogen induced brittle cracking in nickel single crystals is along  $(100)$  planes. It can be seen that some cracks (indicated by arrows) are parallel to the stress axis, indicating that the hydride strength is rather low; their fracture must have been a result of local dislocation activity. Such an observed grain size effect on the fracture mode has not been reported previously and is considered as an important observation which is difficult to explain by present

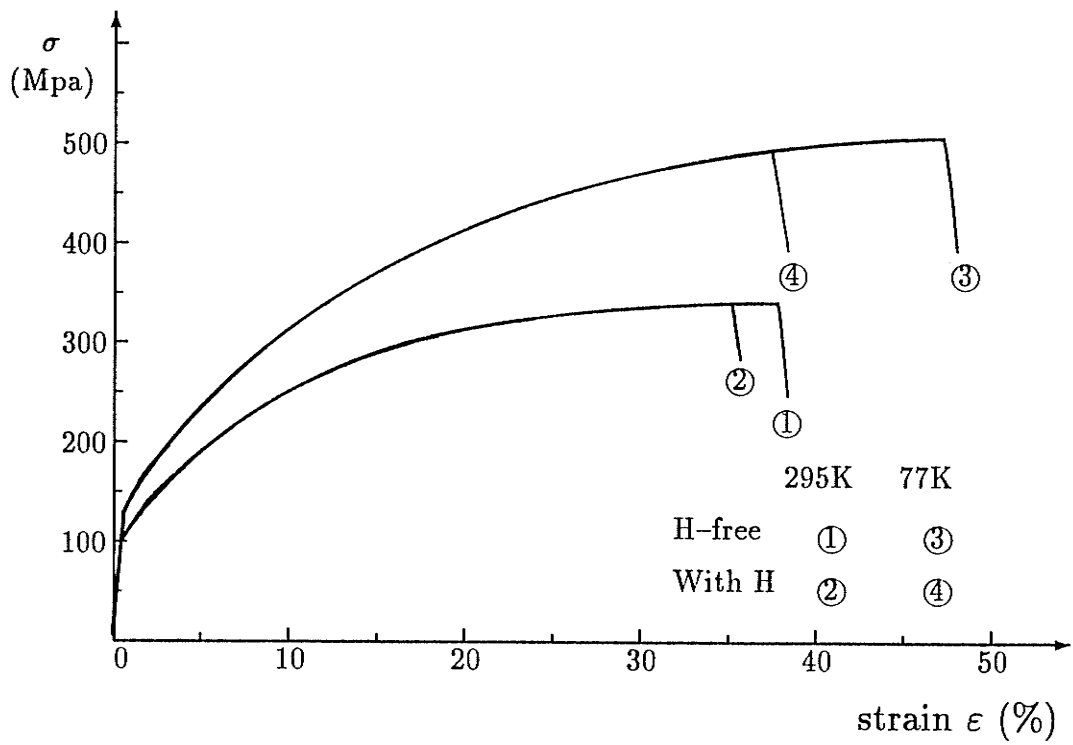


Figure 7.22: Stress strain curves in specimens saturated with hydrogen. Grain size 10  $\mu\text{m}$ .

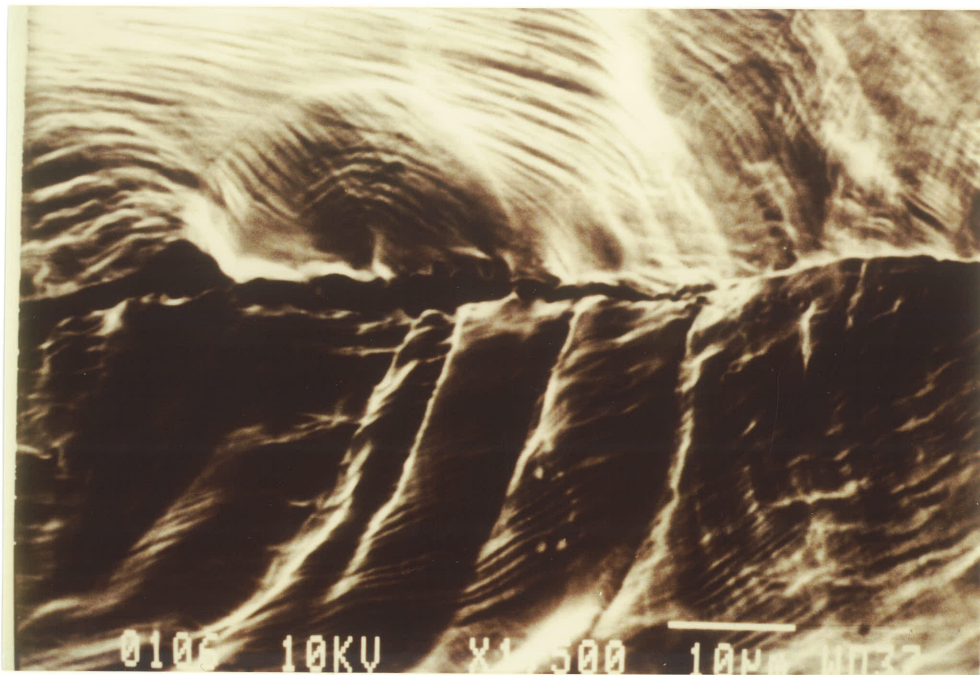


Figure 7.23: SEM micrograph of a fine grained specimen which was pre-saturated with hydrogen but fractured with full ductility. The reduction of area was almost 100%.

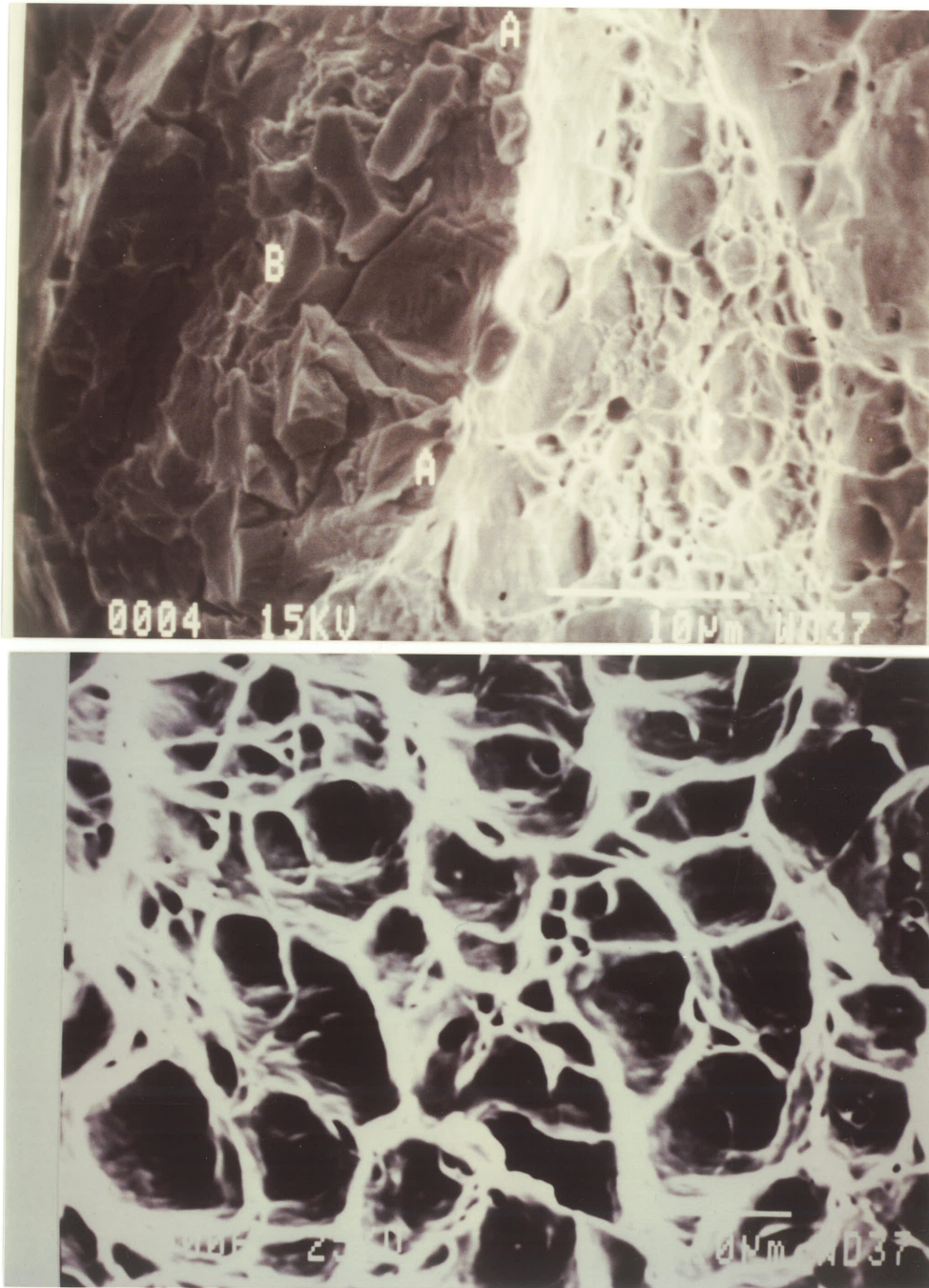


Figure 7.24: Comparison of transgranular fracture surfaces: (a) fine grained specimen pre-saturated with hydrogen and fractured transgranularly; (b) well developed dimples in central area of a rod specimen shown in Fig.7.13.

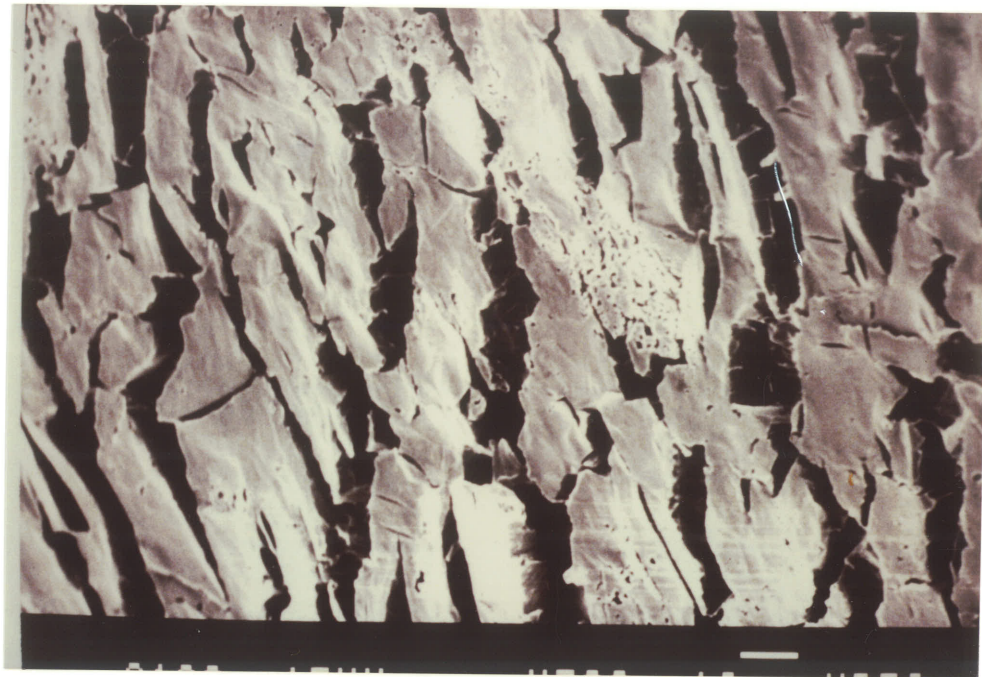


Figure 7.25: SEM micrograph of side surface of a fine grained specimen which was pre-saturated with hydrogen but fractured with full ductility. The external stress is horizontal.

proposed mechanisms and will be dealt with in next chapter.

In order to reveal fast transport of hydrogen through grain boundaries in penetration tests, it is better to use fine grained specimens as shown in Fig.7.1. However, since fine grained specimens did not fracture intergranularly, conclusions have to be made from the results of medium grained specimens which have been given in the last section.

# Chapter 8

## Discussions

### 8.1 Grain Boundary Transport of Hydrogen

#### 8.1.1 Dominant Process During Mass Transport of Hydrogen

Theoretical calculations predict that the fine grain size used in the present study should be able to reveal grain boundary enhanced transport. If grain boundaries play an important role, not necessarily dominant, it should have been observed in any one of the three tests used in this study. However, permeation tests performed in fine grained membranes failed to provide any evidence that supports enhanced transport of hydrogen by grain boundaries. All information obtained from the tests (e.g. the actual breakthrough time, steady state flux, and measured diffusivities) suggests that lattice diffusion is the dominant process. Results of the penetration tests yields the same conclusion.

Further, the silver decoration tests revealed that when the hydrogen concentration is extremely low (i.e. close to zero as is on the downstream surface during a permeation test),  $K$  approaches zero; i.e. there is virtually no hydrogen flux along grain boundaries. Therefore, the present results suggest that the lattice diffusion is the dominant process in most cases of hydrogen embrittlement in metals.

### 8.1.2 Explanation of Low $D_g$ at Low Concentrations

A close look at the experimental results suggests that hydrogen atoms can cross a grain boundary with ease although they experience much more difficulty in diffusing along the grain boundary at low concentrations. This can be understood by the following reasoning. To be more realistic, we assume that a grain boundary has a small percentage of specific sites where the energy level is much lower for hydrogen atoms than elsewhere. This idea is consistent with the coincidence site lattice (CSL) model of grain boundaries as outlined in Chapter 2. When hydrogen atoms drop into such sites, their escape would be extremely difficult. If these sites, i.e. deep traps, are arranged in a random way, their overall effect would still be negligible because of their low population. However, if they are arranged in distantly separated lines, they would be able to block the transport of hydrogen in certain directions before they are filled.

According to the CSL theory of grain boundaries, most grain boundaries possess an ordered or periodic structure [24]. For a symmetric tilt grain boundary, there are special tilt angles at which the boundary has a lower energy. When the crystal misorientation deviates from the special misorientation, the boundary can minimize its energy by forming a structure consisting of an array of intrinsic grain boundary dislocations (IGBDs) embedded in a boundary structure of relatively low energy. This results in the anisotropy of diffusivity in tilt boundaries. In a more general case, the boundary may have more than two sets of IGBDs, which meet at a certain angle. In this way, the transport of hydrogen in the grain boundary plane in any direction will be blocked if only these IGBDs are deep traps for hydrogen.

In fact, the binding energy of hydrogen to dislocations has been proposed to be high, e.g., 58.6 kJ/mol [7]. Therefore, it is reasonable to propose that sites

in grain boundary dislocation cores are indeed of much lower energy for hydrogen atoms. It is these sites that are responsible for the retardation of mass transport of hydrogen along grain boundaries at low concentrations, with no apparent effect on diffusion crossing the boundary. As for those low energy grain boundaries which do not have IGBDs, e.g., symmetric tilt grain boundaries with special tilt angle or twin boundaries, the diffusivity may be higher than that of random grain boundaries at low concentration. However, the binding energy and the segregation factor are also smaller, and the overall effect would be negligible.

### 8.1.3 $D_g$ at High Concentrations

Permeation test results (curve 6 in Fig.7.1) indicate that some weak trapping effect due to grain boundaries does exist. It has been mentioned that the theoretical model predicts that for the grain size used in the present study, there should be no retardation due to grain boundaries. Consequently, no trapping effect should be observed. This contradiction arises partly from the fact that the model has neglected those grain boundaries parallel to the membrane surface. Another reason is that the grain boundary diffusivity is concentration dependent. During evolution, hydrogen atoms in the deepest traps drain last. When recharging was applied before complete evolution, the grain boundary concentration was still higher than in the lattice. This is equivalent to a state where a higher average concentration exists; thus, the measured effective grain boundary diffusivity became larger than in the first run. However, compared with curve 2 of Fig.7.1, it can be concluded that the  $K$  ratio should be less than 10 during recharging.

### 8.1.4 Comparison with the Literature

It would appear ideal to use the finest grained specimens possible for the purposes of this study. However, since grains are so liable to growth in pure nickel, the grain size of  $10\ \mu\text{m}$  is the finest that could be made reasonably uniform. Therefore, comparison with literature data is necessary. Mütschele and Kirchheim [128] have investigated grain boundary diffusion of hydrogen using a different approach. They measured the diffusion coefficient of hydrogen at various bulk concentrations in nano-crystalline palladium (grain size  $\sim 5\ \text{nm}$ ). They found that the diffusion coefficient in single crystal materials was constant while it changed with concentration in polycrystalline materials. Since small grain sizes are accommodated by the new model, their data are reproduced in Fig.8.1 and analyzed here. Since the measured diffusion coefficient in polycrystalline metals has been averaged across grain boundary and grain interior areas, it should be considered an effective or apparent diffusion coefficient rather than representative of grain boundary or lattice diffusion. It is obvious that the effective diffusion coefficient should neither exceed the larger nor be less than the smaller of the two diffusivities,  $D_g$  and  $D_l$ . From Fig.8.1, it is seen that the maximum ratio of  $D_{\text{eff}}/D_l$  is about 3.5. If their data are extrapolated to  $C = 0$  the ratio of  $D_{\text{eff}}/D_l$  is about 0.05. Therefore, their data suggest that at  $C = 0$ ,  $K$  is no larger than 0.05 and at higher concentrations  $K$  is greater than 3.5.

The time-lag method is usually used to determine the diffusion coefficient and it has been shown in Chapter 4 that the effective diffusion coefficient obtained in this way can be expressed as

$$D_{\text{eff}} = \frac{1}{6\beta} D_l \quad (8.1)$$

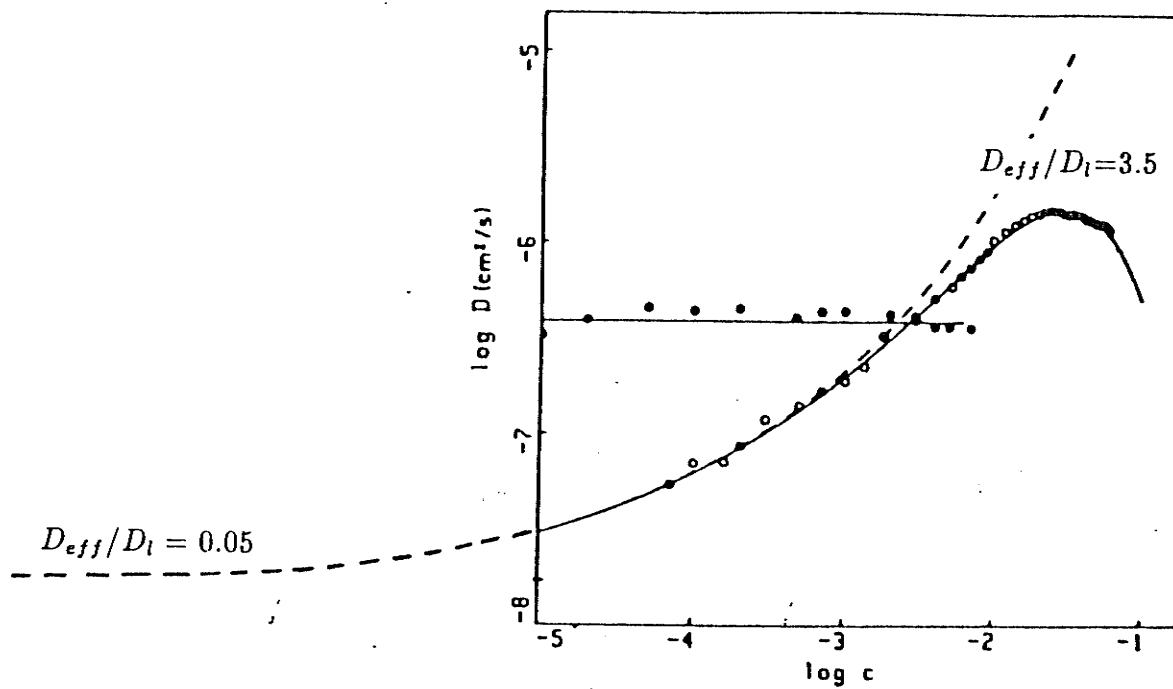


Figure 8.1: Re-produced Mütschele and Kirchheim's [128] measurement of hydrogen diffusion coefficient in single and polycrystalline palladium. The ratio of the latter to the former has a maximum value of 3.5 at high concentrations and a minimum of 0.05 extrapolated to low concentrations.

where  $\beta$  has been given in eqn.(4.8) as

$$\beta = \sum_{n=1}^{\infty} \sum_{m=1}^{\infty} \frac{(-1)^n 32 [J_1(\alpha_{nm} L/2) + as \alpha_{nm} J_0(\alpha_{nm} L/2)]^2}{(L + 4asK) n^2 \pi^2 \alpha_{nm}^2 [(L + 4as) J_0^2(\alpha_{nm} L/2) + L J_1^2(\alpha_{nm} L/2)]} \quad (8.2)$$

If the  $K$  ratio is assumed to be 0.05, and using values of  $h = 0.008\text{cm}$  and  $L = 5 \times 10^{-7}\text{cm}$ , it was found by trial and error that to obtain the extrapolated value of  $D_{\text{eff}}/D_l = 0.05$ , the value of the segregation factor  $s$  must be greater than 7900, implying a binding energy of  $E_b = 22 \text{ kJ/mol}$ . Kimura and Birnbaum [13] reported a value of 11.6 kJ/mol for nickel. Since Pd and Ni are both face centred cubic and are generally quite similar metals, it is reasonable to expect the grain boundary binding energy for Pd to be in the same range as that for Ni. In fact, Mütschele and Kirchheim [128] suggested an average binding energy of 5.3 kJ/mol for hydrogen with grain boundaries in Pd. Therefore, 22 kJ/mol is unrealistically high.

If  $K$  is assumed to be zero as suggested by the silver decoration test, the  $s$  value reduces to 48 which corresponds to a binding energy of  $E_b = 9.47 \text{ kJ/mol}$ . Mütschele and Kirchheim found that if a single binding energy is used to describe the distribution of hydrogen, its value would have to change with concentration and the segregation factor would be in a range from 10 to 100. The  $s$  value of 48 is apparently a fair approximation. Therefore, their results are consistent with the present study; i.e., when the hydrogen concentration is close to zero, there is little hydrogen transport through grain boundaries.

Substituting the value of 9.47 kJ/mol for the binding energy into eqn.(3.10), the value of  $K$  is found to be 3.6 when  $D_{\text{eff}}/D_l = 3.5$ . Therefore, Mütschele and Kirchheim's data also suggest that grain boundary enhanced transport of hydrogen will never play an important role since  $K$  is not much greater than unity at any concentration.

### 8.1.5 Distinguishing Fast Paths from Short Circuit Paths of Diffusion

When the value of  $K$  is about unity, even if  $s$  is large and the grain size small, the mass transport of hydrogen is not accelerated by grain boundaries. However, most flux would still be via grain boundaries. In this case, the grain boundaries act as short circuit paths for diffusion. Therefore, it is necessary to distinguish between short circuit paths and fast paths for diffusion. For the latter, it has the specific meaning that the diffusion coefficient is larger in the paths than in the lattice, while for the former, it can be a result of the segregation effect. A short circuit path is not necessarily a fast path for diffusion.

In the literature, there have been continuing attempts to obtain direct experimental evidence of enhanced transport of hydrogen by grain boundaries. For example, autoradiography was used by Abraham et al. [27] and an ion microprobe (IMA) technique was used by Tsuru and Latanision [14]. In those tests, traces of hydrogen or tritium were detected on one surface of the testing membrane which had been precharged from the other side for a period less than the breakthrough time. They considered that hydrogen/tritium could not have reached the downstream surface in this period through lattice diffusion. Therefore, their conclusion was that hydrogen must have diffused through the fast diffusion paths, i.e., grain boundaries. However, it seems that the breakthrough time was incorrectly interpreted and misused. The breakthrough time is defined as the intersection of the tangent at the inflection point on the anodic current with the background anodic current. At this time there should have been a considerable amount of permeating flux according to theoretical calculations [17]. If the actual breakthrough time,  $t_a$ , is used and the sensitivity of the monitoring system is assumed to be sufficient, the charging periods used in

their studies would approach or even exceed that required for hydrogen/tritium to appear at the downstream surface through lattice diffusion.

If  $K = 0$ , i.e.  $D_g = 0$ , it can be demonstrated by using eqn.(3.32) that for nickel and palladium of ordinary grain size ( $\geq 1\mu\text{m}$ ), where the grain boundary binding energy is relatively low, the concentration buildup in grain boundaries will progress with that in the lattice. In other words, the retardation effect due to grain boundaries perpendicular to the membrane is very limited. When hydrogen/tritium reaches the downstream surface in grain interiors, it also appears in grain boundary areas. Further, since  $D_g$  has been shown to be not always smaller than  $D_l$ , it can be concluded that the hydrogen concentration in grain boundaries will never fall below that in the lattice. Consequently, autoradiography and IMA techniques would yield grain boundary patterns if the membrane has been precharged for a period comparable to that required for hydrogen to appear at the downstream surface by lattice diffusion. Since neither of the techniques 'freezes' hydrogen atoms during detection, further diffusion may take place. Therefore, it seems that the reported evidence can not be considered as evidence of fast diffusion, but rather of the segregation effect,

### 8.1.6 Dislocation Pipe Diffusion of Hydrogen

There is evidence in the literature that moving dislocations can transport hydrogen atoms [98,99]. However, arguments exist regarding the role of stationary dislocations. Kirchheim [129] and Bucur and Indrea [130] observed a double plateau phenomenon during hydrogen permeation in deformed palladium. The first plateau was quite instantaneous and was ascribed to the fast filling of dislocation cores. However, if the filling rate of dislocation cores is high, there would be no reason for the diffusion process in dislocation cores to slow down in the later stages of a permeation test. Therefore, a much higher effective diffusion coefficient should be

obtained. However, in the present study it was found that both breakthrough time in the permeation tests and incubation period in the decoration tests increased if the membrane was cold worked, indicating that dislocations are not fast diffusion paths. This is consistent with the work by Louthan et al [17]. From the present test results regarding grain boundary transport, attributing the double plateau phenomenon observed in deformed palladium to rapid dislocation network transport of hydrogen seems to be questionable.

## 8.2 Grain Size Effect on the Fracture Mode

The important observation that hydrogen does not embrittle fine grained specimens has not been previously reported. Therefore, before trying to explain this phenomenon, it is desirable to determine if it could be a result of some other effect. There appears to be only three possibilities: 1) there was much less hydrogen entering the fine grained specimens. Therefore the average concentration was much lower than that in coarse grained specimens; 2) grain boundaries in these specimens are of a special kind which either cannot segregate sufficient amount of hydrogen or are immune to hydrogen embrittlement; and 3) segregated sulfur was so low that grain boundaries were too clean to be fractured by hydrogen alone.

To rule out the first possibility, hydrogen outgassed from the membranes which were precharged to saturation ( $> 3$  days) was collected. The membrane was immersed in silicon oil covered by a glass funnel which had a calibrated dead-end tube. The outgoing hydrogen bubbles replaced the oil in the tube and concentrated there. It was found that for a charging area of  $1.5 \text{ cm}^2$  on each side and a current density of  $10 \text{ mA/cm}^2$ , the collected amount of hydrogen for both grain sizes was in a range of  $2\text{-}10 \text{ ml/cm}^3$ , changing from membrane to membrane. No

systematic difference between the amount of outgassed hydrogen from fine grained specimens and that from coarse grained ones was found. Assume each grain has a radius  $L/2$ , the volume percentage of grain boundaries is estimated as

$$\frac{\pi L^2 a}{1/6\pi L^3} = \frac{6a}{L} \quad (8.3)$$

and the number of metal atoms in grain boundaries per unit volume would be  $(6a/L)/(4/3\pi r^3)$ , where  $r$  is the radius of metal atoms.

Assume grain boundaries have been saturated to 1:1, using  $L=0.001$  cm and  $a = 2r$ , the number of hydrogen atoms per unit volume would be  $3 \times 10^{18}$ , which equals  $5 \times 10^{-6}$  mol. At room temperature and one atmosphere, this amount of hydrogen would occupy  $22.4l \times 5 \times 10^{-6} = 0.1$  ml. Compared with the collected hydrogen, it is seen that even in the fine grained specimens, most hydrogen was stored in the surface layer in hydrides. Further, after fracture at 77K, hydrogen could still be collected from fine grained specimens. Further, as already shown in Fig.7.24, grain interiors of fine grained specimens were indeed embrittled by hydrogen. Therefore, it is concluded that grain boundaries in fine grained specimens should have been saturated with hydrogen as were coarse grained specimens.

The fine grained specimens were highly textured with a large percentage of small angle grain boundaries, which may be argued to have a lower binding energy with hydrogen. However, when the specimens were given a re-annealing at 1173K for 10 minutes to obtain coarse grains before precharging with hydrogen, intergranular cracking was again observed. It was confirmed by X-ray analysis that the microstructure was still heavily textured after re-annealing. This is consistent with the generally accepted concept that recrystallization at a lower temperature yields a more random structure [131]. Therefore, it can be concluded that the mechanical features of grain boundaries did not change significantly during annealing.

On the other hand, the grain boundary area per unit volume increases as the grain size decreases. Therefore, for a fixed quantity of impurities in the solid, the impurity concentration at grain boundaries must decrease. Morgan and McMahon [110] argued that clean grain boundaries may not suffer from hydrogen induced intergranular cracking. However, since annealing at 1173K causes little segregation of sulfur [109,124,132], the sulfur concentration at grain boundaries in the specimens with medium and coarse grains obtained during re-annealing should not be high. On the other hand, there has been evidence that moving grain boundaries can carry sulfur atoms during recrystallization [124,132], so that grain boundaries in fine grained specimens may not be sulfur free. Therefore, the chemical compositions of grain boundaries in both groups of specimens should not be substantially different. Further, hydrogen induced intergranular cracking in solution annealed Ni270 was observed where no sulfur segregation could be detected by Auger Electron Spectroscopy [109,133,134]. Rice [135] has proposed a model to predict intergranular cracking in metals, which also suggests that hydrogen induced intergranular fracture in pure nickel is possible.

Therefore, it can be concluded that all of the three possibilities can be ruled out. The lack of intergranular cracking in fine grained specimens is directly related to the grain size effect.

### **8.3 The Mechanism of Hydrogen Induced Intergranular Cracking**

At 77K, hydrogen diffusivity would be in the order of  $10^{-29}\text{cm}^2\text{s}^{-1}$  if Louthan et al's [119] data is extrapolated. According to Tien et al [136], the critical velocity

for a dislocation to break away from its hydrogen cloud is

$$V_c = \frac{D_l E_b}{30kTb} \quad (8.4)$$

which is many orders of magnitude smaller than the dislocation velocity corresponding to the strain rate used in this study,  $10^{-2}\text{s}^{-1}$  to  $10^{-4}\text{s}^{-1}$ . Therefore, the dynamic interaction of hydrogen with dislocations is negligible. There should be little transport of hydrogen by dislocations from or to the grain boundaries. The intergranular fracture observed in coarse grained specimens thus must be due to local hydrogen through the following two ways:

- 1) reduction in the resistance force to intergranular cracking;
- 2) increase of the driving force for intergranular cracking.

### 8.3.1 Decohesion Theory

Although it has been speculated that hydrogen reduces cohesive strength, so far there has been no direct evidence in the literature. Hsiao's [137] group has provided indications that such a reduction in cohesive strength is only a small fraction, about 10%. Therefore, the observed large reduction in the fracture stress ( $\sim 60\%$ ) in coarse grained specimens cannot be solely attributed to the reduction in the resistance force. Further, if the grain boundary strength were reduced to such a degree by either decohesion or hydride formation, at a given applied stress, the tensile stress applied on the grain boundaries in the fine grained specimens would not be much different from that in coarse grained ones. Therefore, the fine grained specimens should also have fractured intergranularly. This is evidenced by the small grains on the fracture surface shown in Fig.7.7.

### 8.3.2 Increase of the Driving Force

It is well known that the leading dislocation in a pileup can exert a force,  $\sigma_p$ , onto its barrier  $N$  times larger than the applied stress,  $\sigma_a$ , where  $N$  is the number of dislocations in the pileup. The more dislocations a pileup contains, the greater the local stress it produces. The following two processes can reduce the number of dislocations in a pileup.

First, if the stacking fault energy (SFE) is high as in Al, pileups can be blunted without difficulty through cross slip and local stresses are relaxed. If hydrogen reduces the relaxation ability of dislocation pileups, the number of dislocations in a pileup will increase, higher normal tensile stresses can build up at grain boundaries, and intergranular cracking may be observed. Cornet *et al* [138] applied this mechanism in iron, but Oriani [8] argued it might not be meaningful since the SFE of iron is rather high. Because nickel has a much lower SFE, this mechanism may work in our case. However, under the conditions of the present study, specimens precharged at room temperature but fractured at 77K, only the leading dislocation in the pileup is in a high concentration of hydrogen. Blunting could nevertheless occur somewhere a small distance away from the leading dislocation, where the dislocations would be hydrogen free. Further, this mechanism does not work in pileups of edge dislocations which do not cross slip. Therefore, this mechanism can at most play only a secondary role in the present case.

Second, when local accumulated stress is sufficiently high, the leading dislocation is forced into and slides along the grain boundary, and then emerges in the adjacent grain with a new Burgers vector. Dingley and Pond [139] hypothesized that in hard grain boundaries the separation of the dislocation products of extrinsic grain boundary dislocations (EGBDs) is difficult and therefore the above process

has to overcome higher resistance. They used this idea to explain the embrittlement effect of segregated impurities, which, however, has received little attention. Adopting their idea, we propose a new mechanism for hydrogen induced intergranular cracking in metals as follows.

### 8.3.3 New Mechanism for Intergranular Cracking

We assume that in the absence of hydrogen, the resistance of the controlling process for a lattice dislocation to cross a grain boundary,  $\sigma_g^r$ , is low in these metals. The controlling process may either be the impingement or the dissociation of the lattice dislocations. Therefore, pileups in these metals are never fully built up. In other words, the grain boundary could have withstood more dislocations in the pileups. It is hypothesized that hydrogen can increase this resistance, i.e.,  $\sigma_{g(H)}^r > \sigma_g^r$ . Therefore, pileups are given a second chance to fully develop in the presence of hydrogen. The number of dislocations in the pileup would increase, which in turn would raise the local stress at the grain boundary,  $\sigma_p$ . When  $\sigma_p$  exceeds the grain boundary strength,  $\sigma_g^*$ , intergranular cracking occurs.

Since the upper bound of  $\sigma_p$  is  $\sigma_g^r$ , this mechanism suggests that it is the relative ease or difficulty to the entrance of the leading dislocation into the grain boundary that determines if the fracture mode changes when hydrogen is present at grain boundaries. If  $\sigma_g^r > \sigma_g^*$ , pre-segregated hydrogen at grain boundaries would not change the fracture mode. Intergranular cracking is the preferred fracture mode in this case. If  $\sigma_g^r \ll \sigma_g^*$ , hydrogen may not be able to raise  $\sigma_g^r$  to  $\sigma_g^*$ . In case it does, then the number of dislocations in the pileup has to be substantially increased in order to raise the local stress. Therefore, hydrogen can change the fracture mode only when SFE is not large. When  $\sigma_g^r$  is smaller than but comparable to  $\sigma_g^*$ , intergranular cracking may occur even when SFE is large since a small increase in

$N$  could raise  $\sigma_p$  to above  $\sigma_g^*$ . This might be the explanation why hydrogen changes fracture mode from transgranular to intergranular in high purity iron which has a high SFE [42]. The present case may locate in between the latter two groups.

This mechanism explains the results reported in the literature and observed in the present study that a few percent, 2 ~ 10%, plastic deformation is necessary and sufficient condition for hydrogen induced intergranular cracking to occur in coarse grained specimens where the fracture strength could be reduced by 60%. In this range of deformation, pileups are the dominant low energy dislocation structure in the material.

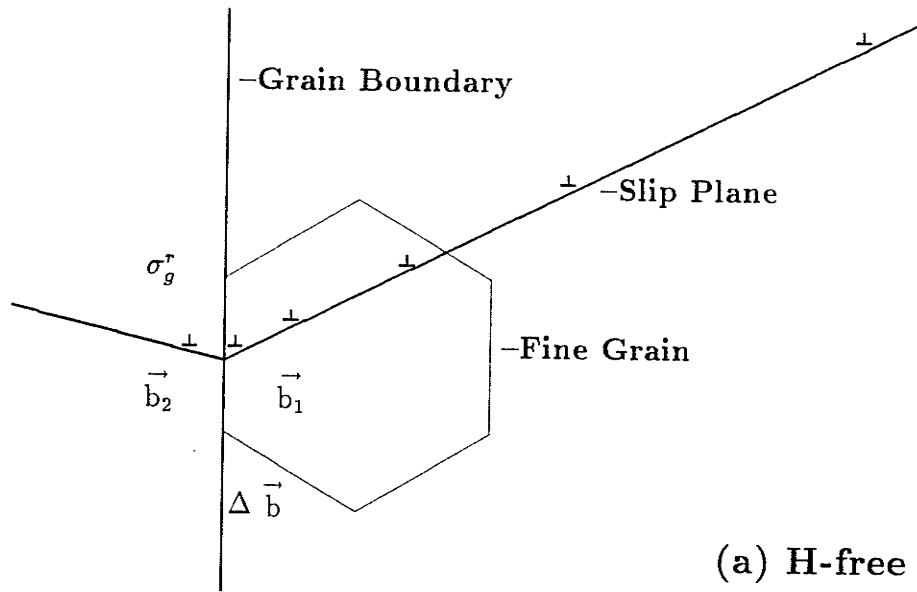
This mechanism also explains the recovery of the tensile properties for fine grained specimens. It is known that the number of dislocations in a pileup is proportional to the length of the pileup which is limited by the grain size. The stress exerted onto its barrier by a pileup,  $\sigma_p$ , and the stress at a distance of  $r$  from its head,  $\sigma_d$ , are [140]

$$\sigma_p \propto N\sigma_a \propto \sigma_a^2 L \quad \text{and} \quad \sigma_d = \sigma_a \left(\frac{L}{r}\right)^{1/2}$$

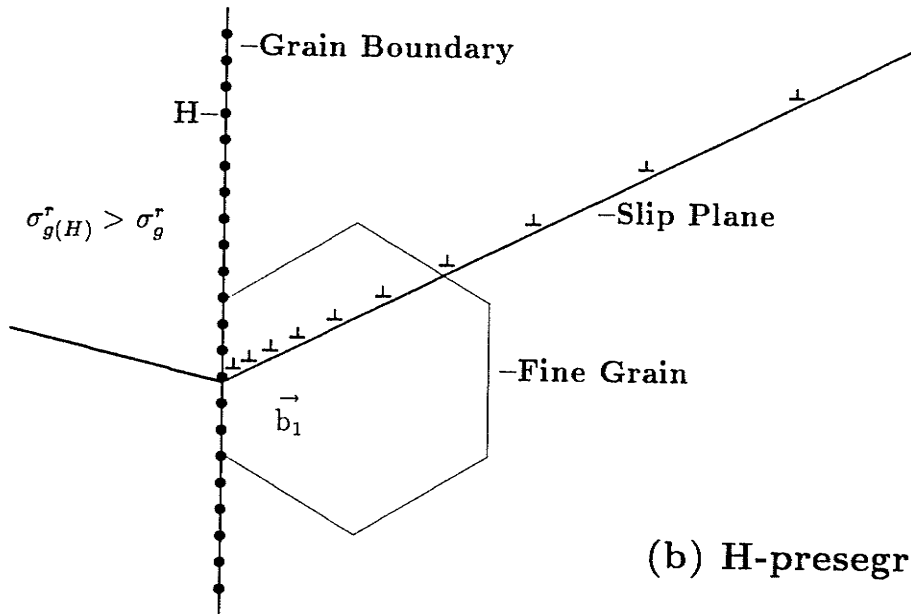
respectively. The latter will activate dislocation sources in the next grain and thus transfer plastic deformation. It is clear that intergranular fracture is favored in coarse grained specimens if pileups play an important role in the fracture processes, since the ratio of  $\sigma_p/\sigma_d$  is proportional to  $L^{1/2}$ . If stressed to the same  $\sigma_a$ , since  $L_f = 0.2L_c$ , thus we have  $\sigma_p^f = 0.2\sigma_p^c$ . The sub- and super-scripts f and c stand for fine and coarse grained specimen, respectively. Therefore, in order to obtain intergranular cracking in fine grained specimens, i.e.,  $\sigma_p^f = \sigma_p^c$ ,  $\sigma_a$  has to be increased by  $\sqrt{1/0.2} = 2.24$  times. However, since  $\sigma_d$  is well above the yield stress,  $\sigma_s$ , (though it is also reduced by a factor of 2.24 for a given  $\sigma_a$ ) and since hydrogen does not significantly affect grain interior deformation processes under the present conditions

(mobile dislocations are hydrogen free), large scale plasticity may occur in grain interiors as  $\sigma_a$  increases. It is known that other low energy dislocation structures, e.g., dislocation cells, start to form during or even before stage II work hardening [141,142], which in turn shortens the length of pileups. Therefore, before  $\sigma_a$  is increased to the level required for intergranular fracture to occur, the grain interior strength has been reached. Consequently, intergranular cracking does not occur, which is shown in Fig.8.2.

This mechanism is consistent with the scanning electron microscopy results. Fig.8.3 shows a grain boundary triple point area on a specimen side surface (grain size  $150\mu\text{m}$ ) deformed at room temperature in the absence of hydrogen. This specimen had segregated sulfur at grain boundaries and would have fractured intergranularly if tested at 77K. It can be seen that dislocations can easily cross the grain boundary and two grains glide with each other forming a step at the boundary. Note the height of the step,  $\sim 10\mu\text{m}$ , indicating numerous dislocations have crossed the boundary. However, when the specimens were fractured in the presence of hydrogen, the grain surfaces were flat and quite featureless except for the existence of many clear and rather straight slip lines (Fig.7.15). This means the plasticity was not continuous across the grain boundaries and dislocations were blocked at the boundary and released after fracture making these slip lines. When hydrogen is added to the specimens with segregated sulfur, the morphology looks more brittle (Fig.7.11) than that caused by hydrogen alone, indicating that the effects of sulfur and hydrogen are additive. This is straight forward according to the present model since they operate in different mechanisms: sulfur reduces the resistance while hydrogen mainly contributes the driving force for intergranular cracking. Since  $2 \sim 10\%$  plastic strain is needed for hydrogen induced intergranular fracture, the model predicts that as long



(a) H-free



(b) H-presegregated

Figure 8.2: New mechanism for intergranular fracture due to hydrogen.

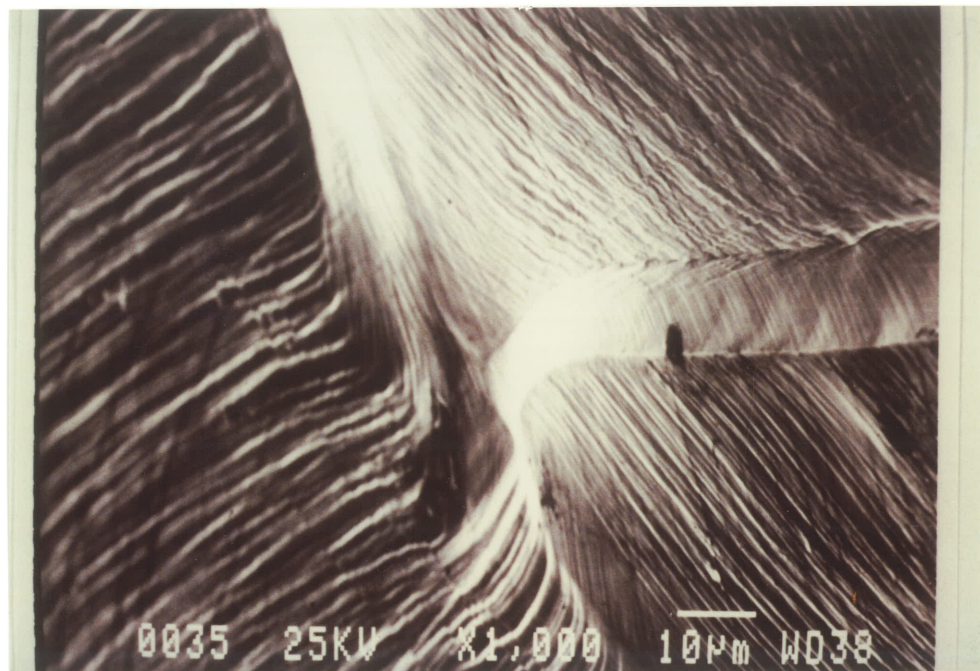


Figure 8.3: SEM micrograph showing an area around a grain boundary triple point on a specimen side surface which was fractured at room temperature in the absence of hydrogen but with segregated sulfur at grain boundaries.

as the ultimate strength of the metal has not been reduced by sulfur to around the yield strength, hydrogen will further embrittle the material.

Verpoort et al [143] have reported that cold work changed the fracture path in nickel from intergranular to transgranular. They did not give the reason but considered grain boundaries to be fast diffusion paths. Their observation can be explained by the new mechanism: severe cold work forms dislocation structures other than pileups in the material, which limits the number of dislocations present in a single pileup. Thus, the critical stress can no longer be established at grain boundaries.

To summarize, the present study advances a new model for hydrogen induced intergranular cracking in Ni. However, it does not exclude the possibility that grain boundary strength,  $\sigma_g^*$ , may have been simultaneously reduced by segregated hydrogen; i.e., the decohesion effect may also contribute. Nor does it exclude the role that hydrogen transport by moving dislocations may play at a higher temperature, since only the pre-segregated hydrogen at grain boundaries has been addressed in this study. However, this study does not support Birnbaum's model which suggests that intergranular fracture is not in the grain boundary planes, but rather along active slip planes in the vicinity of grain boundaries. If that is true, the mating fracture surfaces should match each other as shown in Fig.7.16, which has rarely been seen.

# Chapter 9

## Conclusions and Recommendations

### 9.1 Conclusions

The present study has clarified some important issues regarding hydrogen induced intergranular cracking. The main findings are summarized as follows.

1. An analytical solution for diffusion involving a realistic grain boundary pattern in a finite system has been obtained. The model accommodates a small grain size, the segregation factor, and a large range of  $K$  values.
2. The model is used to predict the permeation rate during an electrochemical permeation test. Enhanced transport by grain boundaries will shift the permeation curve to shorter times than that for lattice diffusion alone and also to higher permeation rates, which will result in a higher effective diffusion coefficient determined by the conventional time-lag method.
3. There should not be a double-plateau phenomenon on a permeation curve no matter how fine the grain size. If grain boundary transport plays a key role during the mass transport of hydrogen, the actual breakthrough time should be greatly reduced.

4. For most metallic materials, an average grain size of  $10\mu\text{m}$  should be sufficient to reveal enhanced grain boundary transport of hydrogen even when lattice diffusion is dominant.
5. Fast diffusion paths should be distinguished from short circuit diffusion paths. The former infers a higher diffusivity in grain boundaries, while the latter infers a large segregation factor. The observation of a higher steady state permeation rate most likely results from a high segregation factor rather than enhanced transport by grain boundaries.
6. Grain boundaries are not high diffusivity paths for hydrogen and will not likely play an important role during the mass transport of hydrogen in metals. The role played by grain boundaries is retardation of transport via their weak trapping capacity.
7. The grain boundary diffusivity of hydrogen is concentration dependent. When the hydrogen concentration is extremely low, the grain boundary diffusion of hydrogen is virtually stopped. It is postulated that intrinsic grain boundary dislocations are responsible for such retardation.
8. Hydrogen does not change the fracture mode in pure nickel at 77K from transgranular to intergranular in specimens with a grain size of  $10\mu\text{m}$ .
9. The experimental results in this study support Birnbaum's data; i.e., the binding energy of hydrogen to grain boundaries in Ni is 11.6 kJ/mol and the critical hydrogen concentration to cause intergranular cracking at 77K is about 10 at%.
10. Segregated sulfur and hydrogen at grain boundaries cause intergranular fracture through different mechanisms. Sulfur reduces the grain boundary cohe-

sive strength. When the external stress exceeds the grain boundary strength, intergranular cracking occurs. Hydrogen increases the resistance of a grain boundary to the entrance of the leading dislocations in dislocation pileups, which results in an increase in the number of dislocations held in a pileup. When the tensile stress against the grain boundary raised up by dislocations exceeds the grain boundary strength, intergranular cracking occurs. Therefore, their effects can be additive in most cases.

## 9.2 Recommendations

Although a general picture of hydrogen induced intergranular cracking in nickel has been established through this study, it is highly recommended that the following work be carried out in the future:

1. Using Auger Electron Spectroscopy to quantitatively establish the relation among the grain boundary strength, the grain boundary sulfur concentration, and the grain sizes.
2. Using transmission electron microscopy to compare dislocation pileups in fine and coarse grained specimens in the absence and presence of hydrogen.

# Bibliography

- [1] *Effect of Hydrogen on Behavior of Materials*, A. W. Thompson, I. M. Bernstein eds., AIME, N.Y., 1976.
- [2] *Hydrogen Effect in Metals*, I. M. Bernstein and A. W. Thompson, eds., AIME, Warrendale, PA, 1980.
- [3] *Environmental Degradation of Engineering Materials in Hydrogen*, M. R. Louthan, Jr., R. P. McNitt, R. D. Sisson, Jr., eds., Virginia Polytechnic Inst., 1981.
- [4] *Current Solutions to Hydrogen Problems in Steels*, C. G. Interrante, G. M. Pressouyre, eds., ASM, Metals Park, Ohio, 1982.
- [5] *Hydrogen Degradation of Ferrous Alloys*, R. A. Oriani, J. P. Hirth and M. Smialowski, eds., Noyes Publications, 1985.
- [6] *Hydrogen Effect on Material Behavior*, A. W. Thompson, N. R. Moody eds., to be published in 1990.
- [7] J. P. Hirth: *Metall. Trans.*, **11A**, 861 (1980).
- [8] R. A. Oriani: *Ann. Rev. Mater. Sci.*, **8**, 327-57 (1978).
- [9] R. A. Oriani: *Corrosion*, **43**, 390 (1987).
- [10] T. Boniszewski and G. C. Smith: *Acta Metall.*, **11**, 165 (1963).
- [11] B. A. Wilcox and G. C. Smith: *Acta Metall.*, **13**, 331 (1965).
- [12] R. M. Latanision and H. Opperhauser, Jr.: *Metall. Trans.*, **5A**, 483 (1974).
- [13] D. H. Lassila and H. K. Birnbaum: *Acta Metall.*, **34**, 1237 (1986).

- [14] T. Tsuru and R. M. Latanision: *Scripta metall.*, **16**, 575 (1982).
- [15] T. Schöber and C. Dieker: *Metall. Trans.*, **14A**, 2440 (1983).
- [16] M. A. V. Devanathan and Z. Stachuski: *Pro. Roy. Soc.*, **270A**, 90 (1962).
- [17] N. Boes and H. Züchner: *J. Less Common Metals*, **49**, 223-40 (1976).
- [18] J. Ovejero-Garcia: *J. Materials Sci.*, **20**, 2623-29 (1985).
- [19] S. M. Lee and J. Y. Lee: *Metall. Trans.*, **17A**, 181 (1986).
- [20] A. Kimura and H. K. Birnbaum: *Acta Metall.*, **36**, 757 (1988).
- [21] H. K. Birnbaum: Private communication, 1989.
- [22] A. M. Brass, A. Chanfreau, and J. Chene: Ref.6.
- [23] T. M. Harriss and R. M. Latanision: Ref.6.
- [24] R. W. Balluffi: *Diffusion in Crystalline Solids* eds. G. E. Murch and A. S. Nowick, Academic Press, Inc., pp.319-377 (1984).
- [25] B. Ladna and H. K. Birnbaum: *Acta Metall.*, **35**, 2537-42 (1987).
- [26] G. H. Gilmer and H. H. Farrell: *J. Appl. Phys.*, **47**, 4373 (1976).
- [27] P. M. Abraham, T. S. Elleman and K. Verghese: *J. Nuclear Materials*, 1978, **73**, 77 (1978).
- [28] H. S. Levine and C. J. MacCallum: *J. Appl. Phys.*, **31**, 595 (1960).
- [29] R. H. Jones: *Advances in the Mechanics and Physics of Surfaces*, Vol.3, 1986, ed. R. M. Latanision and T. E. Fischer, Harwood Academic Publishers, pp.1-70.
- [30] N. Bandyopadhyay, J. Kameda, and C. J. McMahon, Jr.: *Metall. Trans.*, **14A**, 881 (1983).
- [31] R. Viswanathan and S. J. Hudak, Jr.: *Metall. Trans.*, **8A**, 1633 (1977).
- [32] H. H. Johnson, J. F. Morlet and A. R. Troiano: *Trans. AIME*, **212**, 528 (1958).

- [33] A. R. Troiano: *Trans. ASM*, **52**, 54 (1960).
- [34] D. P. Williams and H. G. Nelson: *Metall. Trans.*, **1**, 63 (1970).
- [35] K. Yoshino and C. J. McMahon, Jr.: *Metall. Trans.*, **5A**, 363 (1974).
- [36] R. A. Oriani and P. H. Josephic: *Acta Metall.*, **22**, 1065 (1974).
- [37] W. W. Gerberich and Y. T. Chen: *Metall. Trans.*, **6A**, 271 (1975).
- [38] J. F. Lesser and W. W. Gerberich: *Metall. Trans.*, **7A**, 953 (1976).
- [39] G. W. Simmons, P. S. Pao and R. P. Wei: *Metall. Trans.*, **9A**, 1147 (1978).
- [40] S. K. Banerji, C. J. McMahon, Jr., H. C. Feng: *Metall. Trans.*, **9A**, 237 (1978).
- [41] J. Kameda and C. J. McMahon, Jr.: *Metall. Trans.*, **14A**, 903 (1983).
- [42] A. Kimura and H. Kimura: *Trans. Jpn. Inst. Met.*, **25**, 411 (1984).
- [43] C. L. Briant: *Ref.3*, pp.335-345.
- [44] M. Kuribayashi, H. Okabayashi: *Trans. Jpn. Inst. Met.*, **25**, 628 (1984).
- [45] A. J. West and M. R. Louthan, Jr.: *Metall. Trans.*, **10A**, 1675 (1979).
- [46] J. M. Hyzak and W. M. Garrison, Jr.: *Proceedings of Topical Conf. on Ferritic Alloys for Use in Nuclear Energy Technologies*, AIME, Warrendale, Pa, 385-393 (1984).
- [47] R. H. Jones: *Metall. Trans.*, **17A**, 1229 (1986).
- [48] R. J. Gest and A. R. Troiano: *Corrosion*, **30** 274 (1974).
- [49] K. S. Shin, C. G. Park and M. Meshii: *Ref.2*, pp.209-218.
- [50] A. W. Funkenbusch, L. A. Heldt and D. F. Stein: *Embrittlement by Liquid and Solid Metals*, AIME, Warrendale, Pa, pp.241-251 (1984).
- [51] S. M. Bruemmer, R. H. Jones, M. T. Thomas and D. R. Baer: *Metall. Trans.*, **14A**, 223 (1983).
- [52] Y. Ogino and T. Yamasaki: *Trans. Jap. Inst. Metals.*, **25**, 150 (1984).

- [53] R. C. Pond and W. Bollmann: *Philos. Trans. Roy. Soc. London* **292**, 449 (1979).
- [54] W. Bollmann: *Crystal Defects and Crystalline Interfaces* Springer-Verlag, N.Y., 1970.
- [55] A. P. Sutton: *Ph.D Thesis*, University of Pennsylvania, 1981.
- [56] A. P. Sutton and V. Vitek: *Philos. Trans. Roy. Soc. London* **309**, 1,37,55 (1983).
- [57] R. W. Balluffi, P. D. Bristowe and C. P. Sun: *J. Am. Ceram. Soc.* **64**, 23 (1981).
- [58] A. Brokman and R. W. Balluffi: *Acta Metall.*, **29**, 1703 (1981).
- [59] T. P. Darby, R. Schindler and R. W. Balluffi: *Philos. Mag.*, **A37**, 245 (1978).
- [60] C. P. Sun and R. W. Balluffi: *Philos. Mag.*, **A46**, 63 (1982).
- [61] D. A. Smith and R. C. Pond: *Int. Metall. Rev.*, **No.205**, 61 (1976).
- [62] A. H. King: *Acta Metall.*, **30**, 419 (1982).
- [63] A. Brokman, P. D. Bristowe and R. W. Balluffi: *J. Appl. Phys.*, **52**, 6116 (1981).
- [64] R. W. Balluffi, T. Kwok, P. D. Bristowe, A. Brokman, P. S. Ho and S. Yip: *Scri. Metall.*, **15**, 951 (1981).
- [65] E. W. Müller, T. Z. Tsong: *Field Ion Microscopy*, Elsevier, N.Y., p.254 (1969).
- [66] M. Hashimoto, Y. Ishida, R. Yamamoto and M. Doyoma: *Acta Metall.*, **29**, 617 (1981).
- [67] N. A. Gjostein: *Diffusion*, ASM, Metals Park, Ohio, 1973.
- [68] G. Martin and B. Perrailon: *Grain Boundary Structure and Kinetics*, ASM, Metals Park, Ohio, p.239, 1980.
- [69] N. L. Peterson: *Ref.40*, p.209.

- [70] R. E. Hoffman: *Acta Metall.*, **4**, 97 (1956).
- [71] R. W. Balluffi: *Phys. Stat. Solidi.*, **42**, 11 (1970).
- [72] L. G. Harrison: *Trans. Faraday Soc.*, **57**, 1191 (1961).
- [73] D. Gupta, D. R. Campbell and P. S. Ho: *Thin Films Interdiffusion and Reactions*, J. M. Poate, K. N. Tu and J. W. Mayer eds., Wiley, N.Y., pp.161-242, 1978.
- [74] G. B. Gibbs: *Phys. Stat. Solidi.*, **16**, K27 (1966).
- [75] J. C. Fisher: *J. Appl. Phys.*, **22**, 74 (1951).
- [76] T. Suzuoka: *Trans. Jap. Inst. Metals.*, **2**, 25 (1961).
- [77] R. T. P. Whipple: *Phil. Mag.*, **45**, 1225 (1954).
- [78] A. D. Le Claire: *J. Appl. Phys.*, **14**, 351 (1963).
- [79] G. H. Gilmer and H. H. Farrell: *J. Appl. Phys.*, **47**, 3792 (1976).
- [80] R. D. Calder, T. S. Elleman and K. Verghese: *J. Nuclear Materials*, **46**, 46 (1973).
- [81] J. H. Austin and T. S. Elleman: *J. Nuclear Materials*, **43**, 119 (1972).
- [82] B. Chew and F. T. Fabling: *Metal Sci. J.*, **6**, 140 (1972).
- [83] W. Beck, J. Bockris, J. McBreen and L. Nanis: *Proc. Roy. Soc.*, **A290**, 220 (1966).
- [84] W. M. Robertson: *Z. Metallk.*, **69**, 436 (1973).
- [85] V. M. Sidorenko and I. I. Sidorak: *Fiz. Khim. M. mat.*, **9**, 12 (1973).
- [86] M. Ransick and P. Shewmon: *Ref.2*, pp.895-902.
- [87] D. Eliezer: *Ref.2*, pp.913-21.
- [88] D. G. Westlake: *Trans. AME*, **62**, 1000 (1969).
- [89] R. Dutton: *Int. J. Hydrogen Energy*, **9**, 147-155 (1984).

- [90] M. P. Puls, L. A. Simpson and R. Dutton: *Fracture Problems and Solutions in the Energy Industry*, L. A. Simpson ed., Pergamon Press, Oxford, P.13, (1982).
- [91] C. Zapffe and C. Sims: *Trans. AIME*, **145**, 225 (1941).
- [92] A. S. Tetelman: *Fracture of Solids*, D. C. Drucker and J. J. Gilman eds., Gordon and Breach Sci. Publi. Inc., pp.671-708 (1963).
- [93] B. Baranowski: *Berichte der Bunsengesellschaft fur Physikalische Chemie*, **76**, 716 (1972).
- [94] G. G. Hancock and H. H. Johnson: *Trans. TMS-AIME*, **236**, 513 (1965).
- [95] P. Bastein and P. Azou: *C. R. Acad. Sci. Paris*, **232**, 1845 (1951).
- [96] J. K. Tien, A. W. Thompson, I. M. Bernstein and R. J. Richards: *Metall. Trans.*, **7A**, 821 (1976).
- [97] H. H. Johnson and J. P. Hirth: *Metall. Trans.*, **7A**, 1543 (1976).
- [98] G. S. Frankel and R. M. Latanision: *Metall. Trans.*, **17A**, 861 (1986).
- [99] C. Hwang and I. M. Bernstein: *Acta Metall.*, **34**, 1001-10 (1986).
- [100] R. P. Frohberg, W. J. Barnett and A. R. Troiano: *Trans. ASM.*, **47**, 892 (1955).
- [101] A. R. Troiano: *Trans. ASM.*, **52**, 54 (1960).
- [102] R. A. Oriani and Ber. Bunsenges: *Phys. Chem.*, **76**, 848 (1972).
- [103] M. S. Daw and M. I. Baskes: *Phys. Rev.*, **B29**, 6443 (1984).
- [104] A. J. Markworth and J. H. Holbrook: Ref.5, pp.535-560.
- [105] C. D. Beachem: *Metall. Trans.*, **3**, 437 (1972).
- [106] Lynch: *Act. Metall.*, **36**, 2639 (1988).
- [107] H. K. Birnbaum: *Atomistics of Fracture*, R. M. Latanision and J. R. Picken eds., Plenum Press, N.Y., p.733 (1983).

- [108] I. M. Robertson, T. Tabata, W. Wei, F. Heubaum and H. K. Birnbaum: *Scripta Metall.*, **18**, 841 (1984).
- [109] T. S. F. Lee and R. M. Latanision: *Met. Trans.*, **18A**, 1653-62 (1987).
- [110] M. J. Morgan and C. J. McMahon, Jr.: *Hydrogen Degradation of Ferrous Alloys*, ed. R. A. Oriani, J. P. Hirth and M. Smialowski, Noyes Publications, 1985, pp.608-40.
- [111] J. Crank: *The Mathematics of Diffusion*, Oxford Press, p.48 (1957).
- [112] M. Kurkela and R. M. Latanision: *Scripta metall.*, 1979, Vol.13, pp.927-32.
- [113] R. Zhu, J. Tong and W. zhang: *Corrosion*, 1987, Vol.43, pp.15-19.
- [114] W. Y. Choo and J. Y. Lee: *Metall. Trans.*, 1982, Vol.13A, pp.135-40.
- [115] G. W. Hong and J. Y. Lee: *Scripta Metall.*, 1983, Vol.17, pp.823-26.
- [116] M. Aucouturier: Ref.4, pp.407-12.
- [117] G. Vander Voort: *Metallography Principles and Practice*, McGraw-Hill Book Company, NY, 1984, pp.121-124.
- [118] P. G. Shewmon: *Diffusion in Solids*, McGraw Hill Book Co., 1963, p.18.
- [119] L. R. Louthan, Jr., J. A. Donovan and G. R. Caskey, Jr.: *Acta Metall.*, 1975, Vol.23, pp.745-49.
- [120] T. P. Perng and C. J. Altstetter: *Acta Metall.*, 1986, Vol.34, pp.1771-81.
- [121] R. Otsuka and M. Isaji: *Scripta metall.*, **15**, 1153-56 (1981).
- [122] Y. Ebisuzaki, W. J. Kass and M. O'Keefee: *J. Chemical Physics*, **46**, 1378-81 (1967).
- [123] *Metals Handbook*, ASM, ninth edition, pp.131 and 749 (1980).
- [124] K. M. Olsen, C. F. Larkin and P. H. Schmitt, Jr.: *Trans. ASM*, **53**, 349 (1961).
- [125] M. I. Baskes and V. Vitek: *Met. Trans.*, **16A**, 1625 (1985).

- [126] S. Floreen and J. H. Westbrook: *Acta Metall.*, **17**, 1175-81 (1969).
- [127] H. Vehoff and H. K. Klameth: *Acta Metall.*, **33**, 955 (1985).
- [128] T. Mütschele and R. Kirchheim: *Scripta Metall.*, **21**, 135-140 (1987).
- [129] R. Kirchheim: *Acta Metall.*, **29**, 835-43 (1981).
- [130] R. V. Bucur and E. Indrea: *Acta Metall.*, **35**, 1325-32 (1987).
- [131] G. E. Dieter: *Mechanical Metallurgy*, second edition, McGraw-Hill Book Company, 1976, p.245.
- [132] G. Saindrenan, D. Roptin, J. M. Maufra and B. Bauche: *Scripta Metall.*, **23**, 1163-68 (1989).
- [133] J. Eastman, T. Matsumoto, N. Narita, F. Heubaum and H. K. Birnbaum: Ref.2, p.397.
- [134] T. F. Lee: Ph.D. thesis, MIT, 1982.
- [135] J. R. Rice: Ref.1, p.455.
- [136] J. K. Tien, S. V. Nair, and R. R. Jensen: Ref.2, p.37.
- [137] C. M. Hsiao: Ref.6.
- [138] M. Cornet, M. F. Trichet and S. Talbot-Besnard: *Mem. Sci. Rev. Met.*, **74**, 307-16 (1977).
- [139] D. J. Dingley and R. C. Pond: *Acta Metall.*, **27**, 667 (1979).
- [140] J. P. Hirth: *Theory of Dislocations*, second edition, John Wiley & Sons, Inc., p.764, 1982.
- [141] D. Kuhlmann-Wilsdorf and N. R. Comins: *Mat. Sci. Eng.*, **60**, 7 (1983).
- [142] N. Hansen and D. Kuhlmann-Wilsdorf: *Mat. Sci. Eng.*, **81**, 141 (1986).
- [143] C. Verpoort, D. J. Duquette, N. S. Stoloff and A. Neu: *Mat. Sci. Eng.*, **64**, 135 (1984).

# Appendix A

## FORTRAN Program for Permeation Curves

```
C      C=====C
C      C  PROGRAM P3 UNDER PERMEATIONS (J. YAO'S MODEL)      C
C      C  CALCULATING THE PERMEATION CURVE VS TIME WITH      C
C      C  DOUBLE PRECISION-FINAL FORM                          C
C      C  SAME AS P2 BUT WRITE IN DATA FILES AS WELL        C
C      C=====C
      DIMENSION DBESS(99)
      DOUBLE PRECISION PI,P,A1,AFA,Z0,Z1,Z2,Z3,Z4,Z5,Z6
      DOUBLE PRECISION MMBSJ1,MMBSJ0,Y,DBESS,Z55,Z56,Z65,Z66
      DOUBLE PRECISION B,BO,BA,BAO,B1,BB,BBO,BBA,BBAO
C      C=====C
C      C  TO INPUT PRE-STORED FIRST 100 ZERO POINTS OF BESSEL  C
C      C  FUNCTION OF ZERO ORDER                                C
C      C=====C
      READ(99,1)DBESS
1      FORMAT(3(2X,F20.16))
C      C=====C
C      C  TO INPUT PARAMETERS FOR CALCULATION                  C
C      C=====C
2      READ*, DELTA,DIA,TEM,EB,DL,THI,T
      IF (TEM.LT.0.1) GOTO 65
C      C=====C
C      C          DICTIONARY OF PARAMETERS                      C
C      C
C      C  DELTA: Ratio of two diffusivities, Dgb/Dl           C
C      C  DIA: AVERAGE DIAMETER OF GRAINS                    C
C      C  TEM: TEMPERATURE                                     C
C      C  EB: BINDING ENERGY                                  C
C      C  DL: DIFFUSION COEFFICIENT                            C
```

```

C      C      THI: THICKNESS OF THE SPECIMEN      C
C      C      T:   TIME FOR FIRST TRY I.E. SATURATION      C
C      C=====C
C
C      C=====C
C      C      WRITE THE INPUT PARAMETERS FOR LATER EXAM      C
C      C=====C
WRITE(6,3)DELTA,DIA,TEM,EB,DL,THI
WRITE(12,3)DELTA,DIA,TEM,EB,DL,THI
3      FORMAT(2X,'DGB/DL=',F8.3,8X,'GRAIN DIA.=',F9.7,'CM',6X,
1      'TEMPERATURE=',F4.0,'K'//2X,'BINDING ENERGY=',F6.0,'J',
1      3X,'DL=',E9.3,'CM^2/S',4X,'THICKNESS=',F6.4,'CM')
WRITE(6,4)
4      FORMAT(//8X,'TIME',10X,'IS',12X,'IGB',12X,'TOTAL',7X,
1      'IS/TOTAL %',6X,'IS%',11X,'IGB%',9X,'TOTAL%',10X,'PS')
WRITE(12,5)
5      FORMAT(//2X,'TIME',5X,'IS',6X,'IGB',6X,'TOTAL',
1      2X,'IS/TOTAL(%)',3X,'IS%',5X,'IGB%',4X,'TOTAL%')
C      C=====C
C      C      INTRODUCE INTERMEDIUM PARAMETER;      C
C      C      A IS THE HALF WIDTH OF GRAIN BOUNDARY      C
C      C=====C
A=5.0E-8
PI=3.1415926535897932D0
S=EXP(EB/TEM/8.31)
AS=A*S
P=PI/THI
6      BB=0.0
BBA=0.0
BBN=0.0
NS=-1
DO 40 N=1,200
ZO=N*PI
B=0.0
BA=0.0
BBO=BB
BBAO=BBA
DO 20 M=1,99
BO=B
BAO=BA
Y=DBESS(M)
CALL SOLAFA(AFA,N,M,Y,P,AS,DIA,DELTA,PI,IE,XXX)
A1=DIA*AFA/2.0D0

```

```

Z1=MMBSJ1(A1,IE1)
Z2=MMBSJO(A1,IE2)
IE=IE+IE1+IE2
IF (IE.GT.0) THEN
  WRITE(6,*) 'ERROR! IE=',IE
  GOTO 50
END IF
Z3=Z1*Z1
Z4=Z2*Z2
Z5=AFA*AFA
Z55=DL*T*Z5
IF (Z55.GT.50.) THEN
  GOTO 22
ELSE
  Z56=DEXP(-Z55)
END IF
Z6=Z56*8.0D0*(Z1+AS*AFA*Z2)/AFA/DIA/(Z3+(1.0+4.0*AS/DIA)*Z4)
BA=BA+Z6*Z1*4.0D0/AFA/DIA
B=B+Z6*Z2
20 CONTINUE
WRITE(6,*) 'NEED MORE AFA! N=',N
22 CONTINUE
Z65=DL*T*(Z0/THI)**2
IF (Z65.GT.50.) THEN
  GOTO 42
ELSE
  Z66=DEXP(-Z65)
END IF
B1=Z66*NS
BB=BB+B*B1
BBA=BBA+BA*B1
BBN=BBN+2.0*B1
NS=-NS
40 CONTINUE
42 CONTINUE
Z8=4.0*DELTA*AS/DIA+1.0
CIGB=(Z8-1.0)*(1.0+BB)
CIGB1=CIGB/Z8
CIS=1.0+BBA
CIS1=CIS/Z8
CIT=CIGB+CIS
CIT1=CIGB1+CIS1
PS=1.0+BBN
IF (CIT.GT.1.0E-8) THEN

```

```

      Z7=100.0*CIS/CIT
    ELSE
      Z7=0.0
    END IF
C=====C
C      C      WRITE CALCULATED RESULTS      C
C=====C
    WRITE(6,45)T,CIS,CIGB,CIT,Z7,CIS1,CIGB1,CIT1,PS
45  FORMAT(/4X,F8.0,3(3X,F12.5),7X,F6.2,4(8X,F6.4))
    WRITE(12,46)T,CIS,CIGB,CIT,Z7,CIS1,CIGB1,CIT1
46  FORMAT(/1X,F6.0,3(1X,F8.5),2X,F6.2,2X,3(3X,F6.4))
    IF (CIT.LT.1.0E-5) GOTO 50
    IF (T.GT.10000.0) THEN
      TI=10000.0
    ELSE IF (T.GT.1000.) THEN
      TI=1000.0
    ELSE IF (T.GT.100.) THEN
      TI=100.0
    ELSE IF (T.GT.10.) THEN
      TI=10.0
    ELSE IF (T.GT.1.) THEN
      TI=1.0
    ELSE IF (T.GT..1) THEN
      TI=.1
    END IF
    T=T-TI
    IF (T.LE.0.5) GOTO 50
    GOTO 6
50  CONTINUE
    WRITE(6,60) XXX
    WRITE(12,60) XXX
60  FORMAT(/10X,'*****',3X,'XXX=',F10.0,3X,'*****')
    GOTO 2
65  CONTINUE
    STOP
    END
C=====C
C      C      SUBROUTINE TO SOLVE EQUATION 3.32 IN THESIS  C
C=====C
    SUBROUTINE SOLAFA(FA,I,J,Y,P,AS,DIA,DELTA,PI,IE,XXX)
      DOUBLE PRECISION FA,X,X1,X2,F,FF,BBB,P,PI,Y
      DOUBLE PRECISION MMBSJ1,MMBSJO,BEITA,FFO,FO
      XXX=XXX+1.0
      BEITA=P*I

```

```

      BBB=BEITA*BEITA*(DELTA-1.0)*DIA*DIA/4.0D0
      X=Y
80     X=X-0.1D0
      F=X+DIA*MMBSJ1(X,IE3)/MMBSJ0(X,IE4)/AS/2.0-BBB/X
      IE=IE+IE3+IE4
      IF (IE.GT.0) RETURN
      IF (F.GT.0.0D0) GOTO 80
      X1=X
      X2=X+0.1
      DO 90 NN=1,50
      X=(X1+X2)/2.0D0
      FF=X+DIA*MMBSJ1(X,IE3)/MMBSJ0(X,IE4)/AS/2.0-BBB/X
      IF (FF.LT.0.0D0) THEN
        X1=X
      ELSE
        X2=X
      END IF
      IE=IE+IE3+IE4
90     CONTINUE
      FA=X*2.0/DIA
      RETURN
      END
C      C=====C
C      C INPUT ORDER OF THE DATA: K, L, TEM, EB, DL, THI, T C
C      C PROGRAM STOPS WHEN ALL INPUT BE ZERO C
C      C=====C

```

# Appendix B

## FORTRAN Program for Penetration Tests

```
C      PROGRAM J2 UNDER PENETRATIONS (J. YAO'S MODEL)
C      CALCULATING THE INTERGRANULAR CRACKING DEPTH VS TIME
      DOUBLE PRECISION PI,P,A1,AFA,Z0,Z1,Z2,Z3,Z4,Z5,Z55,Z56
      DIMENSION DBESS(99)
      DOUBLE PRECISION DBESS,MMBSJ1,MMBSJ0,Z65,Z66
      READ(99,1)DBESS
1      FORMAT(3(2X,F20.16))
C      DELTA: Ratio of two diffusivities, Dgb/Dl
C      DIA:   Average diameter of grains
C      TEM:   TEMPERATURE OF HYDROGEN CHARRGING
C      EB:    BINDING ENERGY
C      DL:    DIFFUSION COEFFICIENT
C      THI:   THICKNESS OF THE SPECIMEN
C      CC:    Ratio of critical to surface concentrations
C      T:     Time for first try
C      Y1:    Expected min. depth at time t
C      Y2:    Expected max. depth at time t
      A=5.0E-8
      PI=3.141592653589793D0
2      READ*, DELTA,DIA,TEM,EB,DL,THI,CC,T,Y1,Y2
      IF (DIA.LT.0.00000001) GOTO 65
      S=EXP(EB/TEM/8.31)
      TTT=0.0
      AS=A*S
      THI1=THI/2.0
      P=PI/THI
      WRITE(6,3)DELTA,DIA,TEM,EB,DL,THI,CC
3      FORMAT(5X,'K=',F8.0,10X,'GRAIN DIA.=' ,F6.4,
1 5X,'TEMPERATURE=' ,F5.0,5X,'BINDING ENERGY=' ,
```

```

1 F6.0//5X,'DIFFUSIVITY=',E9.3,5X,'THICKNESS=',F5.3,
1 5X,'CRITICAL/SURFACE CONCENTRATION=',F5.3)
  WRITE(6,4)
4  FORMAT(//10X,'TIME',25X,'IG DEPTH',25X,
1  'LATTICE CONTRIBUTION %')
5  Y=(Y1+Y2)/2.0
6  N=1
  BB=0.0
10 Z0=(2.0*N-1.0)*PI
  M=1
  B=0.0
  BBO=BB
  IF (TTT.GT.0.5) THEN
    B=4.0/Z0
    GOTO 30
  END IF
20 BO=B
  Z=DBESS(M)
  CALL SOLAFA(AFA,N,M,Z,P,AS,DIA,DELTA,PI,IE,XXX)
  A1=DIA*AFA/2.0
  Z1=MMBSJ1(A1,IE1)
  Z2=MMBSJ0(A1,IE2)
  IE=IE+IE1+IE2
  IF (IE.GT.0) THEN
    WRITE(6,*) 'ERROR! IE=',IE
    GOTO 50
  END IF
  Z3=Z1*Z1
  Z4=Z2*Z2
  Z5=AFA*AFA
  Z55=DL*T*Z5
  IF (Z55.GT.50.) THEN
    GOTO 30
  ELSE
    Z56=DEXP(-Z55)
  END IF
  B=B+Z56*Z2*16.0*(Z1+AS*AFA*Z2)/AFA/DIA/(Z3+
1 (1.0+4.0*AS/DIA)*Z4)/Z0
  M=M+1
  IF (M.GE.99) THEN
    WRITE(6,*) 'NEED MORE AFA! N=',N
    GOTO 30
  END IF
  IF (ABS(B-BO).GT.1.0E-5) GOTO 20

```

```

30   Z65=DL*T*(ZO/THI)**2
      IF (Z65.GT.50.) THEN
          GOTO 35
      ELSE
          Z66=DEXP(-Z65)
      END IF
      B1=Z66*SIN(ZO*Y/THI)
      BB=BB+B*B1
      N=N+1
      IF (ABS(BB-BB0).GT.1.0E-5) GOTO 10
35   CONTINUE
      IF (TTT.GT.0.5) GOTO 40
      SHENYU=CC-1.0+BB
      IF (SHENYU.LT.0.0) THEN
          Y1=Y
      ELSE
          Y2=Y
      END IF
      IF ((Y2-Y1)/Y.GT.0.001) GOTO 5
      IF (TTT.LT.0.5) THEN
          TTT=1.0
          GOTO 6
      END IF
40   Z7=100.0*(1.0-BB)/CC
      WRITE(6,45)T,Y,Z7
45   FORMAT(/5X,F10.0,25X,F10.5,35X,F5.1)
      TTT=0.0
      Y1=Y
      Y2=Y+Y
      IF (Y2.GT.TH1) Y2=TH1
      IF (ABS(TH1/Y-1.0).LT.0.0005) GOTO 50
      IF (T.LT.1000.0) THEN
          T=T+300.
      ELSE
          T=T+600.
      END IF
      GOTO 5
50   CONTINUE
      WRITE(6,60) XXX
60   FORMAT(/10X,'*****',3X,'XXX=',F10.0,3X,'*****')
      GOTO 2
65   CONTINUE
      STOP
      END

```

```

SUBROUTINE SOLAFA(FA,I,J,Z,P,AS,DIA,DELTA,PI,IE,XXX)
  DOUBLE PRECISION FA,X,X1,X2,F,FF,BBB,P,PI
  REAL MMBSJ1,MMBSJO
  XXX=XXX+1.0
  BEITA=(2.0*I-1.0)*P
  BBB=BEITA*BEITA*(DELTA-1.0)*DIA*DIA/4.0
  X=Z
80  X=X-0.1
  F=X+DIA*MMBSJ1(X,IE3)/MMBSJO(X,IE4)/AS/2.0-BBB/X
  IE=IE+IE3+IE4
  IF (IE.GT.0) RETURN
  IF (F.GT.0.0D0) GOTO 80
  X1=X
  X2=X+0.1
  DO 90 NN=1,40
  X=(X1+X2)/2.0
  FF=X+DIA*MMBSJ1(X,IE3)/MMBSJO(X,IE4)/AS/2.0-BBB/X
  IF (FF.LT.0.0D0) THEN
    X1=X
  ELSE
    X2=X
  END IF
  IE=IE+IE3+IE4
90  CONTINUE
  FA=X*2.0/DIA
  RETURN
  END

```